PROPOSAL OVERVIEW

During the last decade, three extensive projects in atomic physics were carried out at the unique LEAR facility by the PS194, PS200 and PS205 collaborations. The results of these experiments suggest that a series of finer measurements, first using the lower energy and smaller emittance of the AD, and then supplementing these advantages with RFQ and Trap techniques, will be yet more intriguing.

When antiprotons are introduced into matter, the following sequence of processes take place: i) they slow down, ii) they form antiprotonic atoms, and iii) the produced antiprotonic atoms collide with surrounding atoms/molecules during thermalization. The metastable $\bar{p}He^+$ atomcule studied intensively by the PS205 group at LEAR is the product of such complex atomic processes. In order to understand each process fully, and to form other species of metastable antiprotonic atoms (such as $\bar{p}p$) for precision spectroscopy, experiments with lower energy beams are essential.

We therefore propose to study fundamental atomic processes involving antiprotons, antiprotonic atom formation, and the structure of antiprotonic atoms ($\bar{p}He^+$ and $\bar{p}p$ in particular), with the slow antiprotons from the CERN Antiproton Decelerator (AD) together with an RFQ post–decelerator and an antiproton Penning trap.

As shown in Fig. 1, the proposed experiments are categorized into three groups. The high degree of interconnectedness of the LEAR PS194 and LEAR PS205 lines of research is shown by the transverse arrows.

1. "$\bar{p}He^+$ atomcule spectroscopy using the 5.8 MeV beam of the AD" is described in Section 2, which is based on the success of the PS205 experiment at LEAR. The research program includes higher-resolution laser spectroscopy of $\bar{p}$ energy levels, a laser + microwave resonance experiment to measure the hyperfine splitting (HFS) of $\bar{p}He^+$, and extensive studies of the interaction of $\bar{p}He^+$ atomcules with surrounding atoms and molecules.

2. "Experiments with $\sim$ 100 keV antiproton beams from the RFQ", described in Section 3, will make use of antiprotons decelerated by the RFQ post–decelerator, and will study the antiproton energy loss and channeling at low energy in various gaseous and solid targets. This is an extension of some of the measurements performed by the PS194 collaboration at LEAR. We will also study the "primordial" (n, l) distribution of $\bar{p}He^+$, i.e., the (n, l) distribution immediately after the atomcule formation, before these are affected by collisional processes.

3. In order to carry out the "Experiments with antiprotons in and from the trap", described in Section 4, we construct a Penning-type trap downstream of the RFQ to cool antiprotons. They are either extracted as an ultra-slow (10 keV - 10 eV) beam, or used as a collision target. Experiments to measure the Langevin cross sections, ionization cross sections, antiprotonic atom formation cross sections, etc., will be done as a continuation of the atomic physics results of the PS194 and PS200 LEAR collaborations.

When $\bar{p}p$ atoms are produced in a collision-free environment, they should exhibit metastability (lifetime $\gg 1\ \mu s$). As in the $\bar{p}He^+$ case, high-resolution laser spectroscopy of $\bar{p}p$ (protonium) can be done, which will lead to a high precision determination of the antiprotonic Rydberg constant.

Table 1 summarizes the timeline of the proposed experiment.

Table 1: *The timeline of the proposed experiment*

1997 Feb.	Approval of 'Shinpro' funding*
1997 October	Proposal presented at SPSC
1997 December	RFQ final design report due
1998 April	Start of 'Shinpro' funding*
1998 July	Catching trap magnet delivered to Tokyo
1998 Fall	Construction of laser hut, etc., in the AD hall
1998 Winter	Delivery of the new laser system to CERN
1999 May	Start of the $\bar{p}He^+$ laser spectroscopy using the 5.8 MeV beam
1999 Fall	RFQ commissioning
1999 Winter	Catching trap delivered to CERN
2000 Spring	RFQ installation
2000 May	Start of $\bar{p}He^+$ study using the ~ 100 keV beam
2000 May	Start of energy loss, channeling, and $\bar{p}$ swarm experiments
2000 June	Catching trap commissioning
2000 July	Experiments on ionization, antiprotonic atom formation and laser spectroscopy
↓	↓

* A 5-year Japanese grant for the AD experiments (~ 10 MCHF total).

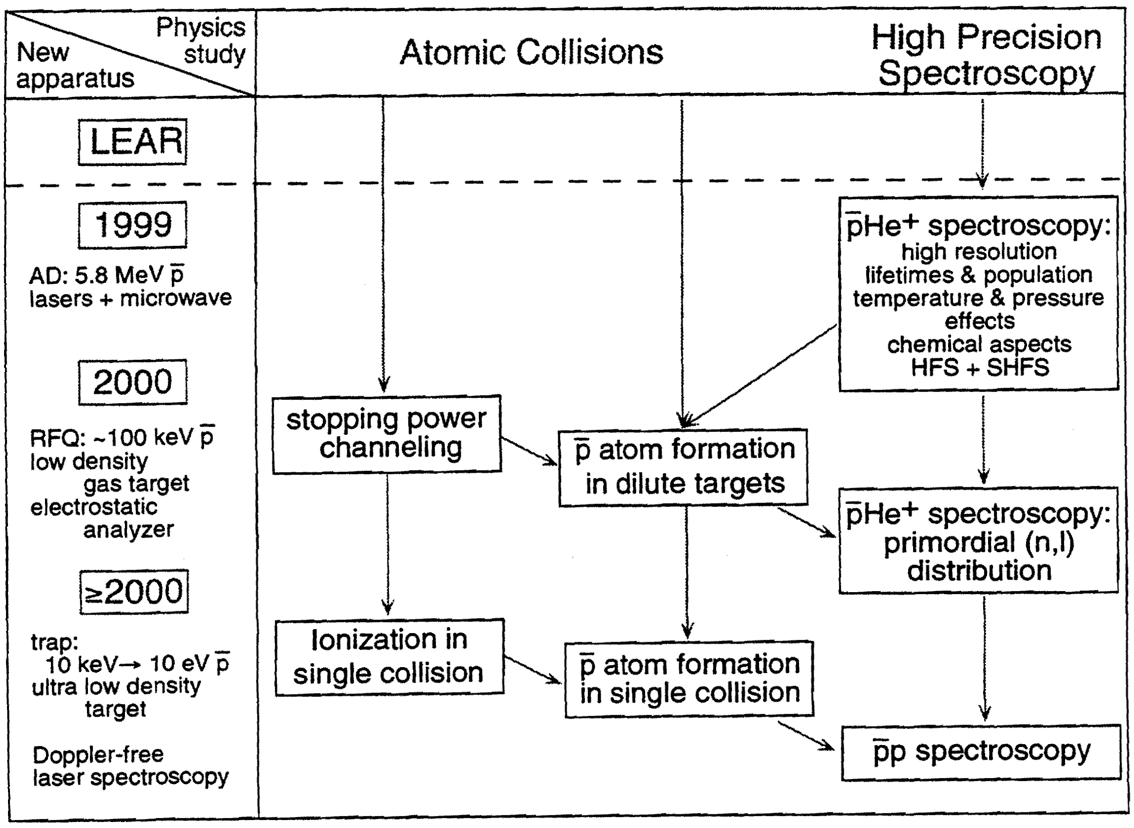

Figure 1: *An overview of the proposed experiment.*

Contents

1 Introduction

Group Logo: The giant lantern of Kaminari-mon Gate of Asakusa Temple, a symbol of downtown Tokyo

1.1 $\bar{\mathrm{p}}\mathrm{He}^+$ laser spectroscopy at LEAR

The antiprotonic helium atom-molecule (in short, atomcule), $\mathrm{e}^-\bar{\mathrm{p}}\mathrm{He}^{2+} \equiv \bar{\mathrm{p}}\mathrm{He}^+$, is a surprisingly metastable three-body system involving a $\bar{\mathrm{p}}$ as one of the constituents, first discovered at KEK in 1991 [1]. This peculiar object, which interfaces between matter and antimatter, offers a unique high-precision arena of fundamental physics using laser and microwave spectroscopy as well as a laboratory for uncovering various physical and chemical phenomena. The theoretical studies in the early stage [2–7] revealed the following features.

In the metastable $\bar{\mathrm{p}}\mathrm{He}^+$ atomcule the $\bar{\mathrm{p}}$ possesses a large principal quantum number n ($n \sim n_0 = \sqrt{M^*/m_e} \sim 38$, M^* being the reduced mass of $\bar{\mathrm{p}}$–He^{2+}) and a large orbital angular momentum $l (l \sim n-1)$, and the e^- stays in the ground ($\sim$ 1s) orbital. Since the energy level spacing $E_n - E_{n-1}$ (typically around 2 eV for $n \sim 38$) is much smaller than the ionization energy $I_0 \approx 25$ eV, fast Auger transitions with L (multipolarity)$= \Delta l \leq 3$ are energetically impossible from large-(n, l) states near the circular ($l = n - 1$) orbital. Furthermore, the interaction between the $\bar{\mathrm{p}}$ and the e^- removes the degeneracy of different-l states for each n. This helps to suppress the collisional Stark mixing that would otherwise cause rapid destruction of large-l metastable states. Thus, the antiproton can only undergo slow successive radiative transitions, each with about 1 μs lifetime, when it lies in a large (n, l) domain as designated by the solid lines in Fig. 2. These transitions tend to follow the $v = n - l - 1 =$ constant propensity rule. The levels shown by wavy lines in Fig. 2 have larger Auger rates than radiative rates, and are hence short lived.

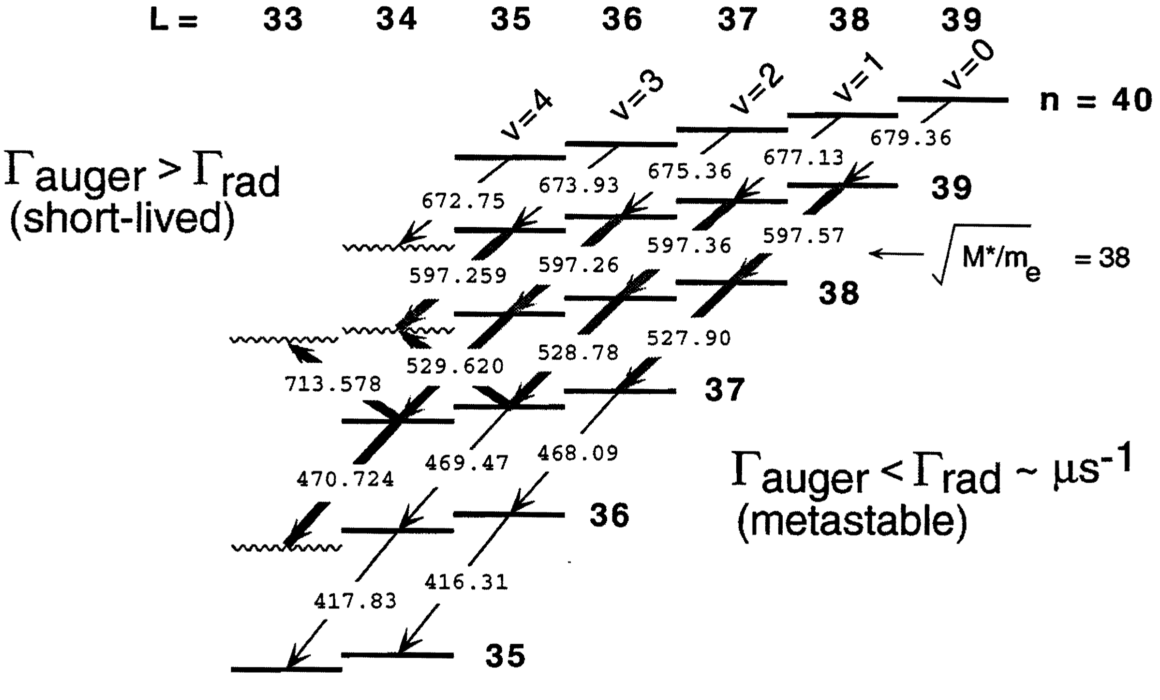

Figure 2: *The level scheme of large-*(n, l) *states of the* $\bar{\mathrm{p}}^4\mathrm{He}^+$*atomcule. The levels shown in solid lines indicate radiation-dominated metastable states, while those shown in wavy lines are Auger-dominated short-lived states. The laser-induced transitions already observed are denoted by bold arrows and the transition wavelengths are shown in the units of nanometer.*

The study of metastable $\bar{\mathrm{p}}\mathrm{He}^+$ at LEAR was initiated late in 1991 as one of the smallest experiments at that machine (PS205) and delayed annihilation lifetime spectra (DATS) of antiprotons in various helium media were studied [8–12]. Two years later, the introduction of laser spectroscopy measurements of atomic transitions [13, 14] marked the start of the second generation of experiments on this atom [15–19], and a new departure in the study of the antiproton.

The principle of laser spectroscopy is to induce resonant transitions from a parent metastable state to a daughter short-lived state by a laser pulse. The laser-induced transitions are almost instantly followed by $\overline{\text{p}}$ annihilation and thus are detected as a spike-like response in the delayed annihilation time spectra (DATS). At first, this laser-based approach retained the parasitic nature of the earlier experiments using a slow-extracted beam to observe the spike in an event-by-event mode. In 1994, however, we began "analogue" measurements of delayed annihilation time spectra (ADATS) [20–29] in which a fast-extracted bunch of antiprotons was stopped in our helium gas target and produced instantaneously a sample of metastable $\overline{\text{p}}\text{He}^+$ atoms that behaves in many ways like a rapidly decaying radioactive source. By recording the 'activity' of this source we could obtain from a single laser pulse all the information previously obtained from some 10^7 antiprotons extracted over 20–30 minutes. This technique developed at LEAR in 1994–1996 forms the basis of the present proposal at the AD where continuous extraction is not possible.

Experiment PS205 initiated an explosive theoretical activity: various research groups in Japan, Germany, Russia, England, USA, Bulgaria, Italy, Hungary and Sweden published calculations of increasing precision on the energy levels and transition rates of the $\overline{\text{p}}\text{He}^+$ three–body system [30–51]. Recently, Korobov [44] has used a variational method to calculate the transition wavelengths in agreement with the experimental values at the level of $\sim$ 50 ppm. When this calculation was augmented by the relativistic correction for the motion of the 1s electron [45], the agreement became as good as a few ppm [23], as shown in Fig. 3.

At the ppm level, evidently, fine and hyperfine structure start to appear as in other atoms. The energy levels of the $\overline{\text{p}}\text{He}^+$ atomcule are split by the interaction of the magnetic moments associated with the spins and angular momenta of the antiproton and the electron. As described in more detail in Section 2.5, the largest effect arises from the interaction of the $\overline{\text{p}}$ angular momentum L and the electron spin $S_e = 1/2$. We call this the "hyperfine" structure (HFS). This splits each level into a doublet with quantum numbers $F^+ = L + 1/2$ and $F^- = L - 1/2$. The effect of the antiproton spin is to split each of the doublets into two states, but according to theoretical calculations [39, 46] the energy difference is smaller by an order of magnitude and is unobservable with the experimental resolution of PS205.

In a laser-induced electric dipole transition a parent doublet state (n, L) proceeds to a daughter doublet state (n', L') according to the selection rule $F = L \pm 1/2 \to F' = L' \pm 1/2$. The resonance profile should then show a double hump structure with a splitting equal to the *difference* of the splitting of parent and daughter state. Theoretical calculations [37, 39, 46] showed that the splitting of a resonance line is small for "favoured" transitions following the propensity rule $\Delta v = \Delta(n - L - 1) = 0$ (typically 100 to 600 MHz), but larger for $\Delta v = 2$ "unfavoured" transitions.

We therefore performed a precise measurement of the resonance profile of the previously discovered transition [23] $(n, L) = (37, 35) \to (38, 34)$ at 726.095 nm. The laser bandwidth, which in the normal PS205 running condition was typically about 7 GHz, could be narrowed to 1.2 GHz by inserting an intra-cavity etalon into the oscillator part of the dye laser. Fig. 4 shows the obtained resonance profile which clearly reveals a — partly resolved — doublet structure with a separation of $\Delta\nu = 1.70 \pm 0.05$ GHz [24] which is in good agreement with the theoretical value of 1.77 GHz [46]. This is the first observation of a hyperfine structure in this unusual three-body system. A more precise measurement planned using a laser/microwave triple resonance technique (see Section 2.5) will measure the $L_{\overline{p}} - S_{e^-}$ splitting directly, rather than the difference of two large numbers, and will give insight in the three-body wavefunctions used for calculation, as well as the $\overline{\text{p}}$ magnetic

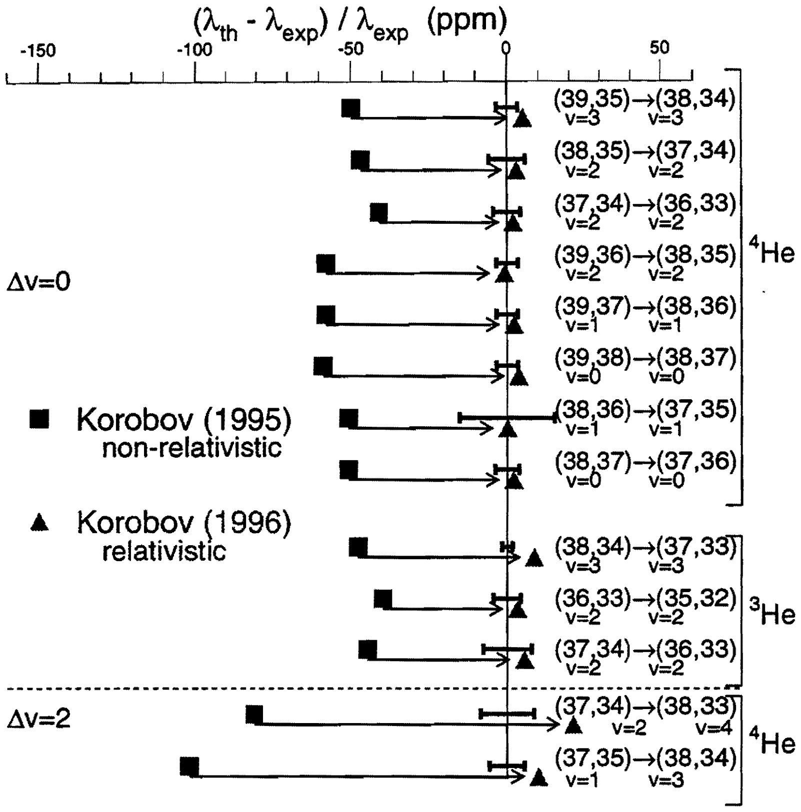

Figure 3: *Comparison of the observed transition wavelengths* λ_{exp} *and the calculated wavelengths* λ_{th}.

moment and QED corrections.

Appendix A describes other recent results on $\bar{p}He^+$ spectroscopy at LEAR including:

- precise measurement of transition frequencies and their density shifts;
- dependence of the level lifetimes on the helium density;
- the influence of impurities and Hydrogen Assisted Inverse Resonance (HAIR) studies.

The new area of antiprotonic atom laser spectroscopy pioneered by the PS205 experiment forms a logical and crucial part of the AD program. In 1999, when the AD first becomes operational, we plan to continue to work on the $\bar{p}He^+$ spectroscopy by using the 5.8 MeV direct beam from the AD. We plan to study the laser induced transitions of the $\bar{p}He^+$ more precisely and, in particular, the hyperfine structure of the $\bar{p}He^+$ atom by using a laser-microwave triple resonance technique. This will provide a stringent test of the three-body $\bar{p}He^+$ theory, and will enable us to determine the antiprotonic Rydberg with a better accuracy than available today. In the year 2000, we plan to install an RFQ decelerator and an antiproton catching trap. With the $\sim$ 100 keV antiprotons emerging from this, we will be able to study the "primordial" $\bar{p}He^+$ states formed in ultra-low density helium media by our well proven annihilation time analysis and laser spectroscopy techniques.

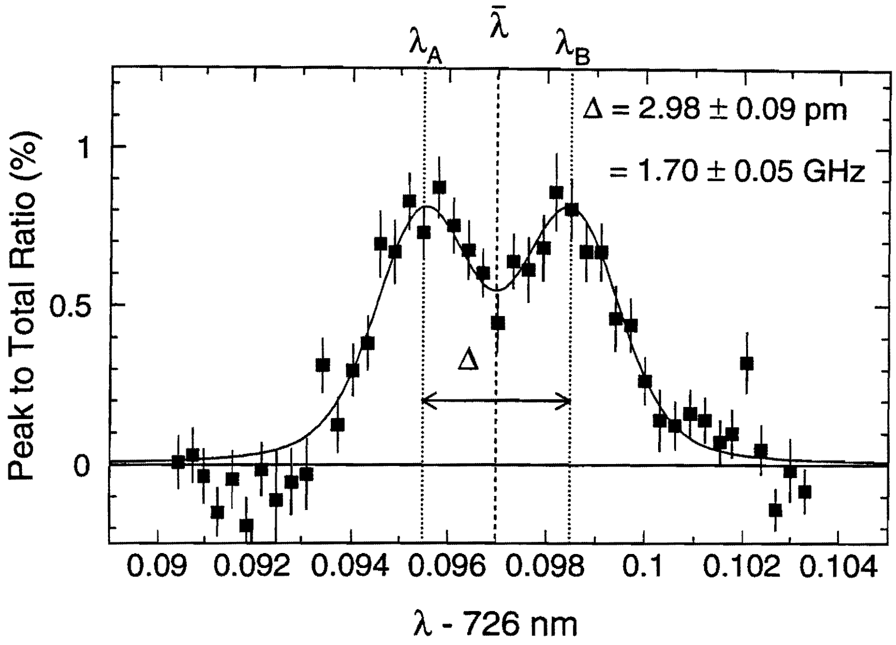

Figure 4: *High resolution resonance profile of the* $(37,35) \to (38,34)$ *transition of* $\bar{p}He^+$ *atomcules showing clearly a doublet structure. The solid line represents a fit of a sum of two functions consisting each of a Gaussian of fixed width of 1.2 GHz representing the measured laser bandwidth folded with a Lorentzian.*

In the middle of the year 2000, we expect to add a Penning trap after the RFQ. By extracting 10–20 eV antiprotons from this we will be able to initiate a new series of experiments on metastable protonium by colliding them onto a hydrogen jet or low density target, as discussed in Section 4.2.

1.2 Atomic collisions with antiprotons

In the field of atomic collisions, the forces between the participating particles (electrons, nuclei) are precisely known, and it is a very good approximation to assume that the particles are structureless. By measuring the cross sections associated with few-particle atomic collisions, it is therefore possible to study dynamic many-body effects in very clean cases. This is a great help to the advancement of many-body theory in general.

During the last decade it has been demonstrated that comparisons between impact of particles and their antiparticles are very fruitful in this respect. This is due to the fact that if we change the projectile from, say a proton to an antiproton, we only reverse the sign of the coupling constant, while all other important variables (such as the projectile mass, velocity etc) can be kept unaltered.

At high projectile velocities v, where the parameter q/v is much smaller than unity (v is measured in atomic units, and qe is the projectile charge) perturbation theory is valid, and we can write the cross section (for example for single or multiple ionization of the target atom) as

$$\sigma = a_1(v)q^2 + a_2(v)q^3 + a_3(v)q^4 + ... \quad (1)$$

where the leading term describes one projectile-target electron interaction, and is given mostly by the target structure. In contrast, the higher order terms contain contributions from multiple processes where, for example, the projectile interacts with each of two target electrons, with one target electron twice, or where a target electron, after having interacted with the projectile, interacts with another target electron. These terms are very difficult to calculate, because it is necessary to take into account detailed many-body phenomena (such as electron-electron correlation) in a dynamic system. Their calculations constitute a great challenge to atomic collision theory.

If we measure the cross section for equi-velocity proton and antiproton impact, we can extract the first higher order term $a_1(v)q^3$ with high accuracy, and hence supply the theorists with bench-mark data for tests of their theoretical models. This has been the underlying strategy for much of the work performed by the collaboration PS194 at LEAR, see Ref. [55].

As a few examples of this work, we may mention the measurements of the single ionization of helium by proton and antiproton impact [56, 57] which disclosed the role of polarization of the target atom in the initial part of the collision for high velocity projectiles, and the measurements of the cross section for double ionization of He for the same two projectiles, which highlighted the interference between various channels that lead to double ionization — an effect that surprisingly makes the high projectile velocity double ionization cross section for antiprotons twice as large as that for equi-velocity proton impact [57]. This work has led to the development of very sophisticated many-body theories for atomic collisions, like the Forced Impulse Method [58].

A phenomenon which is quite closely related to ionization is the energy loss of the charged projectiles. The reason is that at high energy, charged particles loose energy via excitation and ionization of the target atoms. If we call T the energy transfer in such collisions, we can write the energy loss per path length as

$$dE/dx = n \int T(d\sigma_{\text{ex}} + d\sigma_{\text{ion}}), \tag{2}$$

where n is the target density. PS194 also measured the energy loss of fast antiprotons in a wide range of solid targets, and compared the results with newly developed theory [59].

The measurements of the PS194 collaboration were performed with the direct LEAR beam which was often energy degraded in a stack of foils. It was possible in a few cases to obtain data for antiproton energies as low as 13 keV, but the bulk of the PS194 data belong to the "fast" collision regime, i.e., to antiproton energies higher than 25 keV (corresponding to a velocity of 1 au).

With the AD antiproton beam decelerated in the RFQ, the energy range of 5–190 keV can be reached. This is precisely what is needed for studies of the slowing down of slow antiprotons in matter. From a fundamental point of view, in this energy range the stopping phenomenon is greatly complicated by electron capture in the case of positive projectiles. However, no such complication exist for antiproton projectiles, and hence we can test for the first time low-velocity stopping power theory with a "frozen" projectile charge. Measurements of the energy loss of 5–190 keV antiprotons in thin solid Si targets and gaseous He targets are proposed.

With the addition of a Penning trap after the RFQ, we shall have access to antiproton beams of 1–10 keV. With such beams we suggest to investigate the ionization of atomic hydrogen, helium and other gas-atoms in single collision conditions. These are very fundamental, few-particle processes and it is important to obtain bench-mark cross section data for the advancement of many-body theory. Again, slow antiprotons are of special importance because for such projectiles there are no complications for theory due to electron capture. Furthermore, new and unexplored ionization phenomena are expected for impact of slow, negative, heavy projectiles such as Fermi-Teller ionization and quasi-adiabatic ionization. It is our intention to measure the cross sections for ionization of atomic hydrogen and helium for impact of 1–10 keV antiprotons.

1.3 Antiprotonic atom production and new slow antiproton facility

When a heavy particle with a negative charge e.g., an antiproton ($\bar{p}$), a negative pion (π^-), or a negative muon (μ^-), is injected into a dense medium, it loses its kinetic energy via multiple collisions down to $\sim$ eV region. Then, the negative particle is captured into a high-lying atomic orbital of the target atom (exotic atom formation), and cascades down to lower excited or ground states via Auger and/or radiative transitions, and decays or is absorbed by the target nucleus. As the formation takes place during thermalization, the resultant state distribution of the exotic atom is a weighted sum of the velocity dependent $\bar{p}A^+$ formation cross section and cascading. In the case of negative particles with strong interaction, the exotic atom annihilates immediately in dense media [60]. The only exception known until now is He target, e.g., the lifetime of $\bar{p}He^+$ has been found to be longer than $\sim \mu$s even under high target density. This characteristic feature has enabled high precision spectroscopy of $\bar{p}He^+$ (Appendix A). However, if the target is thin enough so that $\bar{p}A^+$s are isolated in vacuum and free from the quenching effect, various antiprotonic atoms are also expected to be metastable. The difficulty to produce such metastable states lay primarily in the fact that the available lowest energy of $\bar{p}$ was in the range of MeV, i.e., a high density target was inevitable to slow down and to effectively produce $\bar{p}A^+$.

We propose here to perform a comprehensive study of the collision dynamics in forming matter-antimatter complexes employing slow $\bar{p}$ beams from the RFQ and from the catcher trap, which will provide as many as 3×10^6 ultra slow antiprotons per minute either as a pulsed or as a continuous beam (Appendix C). In the year 2000 when the antiprotons from the RFQ will be available, a swarm type experiment is proposed to determine the velocity of the $\bar{p}$ at the moment of $\bar{p}A^+$ formation under multiple collision conditions. For this purpose, $\sim$ 50 keV antiprotons will be injected into a gas cell kept at 1 $\sim$ 10 Torr, where DC and/or AC electric fields will be applied to tune the drift velocity of antiprotons. Further, a channeling phenomenon of 10–100 keV $\bar{p}$ can be studied, which will provide, for the first time, a chance to study the behavior of slow, heavy, and negatively charged particles in a single crystal.

In the year 2001 and later, the initial stage of the antiprotonic atom formation will be studied by (i) shooting a $\bar{p}$ beam of 1 eV $\sim$ 1 keV on a thin gas target of $\sim 10^{-3}$ Torr and (ii) injecting particle beams such as H^- and He^+ of 10–100 eV, and supersonic He of $\sim$ meV onto cooled antiprotons in the trap. In both cases, the *single collision condition* is satisfied, and *isolated antiprotonic atoms* are prepared in a free space, which is essential to study the initial stage of $\bar{p}A^+$ formation processes (Appendix B). It is to be noted that various physical quantities such as the principal quantum numbers, the orbital angular quantum numbers, etc., are controllable parameters under the single collision condition. A prototype research in this direction has already been started as an atomic physics part of PS200.

Table 2 summarizes the scope of the present proposal in comparison with the PS205 and PS194 experiments at LEAR.

Table 2: *The scope of the present proposal in comparison with previous LEAR experiments.*

	At LEAR	Present proposal	Keywords
Mode $\bar{p}$ energy ($\bar{p}$ intensity)	Parasitic beam 5.8 - 21 MeV (10^{8-9}/pulse, 1 pulse/10min) (10^{4-5}/sec, continuous)	Dedicated 5.8 MeV (10^{7}/pulse, 1 pulse/min) 5 - 190 keV with RFQ ($\sim 10^{7}$/pulse, 1 pulse/min) 10 eV - 10 keV DC from Trap	High energy regime → Low energy regime
Laser wavelength accuracy	5 ppm	0.2 ppm	$\bar{p}$He$^+$ confirmation → High-precision test of 3-body theory
High resolution spectroscopy	Resolved by laser (3% accuracy)	Microwave-laser triple resonance (10^{-7} accuracy)	Level schemes established → Improve antiprotonic Rydberg constant Hyperfine splitting observed → QED test of the hyperfine structure Initial population and lifetimes → "Primordial" population Interaction with H_2 → Systematic study of quenching by H_2, D_2 and other atoms/molecules.
$\bar{p}$ energy loss	30 – 3000 keV Solid targets TOF measurements	5 – 190 keV from RFQ Si and He Electrostatic energy selection and analysis	High energy regime → Low energy regime
$\bar{p}$ channeling	1.4 MeV	$\sim$ 100 keV from RFQ	High energy regime → Low energy regime
$\bar{p}$ ionization	13 – 3000 keV Atomic hydrogen Noble gases Molecules Single and multiple ionization	1 – 10 keV from Trap Atomic hydrogen Noble gases Single and double ionization	Fast collisions → Adiabatic collisions of few-body systems
$\bar{p}$ capture	——	50 keV from RFQ 10 - 100 eV from Trap	→ $\bar{p}$ drift in dense media → Initial stage of $\bar{p}$ atom formation → Search for stable $\bar{p}$ atoms in vacuum

2 $\bar{p}He^+$ atomcule spectroscopy using the 5.8 MeV Beam of the AD

The first year at AD

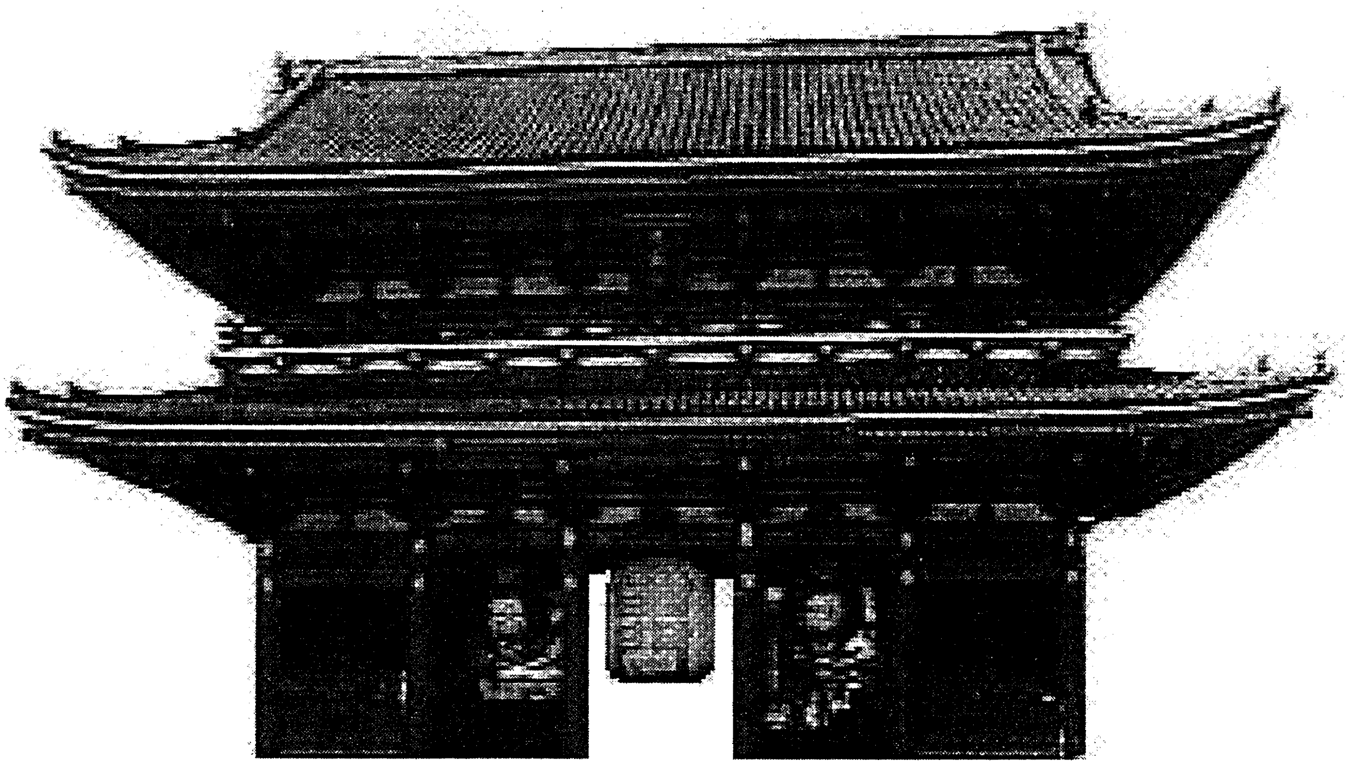

Kaminari-mon Gate of Senso-ji Temple, Asakusa, Tokyo

2.1 Higher resolution spectroscopy of antiprotonic helium atomcules

In the former series of laser resonance experiments, transition energies of $\bar{p}He^+$ atomcules have been measured with 10^{-5} precision, showing good agreement with the theoretical calculations [45] (see Fig. 3). The comparison between experiment and theory has now come to a state where we can discuss relativistic corrections to the level energies. Intensive studies of this are going on also on the theoretical side. Fig. 5 shows the most update value of the $(39,35) \rightarrow (38,34)$ wavelength, which is obtained after precise calibration as well as correction for the measured pressure shift, in comparison with the most advanced theoretical values [45, 48–51]. With the higher resolution available with the new proposed laser system (bandwidth ~ 600–900 MHz) and simultaneous calibration of the frequency against standard atomic lines together with a higher-precision wavelength meter, the resonant transition energies can be determined with a precision down to 10–100 MHz. The following problems will be addressed.

a) A more stringent test of theory to the level of 10^{-7}–10^{-8}. No such experimental precision has ever been achieved for any three-body systems. The best theoretical values presently available show a systematic deviation from the experimental ones (see Fig. 3). The improved experimental precision will stimulate the three-body theory including QED and other higher-order corrections.

b) More hyperfine splittings will be revealed. The better laser resolution to be achieved will facilitate multiple resonance spectroscopy, as will be discussed later.

c) More abundant information on the pressure shifts of various resonance lines (see the next section below).

d) Precision study of the influence of collisions with other atoms on level energies, populations and lifetimes, etc.

2.2 Shift and width measurements of resonances

Precise observations of the resonance profiles give information on the inter-atomic interactions in high-density targets. With the improved resolution the density shift of the resonance frequencies stated in Section A.2 can be studied more accurately. Also, the widths of the collisional broadening will be studied at a very low power-density of the laser, which is needed in order to reduce power broadening. These systematic observations of the density shift and the broadening for many more resonance transitions will reveal the interaction potential between $\bar{p}He^+$ and helium atom, thus giving a hint concerning the quenching mechanism of metastable states in dense medium as discussed in Section A.3.

So-far observed shifts were always proportional to the density of the helium target, but it is interesting to do the measurements for liquid helium targets, in which the $\bar{p}He^+$ atomcules interact with many surrounding atoms at the same time, and may then form clusters. Enormously large shifts and very broad widths of the resonances, as discovered in the spectroscopy of alkaline and alkaline-earth atoms in liquid helium [52, 53], may be observed also for the $\bar{p}He^+$ atoms.

All these measurements are also awaited on $\bar{p}\,^3He^+$ atomcules, where the level structure is similar but level lifetimes are much different [17, 28].

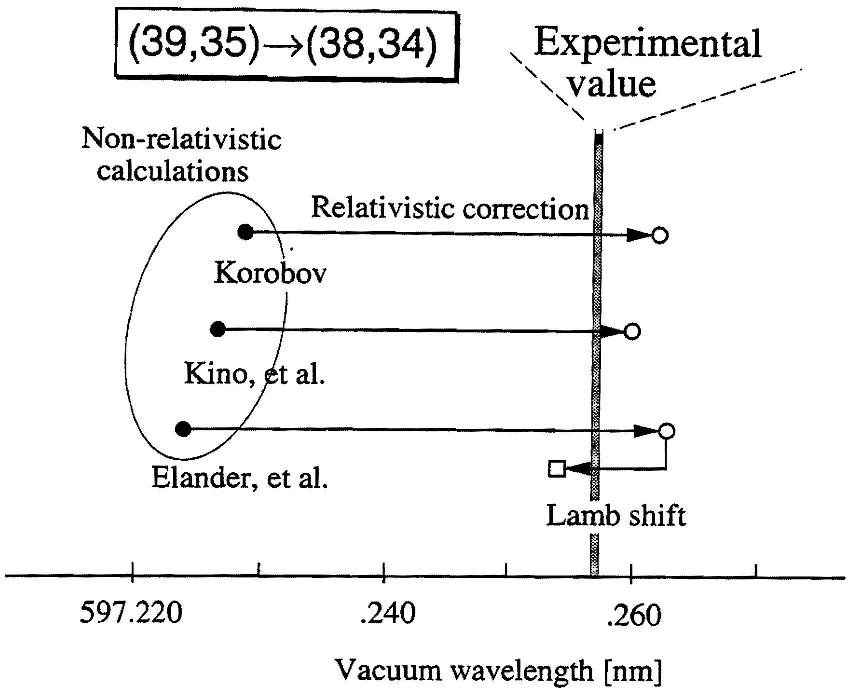

Figure 5: *The experimental value of the (39,35)→(38,34) wavelength is compared with recent theoretical values [45, 49, 51], which agree with several-ppm order precisions.*

2.3 Chemical physics aspects of $\bar{p}He^+$ atomcules

The application of the laser resonance method to microscopic studies of the quenching of the $\bar{p}He^+$ atomcule by H_2 and O_2 at LEAR [21, 22, 26, 29] has opened a chemical physics research domain, which will be matured in the coming AD era. The exotic nature of the $\bar{p}He^+$ atomcule from the viewpoints of chemical physics is as follows. The $\bar{p}He^+$ atomcule is a pseudo hydrogen *à la* e^--$\bar{p}He^{2+}$, but one in which the effective nuclear charge as seen from the e^- is around $1.7e$, the e^- binding energy is around 25 eV, etc. The other constituent $\bar{p}$ has a large angular momentum and is distributed in a quasi-classical orbit near the e^- and intervenes in the e^- behavior. The binding of $\bar{p}$ and e^- is reciprocal in the sense that a shallower binding of the e^- implies a deeper binding of the $\bar{p}$ and vice versa. All such properties of the bound e^- and $\bar{p}$ including their spatial distributions vary according to the quantum numbers (n, l). So, the $\bar{p}He^+$ atomcule is a pseudo hydrogen with rich internal degrees of freedom that can be tagged by laser resonances and its studies in foreign atom/molecule environment will provide important information on chemical physics.

One of the surprising effects found at LEAR was that higher-lying states are quenched more efficiently by a small H_2 admixtures than lower-lying ones. No explanation has yet been found for this effect, which depopulates higher-lying states more effectively than lower-lying ones and therefore permits upward or inverse transitions to be excited by laser stimulation. We will continue to study the mechanism in more detail by extending this method to other states, by i) measuring the lifetime-shortening for the $n = 37$ states from the time dependence of inverse resonance intensities $n = 37 \to 38$, ii) extending inverse resonances to $n = 36 \to 37$, successively, and iii) studying higher-v and higher-n states using unfavoured resonances.

It is also important to study the quenching mechanism with D_2 molecules. Since the D_2 molecule has a denser rotation/vibration energy level scheme and a heavier mass, their interactions in comparison with H_2 will clarify the quenching mechanism.

The quenching behavior depends on the foreign atoms/molecules. We already know that O_2 molecules destroy the $\bar{p}He^+$ in a very much different way from the case of H_2. We will study various reactions systematically.

2.4 Search for other resonances and determination of the lifetimes and populations

We have so far found 13 resonant transitions for $\bar{p}^4He^+$ atomcules and 3 for $\bar{p}^3He^+$. The populations of these metastable states have been deduced (see Section A.3), but still more than half of the metastable population which contributes to the delayed annihilation has not been identified. One reason for this deficiency is that in most of our experiments, the laser resonances were detected only after 1.3 μs from the moment of the $\bar{p}He^+$ atom birth and the important early-time range was lacking. This will certainly be improved in the AD era.

We will therefore search for the unknown states indicated in Table 3 and determine their lifetime and populations by the well-established method described in A.3. The HAIR method (see Section A.4) will be extensively applied not only for favoured transitions but also for $\Delta v = 2$ unfavoured transitions. As shown in Fig. 6 the $\Delta v = 2$ transitions occur between pairs of states with larger lifetime differences. In this way, since the state population can be artificially reduced step by step (from upper to lower), virtually all the metastable states will be covered.

Table 3: *Laser resonance transitions of $\bar{p}^4He^+$ to be searched for the determination of the lifetimes and populations. See Fig. 2 for the assignments of the transitions.*

Transitions	Wavelength (nm)	Type	Condition
$(40,35) \rightarrow (39,34)$	672.8	$\Delta v = 0$	pure He
$(39,l) \rightarrow (40,l+1)$	672.8 - 679.4	$\Delta v = 0$	H_2
$(40,l) \rightarrow (41,l+1)$	759.0 - 776.1	$\Delta v = 0$	H_2
$(41,l) \rightarrow (42,l+1)$	853.0 - 890.5	$\Delta v = 0$	H_2
$(38,l) \rightarrow (39,l+1)$	597.3 - 597.6	$\Delta v = 0$	H_2
$(37,l) \rightarrow (38,l+1)$	527.9 - 529.6	$\Delta v = 0$	H_2
$(36,l) \rightarrow (37,l+1)$	468.1 - 470.7	$\Delta v = 0$	H_2
$(35,l) \rightarrow (36,l+1)$	416.3, 417.9	$\Delta v = 0$	H_2
$(39,l) \rightarrow (40,l-1)$	973.1 - 1066.3	$\Delta v = 2$	pure/H_2
$(38,l) \rightarrow (39,l-1)$	841.7 - 884.5	$\Delta v = 2$	pure/H_2
$(37,l) \rightarrow (38,l-1)$	713.6 - 740.5	$\Delta v = 2$	pure/H_2
$(36,l) \rightarrow (37,l-1)$	616.7, 625.6	$\Delta v = 2$	pure/H_2

The study of the level lifetimes and population for $\bar{p}^3He^+$ gives further interesting isotope comparisons. The planned experiment is summarized in Table 4.

It is interesting that the metastability of the $\bar{p}He^+$ states is retained in dense gas, liquid, and solid phases, despite the frequent collisions with the surrounding helium atoms [1,8–10]. In recent work done at LEAR, we measured the lifetimes of a limited number of $\bar{p}He^+$ states in the $v = 2$ and 3 cascade chains [25]. It appears that collisions with external helium atoms reduce state lifetimes more strongly for lower-lying states in the sequential order (n,l)=$(37,34)$ and $(38,35)$, while they leave the energetically higher-lying state $(39,35)$ unaffected. At present, we have no quantitative

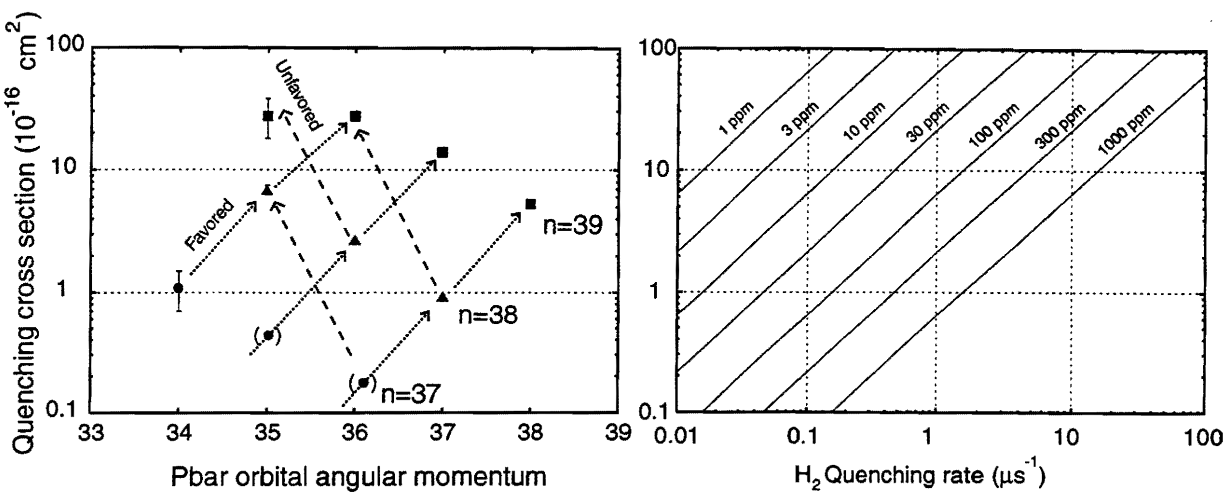

Figure 6: *(Left) The (n, l) dependence of the quenching cross section σ_q, deduced from the HAIR experiment [26]. (Right) The σ_q is converted to the quenching rate of the state for various H_2 concentrations in the "standard" medium condition (30K, 1 bar).*

Table 4: *Laser resonance transitions of $\bar{p}\,^3He^+$ to be searched for isotope comparison and for the determination of the lifetimes and populations.*

Transitions	Wavelength (nm)	Type	Condition
$(39, 34) \to (38, 33)$	670.8	$\Delta v = 0$	pure He
$(38, l) \to (39, l+1)$	670.8 - 679.6	$\Delta v = 0$	H_2
$(37, l) \to (38, l+1)$	593.4 - 594.6	$\Delta v = 0$	H_2
$(36, l) \to (37, l+1)$	522.8 - 524.2	$\Delta v = 0$	H_2
$(35, l) \to (36, l+1)$	461.5 - 464.0	$\Delta v = 0$	H_2
$(34, l) \to (35, l+1)$	408.7, 410.2	$\Delta v = 0$	H_2
$(38, l) \to (39, l-1)$	1007.7 - 1080.7	$\Delta v = 2$	pure/H_2
$(37, l) \to (38, l-1)$	843.1 - 889.7	$\Delta v = 2$	pure/H_2
$(36, l) \to (37, l-1)$	710.6 - 739.44	$\Delta v = 2$	pure/H_2
$(35, l) \to (36, l-1)$	611.5 - 620.5	$\Delta v = 2$	pure/H_2

understanding of the mechanisms that cause this state-dependent lifetime shortening, because it involves the treatment of at least 4-body atomic collisions (the helium nucleus, antiproton, and electron in the $\bar{p}He^+$ atom, plus the external helium atom) which are beyond the scope of established calculation methods.

We propose the continuation of systematic studies to determine the density dependence of the lifetimes of $\bar{p}\,^4He^+$ states over a wider range of (n, l), especially those in the $v = 0$ and 1 cascades which contain the majority of the metastable states, and those in the higher-lying region $n > 41$ which are so far undetected. Limited data on the $\bar{p}\,^3He^+$ metastable states suggests that as the target density is increased, lower-lying states are more strongly affected in the sequential order

(36, 33), (37, 34), and (34, 38). Further measurements would yield detailed data on the density dependence of the state lifetimes which can be compared with those of $\overline{\mathrm{p}}^4\mathrm{He}^+$ states.

2.5 New spectroscopy of hyperfine and superhyperfine structure

2.5.1 Hyperfine and superhyperfine structure

The $\overline{\mathrm{p}}\mathrm{He}^+$ atomcule has three angular momenta; L: orbital angular momentum (mainly carried by $\overline{\mathrm{p}}$), S_p: $\overline{\mathrm{p}}$ spin and S_e: electron spin. Let us define the angular momentum coupling as follows:

$$\vec{F} = \vec{L} + \vec{S_e} \tag{3}$$

$$\vec{j} = \vec{L} + \vec{S_p} \tag{4}$$

$$\vec{J} = \vec{F} + \vec{S_p} = \vec{j} + \vec{S_e} = \vec{L} + \vec{S_p} + \vec{S_e} \tag{5}$$

As mentioned above, the dominant effect is a doublet ($F^+ = L + 1/2$ and $F^- = L - 1/2$, separated by ν_{HF}) caused by the interaction of the spin-averaged $\overline{\mathrm{p}}$ magnetic moment (due to the large L) with the electron spin. This splitting is called *Hyperfine (HF) Structure.* The $\overline{\mathrm{p}}$ spin causes an additional smaller splitting for each of the HF state, which is called here *Super Hyperfine (SHF) Structure.*

The HF and SHF structure has been calculated by Bakalov and Korobov [39, 46] using the best three-body wavefunctions of Korobov [44]. The level and transition scheme involving both HF and SHF is shown in Fig. 7. The HF and SHF energies are presented in terms of the angular momentum operators as

$$\delta E = E_1(\vec{L}\cdot\vec{S_e}) + E_2(\vec{L}\cdot\vec{S_p}) + E_3(\vec{S_e}\cdot\vec{S_p}) + E_4\{2L(L+1)(\vec{S_e}\cdot\vec{S_p}) - 6(\vec{L}\cdot\vec{S_e})\cdot(\vec{L}\cdot\vec{S_p})\} \tag{6}$$

The first term gives a dominant HF splitting.

The lower and the upper states of a HF doublet have F^+ and F^-, respectively. Their level order is opposite to that of the hydrogen atom, because of the opposite sign of the "nuclear magnetic moment". The SHF structure is a combined effect of i) (the second term) the one-body spin-orbit interaction (called historically *Fine Structure*, but small in the present case, because of the very large (n, L)), ii) (the third term) the contact term of the $\vec{S_p} - \vec{S_e}$ interaction and iii) (the fourth term) the tensor term of the $\vec{S_p} - \vec{S_e}$ interaction. According to the calculation, the contact and the tensor terms almost cancel and the SHF splitting is nearly equal to the one-body spin-orbit splitting as given by the second term. Thus, its level order (the $j^- = L - 1/2$ level is lower than the $j^+ = L + 1/2$ level) is retained here; the $F^+ = L + 1/2$ member is split into lower $J^{+-} = F^+ - 1/2 = L$ and upper $J^{++} = F^+ + 1/2 = L + 1$ submembers, and the $F^- = L - 1/2$ member is split into lower $J^{--} = F^- - 1/2 = L - 1$ and upper $J^{-+} = F^- + 1/2 = L$ submembers, as shown in Fig. 8.

Because of the large L the HF and SHF magnetic dipole transitions as well as the electric dipole laser transitions are subject to the selection rule $\Delta S_e = \Delta S_p = 0$. This means that, although the HF/SHF level splittings are large, the splittings in the transition frequencies are small. The first successful observation of a HF splitting in the (37,35) → (38,34) used an "unfavoured transition", where the difference of the HF splitting between the parent and daughter states is unusually large (see section 1.1). Our initial study at AD will focus on this particular laser transition. The laser transition wavelength and the microwave resonance frequencies are listed in Table 5, together with other candidate transitions for further systematic studies.

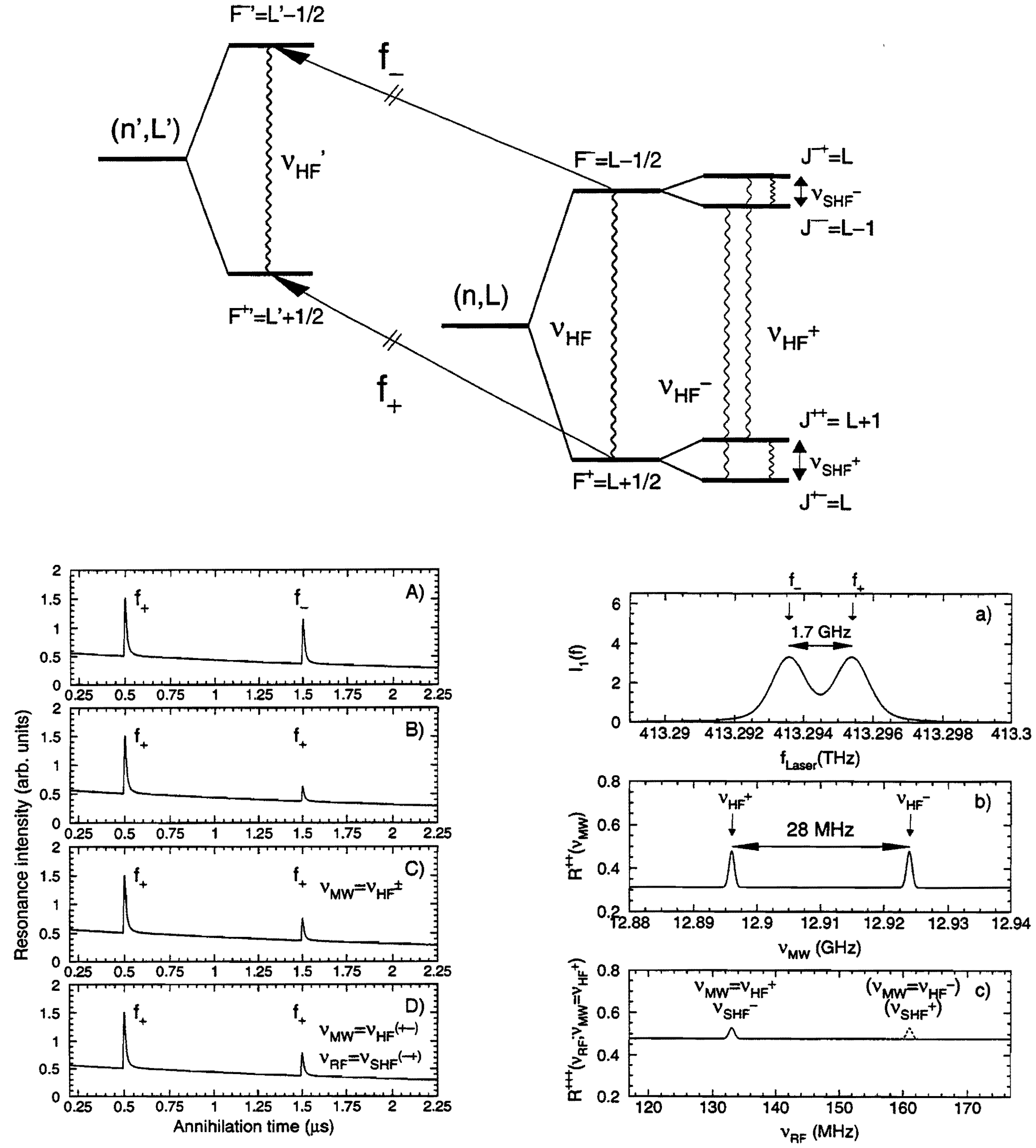

Figure 7: *(Top) Laser, microwave and r.f. transitions in* $\bar{p}He^+$*. (Bottom left) Simulated delayed annihilation time spectra of the laser/microwave triple resonance method. (Bottom right) Simulated microwave resonance profile.*

Most of the candidates are hydrogen-assisted inverse resonances (HAIR) of the unfavoured $\Delta v = 2$ type. The HAIR method provides not only a wide variety of resonances by tuning the H_2 concentration so that the quenching rate of the parent state is around 1 μs^{-1}, but also suppresses the feeding from the upper states since their lifetimes are changed to 100 ns or shorter. This feature is very helpful in the multiple resonance methods.

Table 5: *The laser transition wavelength and the microwave resonance frequencies. The values for* $\Delta\nu$, ν^+_{HF}, ν^-_{HF}, ν^+_{SHF}, *and* ν^-_{SHF} *are given in GHz.*

Transitions	λ (nm)	Conditions	$\Delta\nu$	ν^+_{HF}	ν^-_{HF}	ν^+_{SHF}	ν^-_{SHF}
(39,38) → (40,37)	1066.5	100 ppm H_2	1.890	12.414	12.523	0.139	0.031
(39,37) → (40,36)	1030.5	30 ppm H_2	1.754	11.767	11.867	0.144	0.043
(38,37) → (39,36)	884.64	600 ppm H_2	1.914	13.087	13.157	0.143	0.073
(38,36) → (39,35)	861.71	300 ppm H_2	1.779	12.381	12.448	0.151	0.084
(37,36) → (38,35)	740.53	3000 ppm H_2	1.894	13.639	13.665	0.149	0.122
(37,35) → (38,34)	726.10	pure He	1.767	12.896	12.924	0.161	0.133

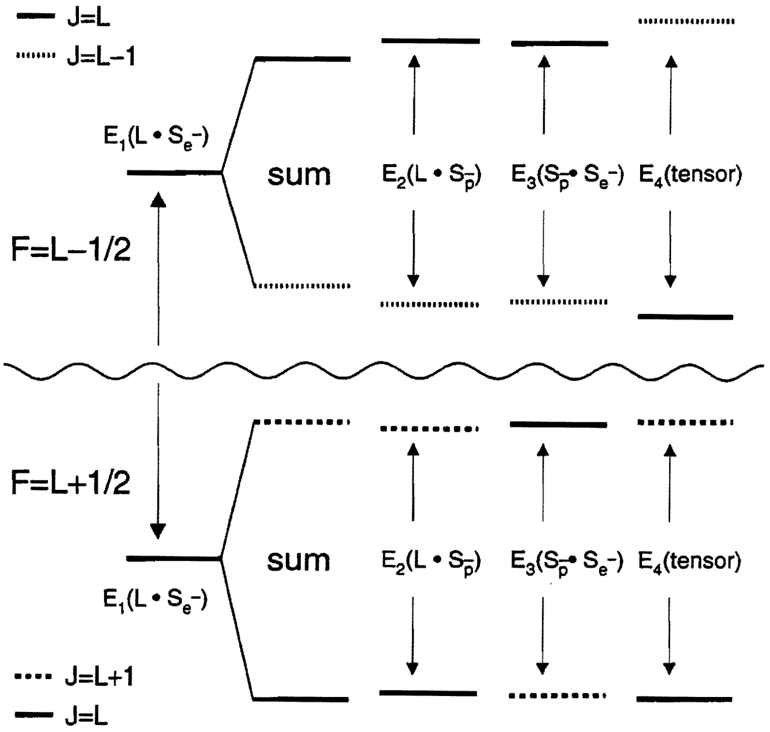

Figure 8: *Contribution of the different interactions to the level splitting of the* (n, l) = *(37,35) state in* $\bar{p}He^+$ *according to theoretical calculations [46]. The final level order of the small doublets labeled sum results from the addition of the three contributions plotted to the right. Due to the cancellation of the scalar* $(E_3(\vec{S}_e \cdot \vec{S}_p))$ *and tensor* $(E_4(\text{tensor}))$ *spin-spin parts, the level order is determined by the* $\bar{p}$ *spin-orbit interaction* $(E_2(\vec{L} \cdot \vec{S}_p))$.

2.5.2 Significance of hyperfine studies

There is a long history on the physics of fine and hyperfine structure of atoms which has provided important information on quantum physics and QED. The $\overline{\mathrm{p}}\mathrm{He}^+$ atomcule is a newcomer, and will occupy an important role, lying next to the fundamental two-body system of hydrogen atom, muonium and positronium. It is an extremely exotic yet fundamental three-body system, composed of a $\overline{\mathrm{p}}$, an e^- and the nucleus. With the advent of both experimental and theoretical progress of $\overline{\mathrm{p}}\mathrm{He}^+$ spectroscopy the state of art is now matured enough to handle the hyperfine/superhyperfine structure of this atomcule to high precision. In the following we discuss briefly what we can learn from the proposed studies.

i) Hyperfine structure (ν_{HF})

The ultimate precision is limited by the natural width of the metastable state (order of 1 MHz) and its uncertainty of the microwave resonance can be reduced to 1 kHz or so on the 12.9 GHz microwave transition frequency. Thus, we expect a relative precision of 10^{-7}. The theoretical values calculated with the best Korobov wavefunctions have 6 digit precision. The theory can be tested to such high precision. A disagreement between theory and experiment, if revealed, will give insight into the three-body wavefunctions, the orbital magnetic moment of $\overline{\mathrm{p}}$ and QED corrections. It should be noted that the orbital magnetic moment of the proton has never been known (except for the large mesonic correction as much as 10 % when the proton orbital is inside the nucleus) simply because there is no atomic system in which a proton is orbiting (only protons jumping into an antimatter world could produce such a situation!!) In contrast, we can examine the orbital g-factor of $\overline{\mathrm{p}}$ in our atomcule.

ii) Superhyperfine structure (ν^-_{SHF} and ν^+_{SHF})

The two SHF frequencies jointly provide well separated information on the one-body spin-orbit term and the spin-spin term. If a doublet structure is observed in the laser/microwave triple resonance and its splitting is indeed small, as predicted ($\sim$ 28 MHz in the case of the (37,35) state), this will indicate that the one-body spin-orbit term is dominant, since the $\vec{S}_p \cdot \vec{S}_e$ term should contribute to the upper and the lower doublets in opposite directions.

The spin-orbit splitting of leptonic particles is well known. For hadronic particles, which are subject to enormous structural corrections ($\mu(p)/\mu_N = 2.79 = 1 + a_p$), the spin-orbit term is proportional to

$$(1 + 2a_p)\vec{s} \cdot \vec{l}. \tag{7}$$

This large correction has not even been tested for a protonic system, because of the absence of a "protonic atom" with a large proton orbital angular momentum. For $\overline{\mathrm{p}}$, in contrast, this term can be measured from spin-orbit doublets of antiprotonic atoms. The best known case is from the fine structure of the $n = 11 \rightarrow 10$ x ray transition of $\overline{\mathrm{p}}$ Pb [61], in which this term was tested to the precision of 3×10^{-3}. The ν^-_{SHF} and ν^+_{SHF} will provide a more stringent test of this term (or equivalently, the magnetic moment of $\overline{\mathrm{p}}$).

2.5.3 2-laser/microwave triple resonance method

Even with an improved laser resolution in the AD era, the laser spectroscopy alone will provide a value of poor precision for the difference $\Delta\nu = \nu^{\mathrm{parent}}_{\mathrm{HF}} - \nu^{\mathrm{daughter}}_{\mathrm{HF}}$, since it measures the difference of two large numbers. We need a new spectroscopic method to directly measure the HF/SHF transitions. Here, we present a laser/microwave triple resonance method to determine $\nu_{\rm HF}$ for which these tests were began at LEAR.

While muonium hyperfine spectroscopy makes use of the muon polarization and asymmetric decay, the present $\bar{\rm p}{\rm He}^+$ case cannot. In order to measure the hyperfine splitting we have to cause a population asymmetry of the doublet and to detect its time evolution induced by the resonant emission/absorption of microwave. We have already utilized two successive laser pulses to empty the resonant state population by the first laser pulse and to detect its recovery by the second pulse. This "t_1-t_2 method" was originally used to determine the lifetime of the parent state[18], and can now be extended to hyperfine studies, as far as the hyperfine doublet is resolved in laser resonance (Fig. 7). Namely, the intensity ratio of the second resonances

$$R^{++}(\nu_{\rm MW}) = \frac{I_2(f_1 = f^+, f_2 = f^+)}{I_2(f_1 = f^+, f_2 = f^-)} \tag{8}$$

reflects the recovery of one member of the hyperfine doublet after time t $(= t_2 - t_1)$ (see A) and B) of Fig. 7). The recovery is caused not only by the feeding from upper excited states but also by any change of population between the hyperfine doublet states. If we can cause a state equilibration by microwave resonance fast enough before the normal feeding (typically, around 1 μs), we can detect the microwave resonance and immediately determine the resonance frequency $\nu_{\rm HF}$ to a high precision, as shown in b) of Fig. 7. This method is called *Laser/Microwave Triple Resonance Method.* The central frequency in the case of (37,35) → (38,34) is predicted to be 12.9 GHz.

To be more precise, the microwave resonance is not a single peak because each HF doublet state has an additional SHF doublet and thus consists of two components:

$$\nu^+_{\rm HF} = \nu_{\rm HF} + \frac{2L-1}{4L}\nu^-_{\rm SHF} - \frac{2L+1}{4L+4}\nu^+_{\rm SHF} \tag{9}$$

$$\nu^-_{\rm HF} = \nu_{\rm HF} - \frac{2L+1}{4L}\nu^-_{\rm SHF} + \frac{2L+3}{4L+4}\nu^+_{\rm SHF} \tag{10}$$

$$\Delta\nu_{\rm HF} = \nu^+_{\rm HF} - \nu^-_{\rm HF} = \nu^-_{\rm SHF} - \nu^+_{\rm SHF} \tag{11}$$

The splitting is a small difference of the two SHF energies, around 28 MHz in the case of the $(37,35) \to (38,34)$ transition.

The state inversion frequency (like Rabi frequency in laser resonance) depends on the magnitude of the oscillating magnetic field (H_1) as given by

$$\frac{\Gamma_{MW}}{2\pi} = \frac{1}{2\pi}\frac{1}{8\hbar}g_e\mu_B H_1 = 0.350 \text{ MHz/G} \times H_1 \tag{12}$$

To cause a detectable resonance effect at $t_2 = t_1 + 1$ μs we need $H_1 \sim 3$ Gauss.

2.5.4 Future scope

A resolved microwave resonance profile, as shown in b) of Fig. 7, is informative on the superhyperfine interaction, especially on the spin-spin part, because only the spin-spin interaction contributes to such an asymmetric energy diagram. However, the information on $\nu_{\rm SHF}$ is poor, since $\nu_{\rm HF}$ ($\sim$ 28 MHz) is a small fraction of $\nu_{\rm SHF}$ ($\sim$ 130 MHz). For precise determination of $\nu_{\rm SHF}$ we have to cause RF transitions ($\nu_{\rm RF} = \nu^-_{\rm SHF} \sim 130$ MHz and $= \nu^+_{\rm SHF} \sim 160$ MHz). The RF resonance will affect the 2-laser resonance intensity ratio R under the resolved microwave resonance condition:

$$R^{+++}(\nu_{\rm RF}) = \frac{I_2(f_1 = f^+, f_2 = f^+, \nu_{\rm MW} = \nu^+_{\rm HF})}{I_2(f_1 = f^+, f_2 = f^-, \text{no MW})}, \tag{13}$$

because the MW/RF double resonance enhances the feeding to J^{++} (see D) of Fig. 7). Therefore, the quadruple resonance can be detected from the above ratio as a function of ν_{MW} (see c) of Fig. 7) and precise information on ν^{-}_{SHF} and ν^{+}_{SHF} will be obtained.

The quadruple resonance is by one order of magnitude more difficult than the triple resonance, and will be pursued only after we succeed in the latter.

2.6 Improvement and adoption of instruments for the AD

2.6.1 Laser system

The pulsed-laser system to be used for all proposed experiments must have as narrow a bandwidth as possible with a high power stable from shot to shot to assure high resolution and constant depopulation efficiency; these are critical especially for the laser-microwave resonance studies discussed in 2.5. Actually, much better laser beam quality and smaller power fluctuations are required in the new measurements using pulse-extracted antiproton beams, than in the former experiments using slow extraction where large numbers of laser shots were averaged.

We have investigated several kinds of laser systems, and the best solution for these requirements turned out to be a YAG-pumped dye laser (see Fig. 9), with a single-mode 600–900 MHz linewidth and a clean spatial and temporal Gaussian profile. This system has lower power fluctuations and smaller time jitter than the excimer lasers used in the former series of experiments. It can produce pulses with 30 mJ power for the whole visible-light range with fluctuations less then 1% for each shot.

It must be noted that the YAG laser requires a trigger for the flash lamp which should precede another trigger for the ignition. We have confirmed with the PS division that accurate timing signals from the AD can be available prior to the extraction by 250 μs.

2.6.2 Beam and annihilation detectors

The detectors and data acquisition systems are basically extensions of those used in previous experiments at LEAR, with particular emphasis on improving time resolution and signal-to-noise ratio.

In the AD, a 200 ns-long antiproton bunch containing 10^7 particles will be injected into the cryogenic helium gas target. The XY profile of this beam will be measured to a resolution of 0.5 mm by a parallel plate ionization chamber, placed immediately upstream of the target. Some 97% of the incoming antiprotons annihilate promptly in the helium gas; the decay products from this prompt annihilation (mostly charged pions) will be detected by a Lucite Čerenkov counter, so that the intensity of each beam pulse can be obtained.

The remaining 3% of the antiprotons form metastable $\bar{\mathrm{p}}\mathrm{He}^+$ atoms that annihilate with an average lifetime of 3 μs; this delayed annihilation time spectrum (DATS) will be measured by the annihilation counter equipped with a special gated fine-mesh photomultiplier which was already tested at LEAR and is further being developed by Hamamatsu Photonics Co. During the initial 200 ns after the first antiprotons of the AD pulse arrive, this photomultiplier will be switched off by reversing the potential of several dynode electrodes, thereby protecting the photomultiplier from being overloaded by promptly annihilating antiprotons. Immediately following the prompt annihilation, the PMT will be switched on and the delayed annihilation time spectrum is measured. The photomultiplier is being designed to have wide-band timing characteristics, so that both the ~ 3 μs DATS lifetime of spontaneously decaying $\bar{\mathrm{p}}\mathrm{He}^+$ atoms and the ~ 5 ns-long laser resonance spike can be accurately measured.

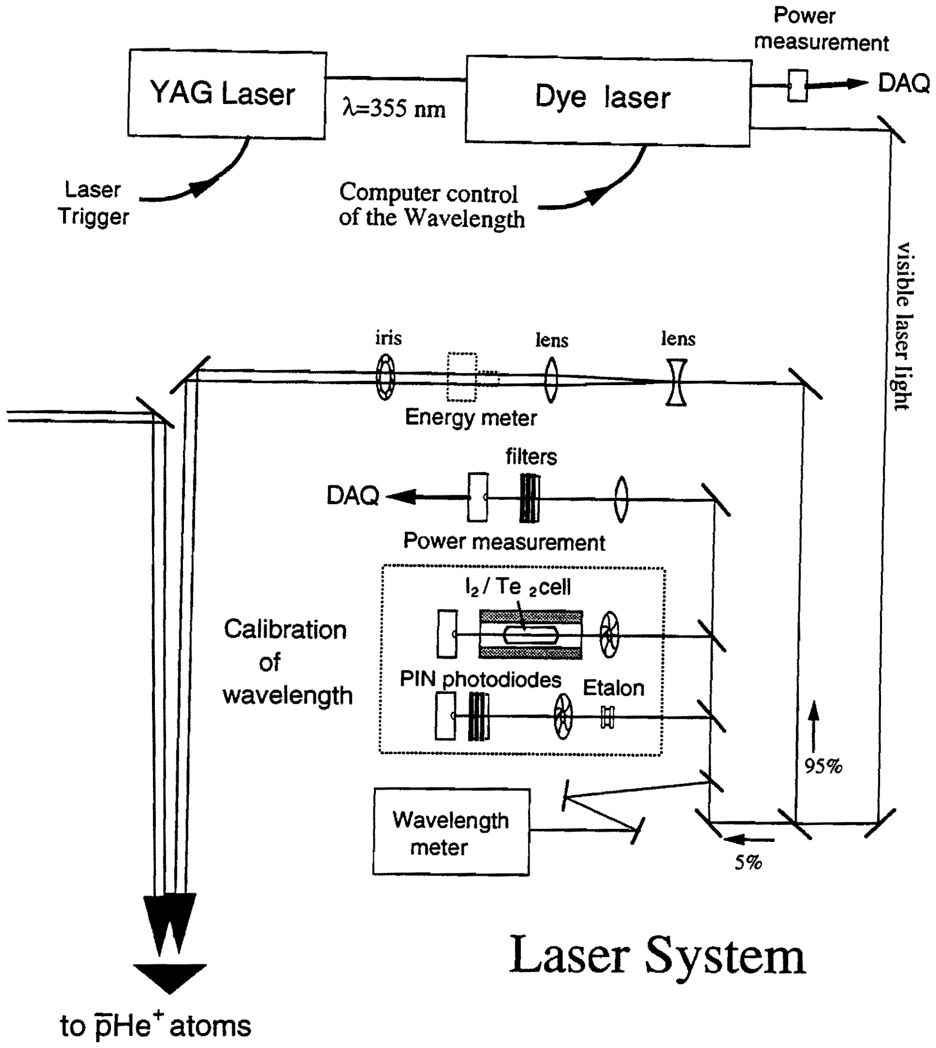

Figure 9: *A schematic of the new laser system proposed for the* $\bar{p}He^+$ *spectroscopy experiments. Two identical YAG-pumped dye lasers. The wavelength of each laser shot is measured with a highly precise wavelength meter, and the absorption signals through standard molecular cells are also referred to as calibration data.*

The analog signal from the PMT will be measured over a $\sim$ 20 μs interval by a high-speed digital oscilloscope (1 GHz analog bandwidth, 8 GHz digital sampling rate) designed especially for the accurate recording of transient signals, and the digitized data will be transferred to an external Windows-NT workstation over a TCP/IP ethernet link.

2.6.3 Laser/microwave resonance experiment

The experiment to measure the hyperfine splitting as described in Section 2.5 needs, in addition to the narrow bandwidth pulsed laser system, a microwave generation system which produces a magnetic field with an amplitude of $H_1 \geq 3$ Gauss at the stopping position of the antiprotons. The microwave cavity is filled with helium gas which must be kept at cryogenic temperatures to keep the Doppler broadening of the laser resonance line small enough (at $T = 10$ K the Doppler broadening amounts to ~ 430 MHz, at $T = 5$ K to ~ 300 MHz for $\lambda = 726$ nm!).

Theoretical calculations showed [39,45] that the splitting in a laser transition in the case of favoured transitions is in the order of 100 to 500 MHz. This might be smaller than the achievable intrinsic linewidth of a resonance under our experimental conditions, which is dominated by power broadening, collision al broadening, and Doppler broadening. Therefore it would probably be very difficult to resolve a line splitting in a favoured transition, even if a laser system with a smaller bandwidth could be used.

The situation is different in the case of unfavoured transitions as the already observed $(37,35) \rightarrow (38,34)$ transition where $\Delta\nu_{\mathrm{HF}} = 1.7$ GHz was found. Table 5 shows that similar values are expected for other unfavoured transitions in the metastable region, the maximum value being ~ 1.9 GHz. In this case the splitting can be at least partially resolved using a YAG-pumped dye laser with 600–900 MHz bandwidth as described in Section 2.6.1, although its pulse length of $\sim 4-6$ ns is shorter than the Auger lifetime of some of the daughter states of unfavoured transitions, so that a single pulse can achieve only $\sim 50\%$ depletion efficiency. In these cases a sequence of several pulses separated just by the pulse length might be applied.

A magnetic field of at least 3 Gauss at a frequency range of 11.5–14 GHz (cf. Table 5) can be most easily generated using a cavity excited by a micro-wave generator like a travelling-wave tube amplifier (TWTA) through a standard waveguide (see Fig. 10). The cavity has to also hold the helium gas which has to be kept at temperatures below 10 K. In a test experiment at LEAR in 1996 we have already shown that the combination of micro-wave supply through a waveguide into a gas chamber kept at $T = 5$–6 K and filled with helium gas of 0.5–1 bar pressure inside a bath-type helium cryostat is feasible [28].

A cavity resonator is characterized by the "quality factor" Q defined as

$$Q = 2\pi \times \frac{\text{time averaged electromagnetic energy}}{\text{energy loss per cycle}}. \tag{14}$$

The stored electromagnetic energy can be calculated from the electric and magnetic field whose distributions are determined by the cavity shape and dimension. For an isolated cavity, the losses are given by the resistive losses through the induced currents in the surface of the walls and depend on material parameters (conductivity and skin depth). If the cavity is excited by an external circuit, the losses will be increased and the Q value decreases (*"loaded"* Q_L).

The frequency dependence of the magnetic (and electric) field $H(\nu)$ $(E(\nu))$ inside a cavity is given by a curve centered around a frequency ν_0 determined — in the case of weak coupling to the exciting circuit — by the shape and the dimensions of the cavity. The bandwidth BW is defined as the width of the resonance curve at the point where the field drops by -3 dB, i.e. by a factor of $\sqrt{2}$, from the maximum value H_0. H_0 is a factor $\sqrt{Q}$ larger than the excitation field outside the cavity.

Scanning the frequency can be performed either by changing the dimensions of the cavity (*mechanical tuning*) or by using a synthesizer with smaller bandwidth than the cavity (*synthesizer tuning*). In the latter case, the frequency of the field can be scanned within the resonance curve, and the field amplitude will follow this curve. Since the experiments have to be performed at liquid helium temperatures, mechanical tuning would require a rather complex construction.

Table 5 shows that the scan range will be of the order of $(\nu_{\mathrm{HF}}^{+} - \nu_{\mathrm{HF}}^{-})/\overline{\nu}_{\mathrm{HF}} = 0.2$–$1\%$ ($\sim$ 30–100 MHz), where $\overline{\nu}_{\mathrm{HF}} = (\nu_{\mathrm{HF}}^{+} + \nu_{\mathrm{HF}}^{-})/2$. For synthesizer tuning a loaded $Q_L \leq 100$ is therefore required. On the other hand, the enhancement of the field strength will be only a factor $\sqrt{Q_L} \leq 10$, requiring a larger power at the microwave source.

Our current design is based on a cylindrical cavity oscillating in the TM110 mode. For this mode the resonance frequency ν_0^{110} is independent of the cavity length and only determined by the radius a [54]:

$$\nu_0^{110} = \frac{c x_{11}}{2a\pi}, \tag{15}$$

where $c = 2.99792 \times 10^8$ m/s is the speed of light and $x_{11} = 3.8317$ is the first root of the corresponding Bessel function J_1. For the (37,35) → (38,34) transition with $\overline{\nu}_{\rm HF} = 12.910$ GHz, the diameter turns out to be $2a = 2.832$ cm. The length l of the cavity has to be chosen to avoid crossing of other modes with a 2–3% tuning range. A suitable value is $l = 2.463$ cm ($2a/l = 1.15$) where the neighboring TE212 and TM111 modes are several percent away. These dimensions are adequate compared to the stopping distribution of the 100 MeV/c $\overline{\rm p}$ beam of the AD in low-temperature helium gas of ~ 0.5 bar and ≤ 10 K, which is typically 1 cm^3. The upper right of Fig. 10 shows the field distribution in the TM110 mode, together with the $\overline{\rm p}$ stopping distribution (dashed circle). Since the mode pattern has no rotational symmetry, there are two degenerate polarizations, *i.e.* the one shown and another one where the pattern is rotated by 90 degrees. For our case, only the magnitude of the magnetic field but not its direction is of importance, so that this degeneracy can be ignored.

If later for systematic studies different transitions will be measured, a new cavity with different diameter has to be constructed for each case. By chosing a waveguide which covers the whole frequency region of interest (e.g. WR 75, range 10–15 GHz) and using a broad-band TWTA amplifier and synthesizer, all other parts except the cavity can be used if the cavity is attached to the waveguide by a flange as shown in Fig. 10.

The dependence of the magnetic field on the Q value can be obtained according to Eq. 14 by integrating the solutions of the Maxwell equations for the cylindrical geometry. For the TM110 mode we obtain for the maximum field value on the axis of the cavity

$$H_r(r=0) = \frac{\sqrt{2P_l}}{a|J_1'(x_{11})|\sqrt{\mu_0 \pi l \omega}} \times \sqrt{Q} \tag{16}$$

with P_l = energy losses in the walls of the cavity, $\omega = 2\pi\nu$, $J_1'(x_{11}) = -0.40276$, and $\mu_o = 4\pi \times 10^{-7}$ Vs/(Am). Substituting the known parameters we obtain for the magnetic flux density B in units of Gauss:

$$B_r^{\rm TM110}(\nu{=}12.91 \text{ GHz}) = \mu_0 H_r^{\rm TM110}(\nu{=}12.91 \text{ GHz}) = 3.508 \times 10^{-2}\sqrt{P\,[\mathrm{W}]\,Q} \quad [\text{Gauss}], \tag{17}$$

where P[W] denotes the power dissipated in the cavity in Watts.

Assuming a reasonable value of $Q \sim 30$, a peak power of $P \sim 240$ W inside the cavity is needed to generate of field of $B = 3$ Gauss. Taking into account losses due to reflections of the microwaves at various transitions and at the coupling to the cavity, a commercially available TWTA amplifier with 2.5 kW *average (rms)* output power is a safe solution as a generator of the microwaves. The microwaves have to be applied only during the measurement period of ~ 1 μs. There is therefore no problem of heat load into the low-temperature cavity, but the field strength at this high power makes it necessary to use a waveguide rather than a coaxial cable to feed the microwaves into the cavity.

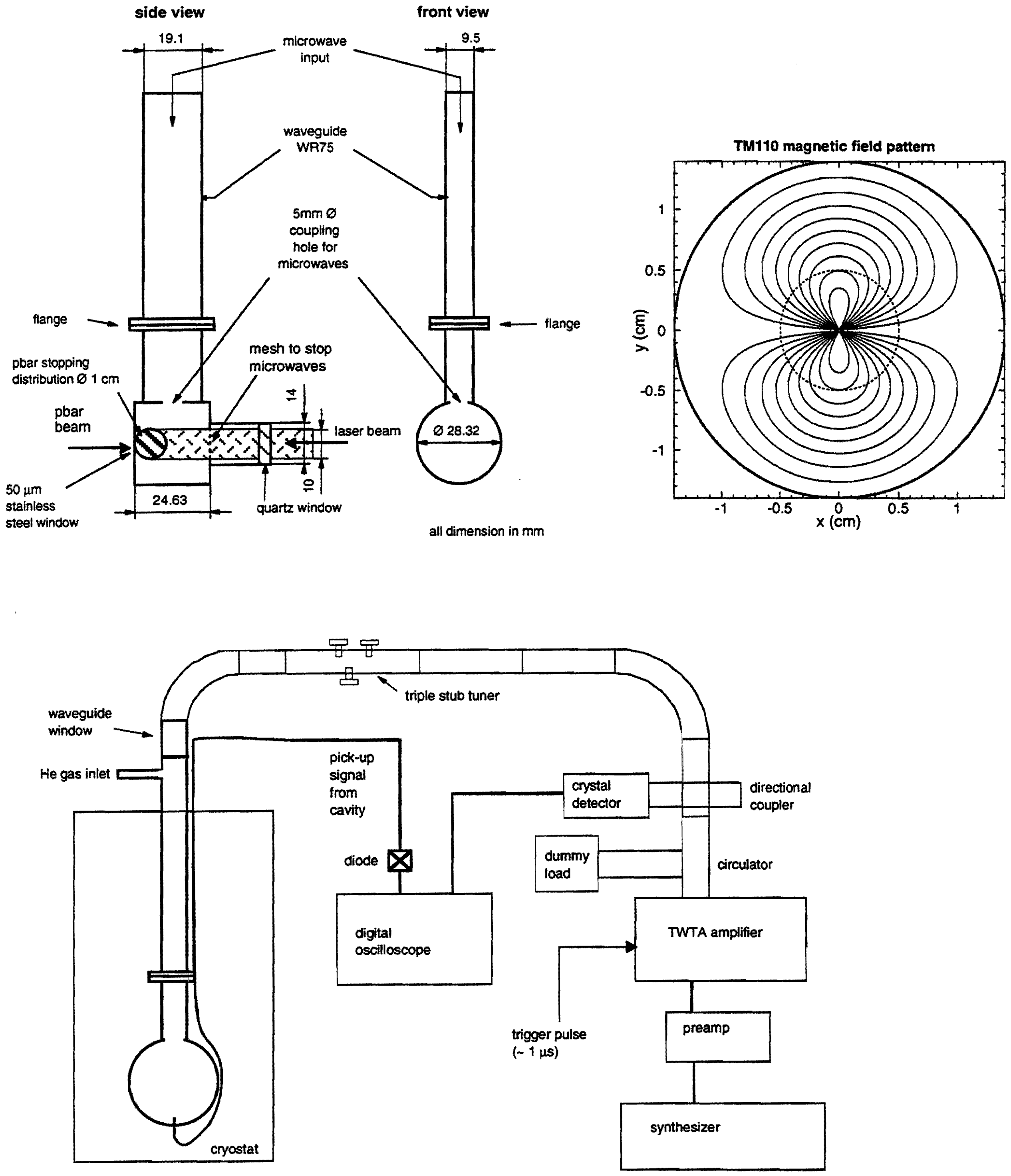

Figure 10: *Upper left: side and front view of the microwave cavity and the waveguide as described in the text. The antiproton stopping region and the laser path are also shown. Upper right: mode pattern of the TM110 mode and* $\bar{p}$ *stopping distribution (dashed circle). Lower: Schematic setup of the microwave generation and detection system. The part of the waveguide which is connected to the cavity and which is filled with He gas is separated from the outer waveguide by a window (quartz plate). The triple stub tuner is used to change the Q-value, and the circulator makes sure that the TWTA amplifier always sees the same load, independent of the Q-value.*

2.7 List of experimental equipment

All the experiments described in the previous sections will be performed with a common setup which is shown in Fig. 11, with only the target cryostat being exchanged. Table 6 lists the equipment needed.

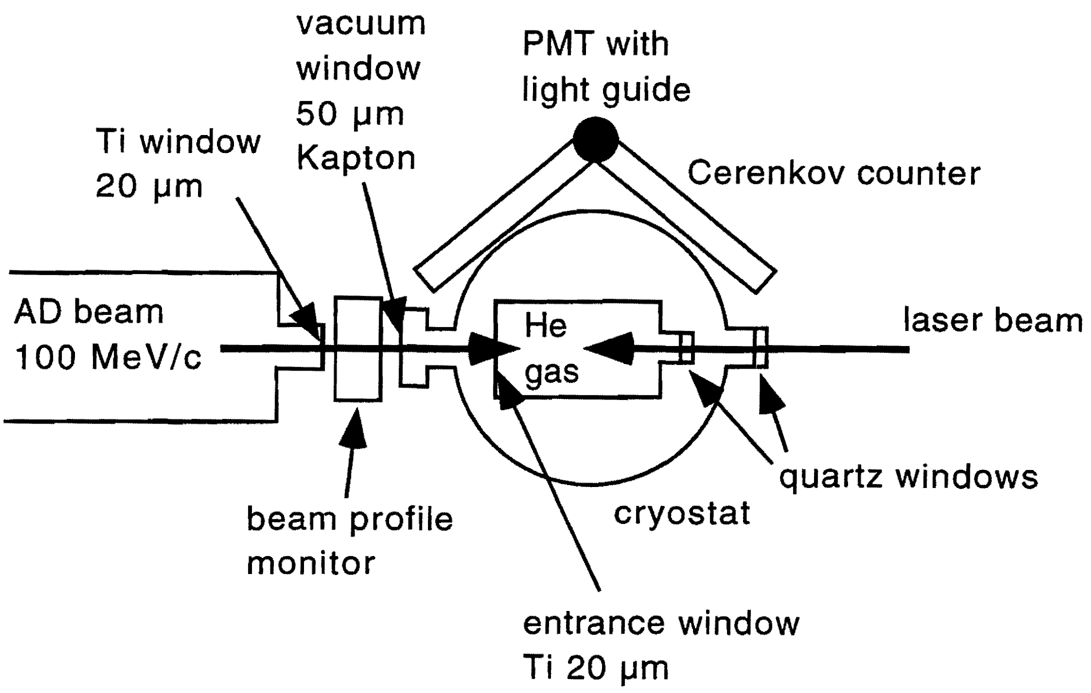

Figure 11: *Schematic setup of the* $\bar{p}$*He*$^+$ *experiments.*

Equipment	Comment	Delivered by
laser system	2 sets	Tokyo/Okazaki
Čerenkov counter		Tokyo
fast gating PMT	Hamamatsu Photonics	Tokyo
beam profile monitor		Tokyo
cryostats	1 multi-purpose 1 for microwave experiment	Tokyo Tokyo
gas supply and mixing system	incl. turbomolecular pump	Tokyo
electronics	CAMAC for beam profile monitor fast sampling digital oscilloscope	Tokyo Tokyo
microwave system	synthesizer, TWTA, etc.	Tokyo

Table 6: *Equipment needed for the first-year experiments*

2.8 Estimation of measurement time

The following table estimates the time required to perform the experiments described in the previous sections. The criterion used was to require the same number of $\bar{p}$ per data point as in previous slow-extraction runs, assuming a rate of 10^7 $\bar{p}$/shot from the AD. One data point corresponds to the measurement of one ADATS, i.e. the laser resonance intensity at one set of conditions (e.g. laser wavelength, target condition, microwave frequency).

Section	Experiment	Quantity measured	AD shots per point	AD shots per measurement
2.1	higher resolution of resonance energies	center of resonance line	5	100
2.2	shift and width	center, width of line	10	200
2.3	quenching by H_2 etc.	quenching cross section	5	400
2.4	search for other resonances	ADATS	1	100
2.4	lifetime, population determination	resonance intensity	5	5–50
2.5	HFS measurement	resonance intensity	10	40

Table 7: *Estimated time required for the different experiments.*

Since resonance scans do require very stable experimental conditions in terms of $\bar{p}$ beam position and laser power, it is definitely required to finish one series of measurements within the daily 12 hour beam period of the AD. Therefore and to guarantee the best possible stability of the beam position we cannot share the AD beam with other users during most of the experiments involving laser spectroscopy of antiprotonic helium atomcules. Of course, this will be discussed and agreed upon with the AD Users' Committee.

3 Experiments with antiproton beams from the RFQ

Next step: toward lower energy

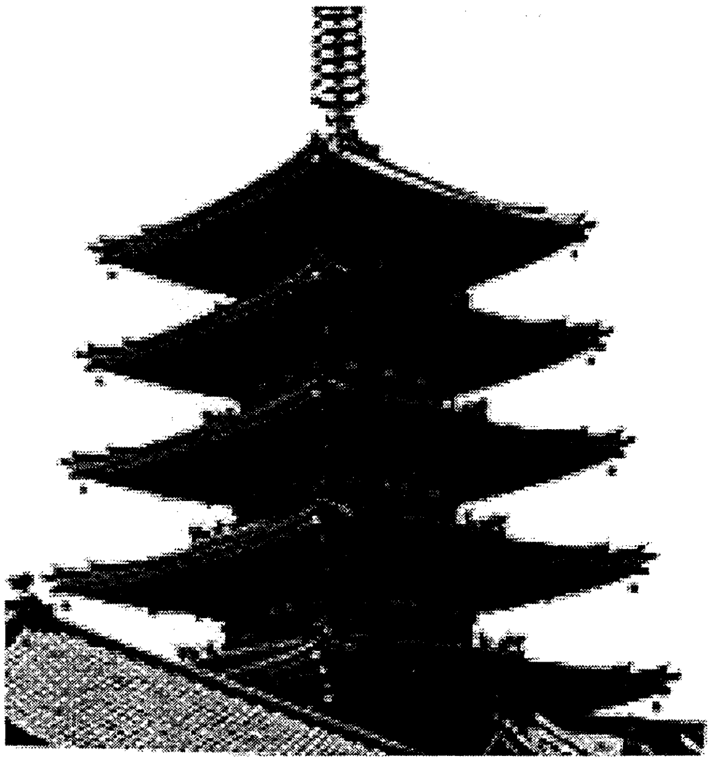

Tower of Sensoji Temple, Asakusa, Tokyo

3.1 $\bar{p}He^+$ atomcule studies using the $\sim$ 100 keV beam from the RFQ

3.1.1 Motivation

Experimental data on the capture process of the antiproton by the helium atom are scarce. The capture cross-sections have never been measured; only little experimental information on the initial population distribution $P(n,l)$ at $\bar{p}He^+$ formation is available, also there are some theoretical studies [13, 30, 43].

In previous work done at LEAR, we measured the populations of several states in the $n \sim \sqrt{M^*/m_e}$ region where initial capture is believed to occur. However, these experiments were done only for atoms formed in dense helium targets of $\rho > 10^{20}$ cm^{-3}, because of the high energy ($E = 5.8$–20 MeV) of the antiproton beam. Atoms formed in such high-density media are subject to collisions with helium atoms, which were found to affect the lifetime of some $\bar{p}He^+$ states [25]. Also the majority of the metastable atoms were initially populated only in the energetically lower-lying states $n \leq 40$ [15, 16].

Recent calculations of the population distribution of $\bar{p}He^+$ atoms at formation indicate that 20% of all incoming antiprotons should be captured into the metastable states[43]. However, experiments using cryogenic helium targets at $\sim$ 1 bar show that only 3% of the antiprotons actually become long-lived. One of the explanations for this discrepancy is due to collisional Stark processes with surrounding helium atoms that quench the higher-lying metastable states during the thermalization of the $\bar{p}He^+$ atom. This theory claims that the states with $n \leq 40$ are stable against collisional quenching at all densities up to liquid helium, whereas states with $n > 42$ are fully destroyed within nanoseconds, and only become metastable at ultra-low densities of $\sim$ 1 Torr. The yield of metastable $\bar{p}He^+$ atoms should therefore increase sharply as the density nears 1 Torr, and also the mean lifetime of the atom may increase to > 8 μs.

We propose to carry out laser spectroscopic studies of metastable $\bar{p}He^+$ atoms formed in helium gas targets at ultra-low densities of $\rho \sim 10^{18}$ cm^{-3}, corresponding to a target pressure of $\sim$ 1 Torr and a temperature of 5 K. At such conditions, collisional effects with external helium atoms will decrease, so that the lifetimes and initial population distributions of the atom at the zero-density limit can be more directly observed.

3.1.2 Experimental setup

An RFQ linear decelerator will be constructed to decelerate the pulsed antiproton beam extracted from the AD from 5.8 MeV to $\sim$ 100 keV. Preliminary simulations of the characteristics of the beam indicate that the energy spread would be ± 5 keV, with a pulse width of 200 ns, a diameter of 5 mm, and an emittance of 180 π mm·mrad. The design acceptance of the RFQ is such that about half of the total beam can be decelerated to 100 keV; the remaining half is ejected at 5.8 MeV. A XY beam profile monitor will be prepared at the end of the RFQ beam line to aid the steering and focusing of the 100 keV beam.

A schematic drawing of the apparatus is given in Fig. 12. The antiproton beam will be injected into a cryogenic gas target at a pressure of 1 Torr and a temperature of 5 K, through a series of two 0.4 μm formvar foil windows [65] which decreases the rate of helium leakage through the beam window. Before entering the window, the beam passes through a 0.3–0.5 μm carbon degrader foil, which is used to adjust the size of the stopping distribution of antiprotons in the target gas. A high-capacity turbomolecular pump will improve the vacuum at the exit of the RFQ to $< 10^{-6}$ Torr, which is the maximum pressure allowed for the operation of the RFQ.

Monte-Carlo energy-loss simulations indicate that the antiproton beam will stop within a 4–6 cm spherical region in the helium gas target. These simulations use experimental data on the stopping power of antiprotons at energies of 1–100 keV in helium gas and in thin films, which were measured by the Obelix [63] and PS194 [59] experiments at LEAR. The effects of range straggling and multiple scattering according to the Vavilov and Moriele distributions, respectively, have also been taken into account.

The lifetime of the metastable antiprotonic helium atoms thus formed will be measured using the same method as in the experiments using the 5.8 MeV beam. A Cherenkov counter equipped with a gatable photomultiplier will be used to detect the analog signal from decaying $\bar{p}He^+$ atoms. A laser beam pulse will be fired into the target chamber through a quartz window, to irradiate the $\bar{p}He^+$ atoms and create a sharp annihilation spike on this analog delayed annihilation time spectrum.

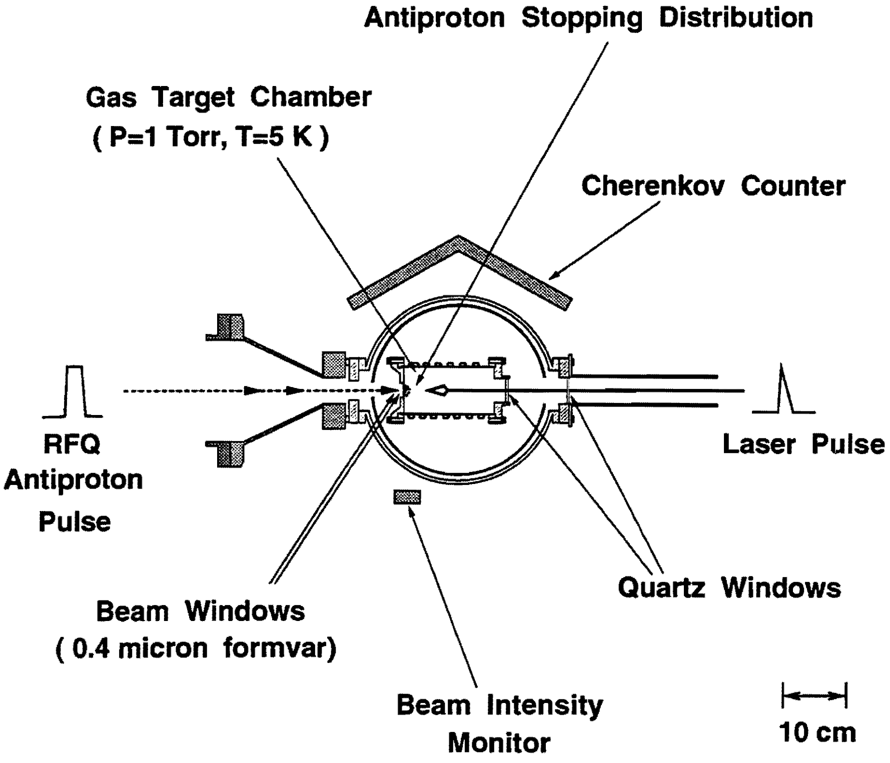

Figure 12: *A schematic drawing of the apparatus for the laser spectroscopy experiment of* $\bar{p}He^+$ *atomcules using the* $\sim$ *100 keV beam from the RFQ.*

3.1.3 Experiment

First, the stopping distribution of antiprotons in the helium gas will be adjusted by tuning the laser beam pulse to a known resonance transition, and then changing the thickness of the degrader material until the intensity of the laser resonance spike is maximized.

The overall lifetime of $\bar{p}He^+$ atoms at various target densities between 1–10 Torr will be systematically studied by measuring the decay rate of the delayed annihilation time spectrum. Laser spectroscopy will then be used to measure the lifetimes of the individual cascade sequences $v = 0, 1, 2, 3$ which will indicate whether the higher-lying states at $n > 40$ are populated at such low densities. Searches will be made of the resonance transitions in the higher-lying $n \geq 40$ region, such as $(n,l) = (40,l) \rightarrow (39,l-1)$ at a wavelength of 670–680 nm which were undetected in previous attempts using higher density targets of 100–1000 Torr and 5.5 K, as well as surveys of the unexplored region $(n,l) = (41,l) \rightarrow (40,l-1)$ at ~ 700–800 nm, and $(n,l) = (42,l) \rightarrow (41,l-1)$ at 900–1000 nm.

The dependence of the lifetimes and initial populations of these states to the density of the helium gas target will be systematically studied for the target conditions between pressures of 1–10 Torr and temperatures of 5–10 K. Measurements of the initial populations will yield information about the state quenching effects during thermalization of the $\bar{p}He^+$ atom. The studies on the lifetimes will provide the cross-section of individual states during collisions with ordinary helium atoms after thermalization of the $\bar{p}He^+$ atom; this in turn will help us learn more about the anomalous metastability of the atom at high densities.

3.2 Atomic collisions

With the antiproton beam from the AD decelerated in the RFQ, it becomes possible to perform atomic collision experiments with 10–100 keV antiprotons, and hence to approach a projectile velocity regime where the collisions are "slow" and quasi-adiabatic. This opens up powerful new opportunities for the study of such collisions with heavy negative particles. The restriction to be remembered is that the beam arrives as a pulse every minute with the pulse width of ~200ns.

3.2.1 Energy loss in thin films and gases

The energy loss per pathlength (the stopping power) of fast (30 keV–3 MeV) antiprotons in a number of solid targets has been measured by the PS194 collaboration ([59] and references therein). An example of these data is shown in Figure 13.

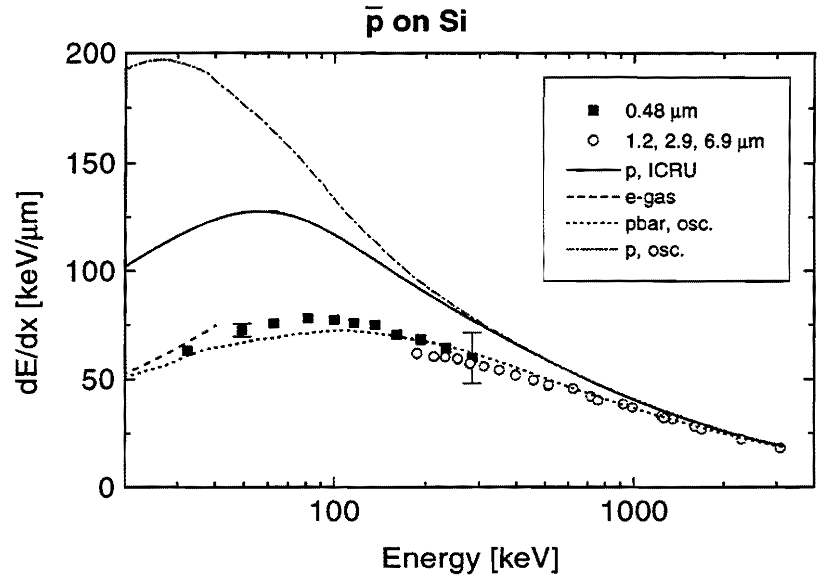

Figure 13: *Stopping power of antiprotons in Si*

Here it can be seen that the experimental data agree rather well with the available theoretical calculations (see Ref. [59]). It is interesting to note, however, that there is no such agreement between the experimental data for proton impact (solid curve) and theory. The reason is that the theories are not able to account for electron capture and loss, which leads to an ill-defined charge state of the projectile as it passes through the target. This is one more example of the usefulness of antiproton data in consolidating the theoretical efforts in the field of atomic collisions.

For low projectile energies (less than around 25 keV) it is predicted that the stopping power should be proportional to the projectile velocity, and an advanced theoretical calculation based on the so-called electron-gas model has been published (Ref. [62]). The result of this theory for a Silicon target is shown in Figure 13 as the curve marked "e-gas".

With the antiproton beam extracted from the RFQ, it should be possible for the first time to test this theory in its region of validity.

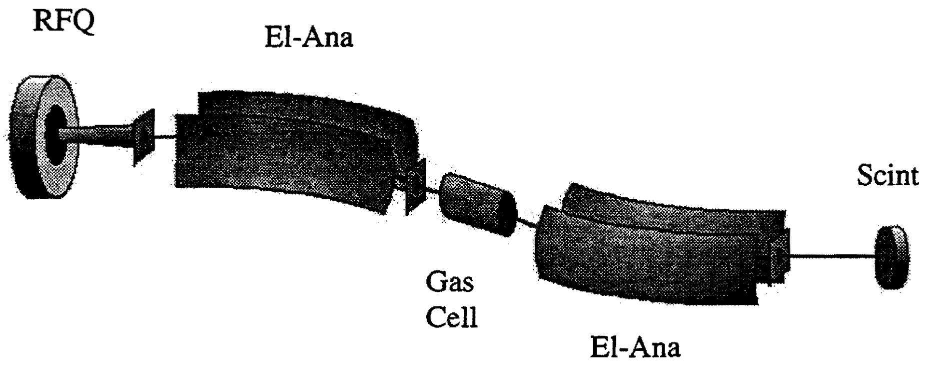

Figure 14: *Schematic drawing of the apparatus for the dE/dx measurement.*

The apparatus suggested for the dE/dx measurements is shown schematically in Figure 14. In the case of energy loss measurements, it is necessary to have a high energy resolution, in order to measure accurately for example a 10% energy loss. This will reduce the transmission of the antiprotons. For example, if the electrostatic analyzer has a 1% resolution, we shall have a transmission of 4×10^{-4} at 50 keV antiproton energy and 2×10^{-5} at 10 keV. Since each detected projectile gives information on the mean energy loss, this reduction is not a severe problem. It is our plan to use a 0.15 μm Si foil target. However, as indicated in the drawing, it is also possible to use a differentially pumped gas cell. In that case, we should be able to measure the energy loss per path length in for example helium gas down to an antiproton energy of 1 keV. There exist measurements of this quantity down to 1 keV by the Obelix collaboration [63], but these data are indirectly obtained via an arbitrary fitting function, and rather uncertain.

3.2.2 Channeling of slow antiprotons

Channeling phenomena of ions and electrons have been extensively studied. The channeling trajectory of a negatively charged particle is attracted to an atomic string or atomic plane whereas that of a positively charged particle is pushed away from it. This situation results in an increase in close collision probabilities for negatively charged channeled particles. In PS194 using LEAR, channeling of antiprotons have been investigated at beam energies as low as 1.4 MeV. While the motion of ions and electrons with relativistic energies can be described by classical mechanics, that of low energy (10–100 keV) electrons requires a quantum treatment. In this sense, channeling of low energy antiprotons forms a new domain of channeling with slow, negatively charged, heavy particles.

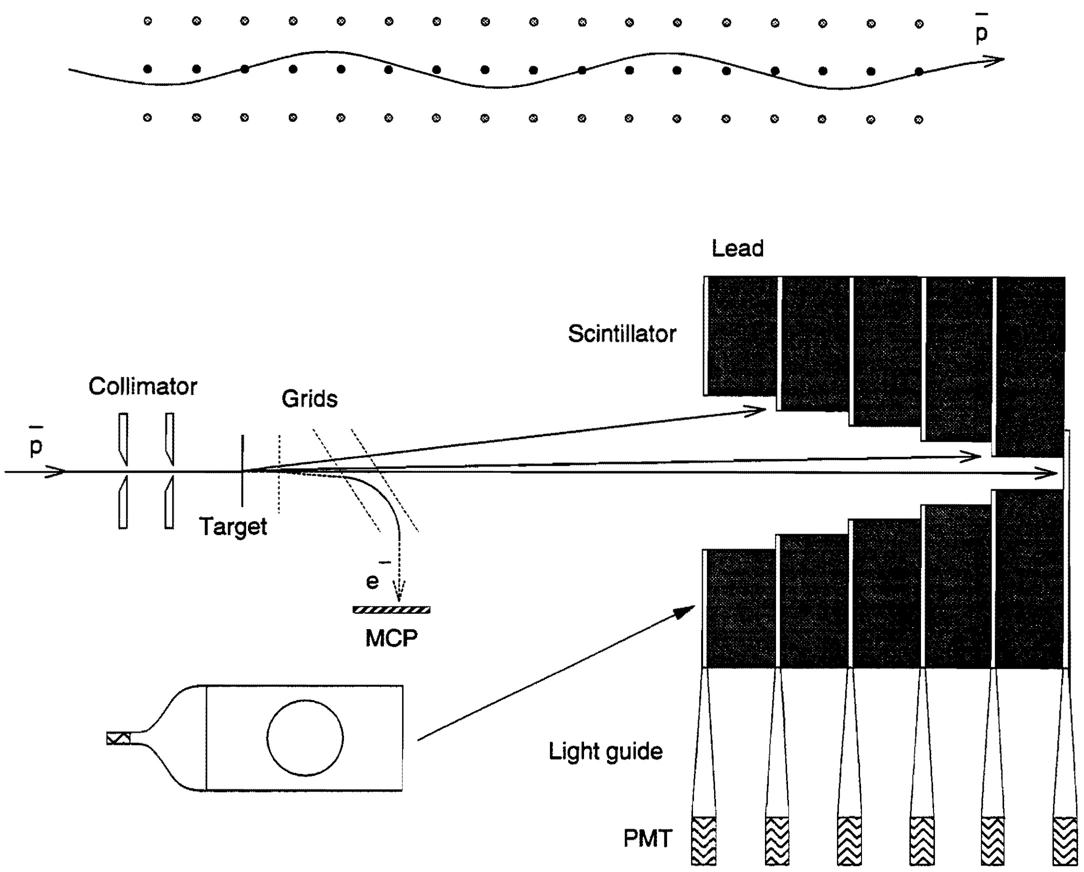

Figure 15: *Channeling of slow antiprotons*

Figure 15 shows the apparatus to be used for channeling studies with the AD RFQ. A beam of 10–100 keV antiprotons will be collimated by a pair of apertures with a diameter of 1 mm and a distance of 1 m. A self-supported thin (~ 100 nm) single crystal will be mounted on a goniometer. After passing through the crystal, the exit angle of individual transmitted antiproton will be measured with a position sensitive detector placed 2 m downstream the crystal. A time-of-flight measurement will provide the energy loss of each $\bar{p}$ at the same time. The correlation between the exit angle and the energy loss will give information on position dependent stopping powers. For positively charged particles, the characteristic angles for axial channeling in the high and low energy regions are $\Psi_1 = \sqrt{2Z_1Z_2e^2/dE}$ and $\Psi_2 = \sqrt{a_{TF}\Psi_1/d}$, respectively. The boundary between high and low energies is $E' = 2Z_1Z_2e^2d/a_{TF}^2$, the value of which for protons travelling along the Si <110> axis is 40 keV. A transition between these two energy regions can be investigated, especially, in comparison with that for protons.

3.2.3 Swarm experiments of slow $\bar{p}$

Although the very beginning of antiprotonic atom ($\bar{p}A^+$) formation processes in rather dense media is of great interest, little is known except for the case of $\bar{p}He^+$. In order to establish a comprehensive picture of the very beginning not only of $\bar{p}He^+$ but also of other kinds of $\bar{p}A^+$, which have been very difficult to study because of their immediate annihilations after $\bar{p}$ injection, we propose here to apply a swarm technique.

The swarm technique is a powerful tool to investigate low-energy ion-atom collisions, where a drift velocity of a charged particle in a rather dense medium is measured to evaluate rate constants, scattering cross sections, etc. [64]. A short introduction of the swarm technique is given in Appendix B.

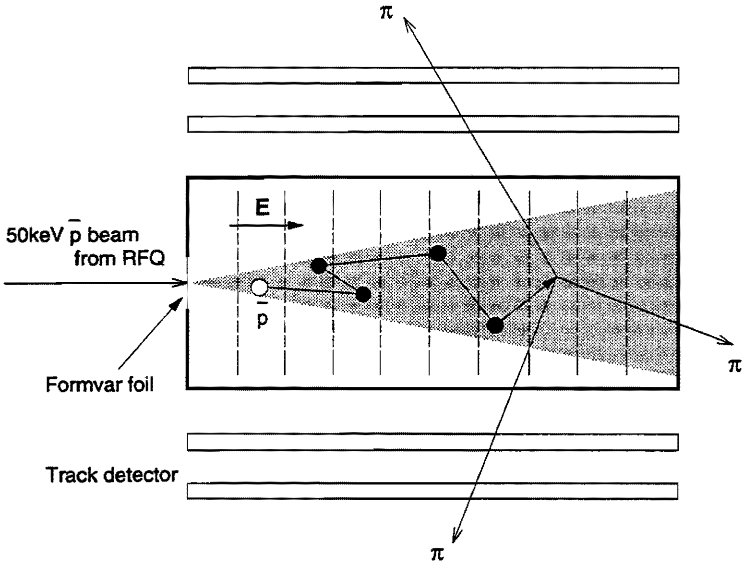

Figure 16: *A schematic drawing of the apparatus for a swarm-type experiment.*

A schematic drawing of the proposed experimental setup is shown in Figure 16. An antiproton beam of ~ 50 keV from the RFQ is injected in a gas cell of 10 cmϕ × 100 cm filled with a target gas of ~10 Torr with several grids to apply a position dependent electric field, $E(z)$. The gas cell is vacuum-shielded from the RFQ beam line by a formvar foil of ~ 3000Å [65], which serves also as an energy degrader of the $\bar{p}$ beam from the RFQ. The degraded $\bar{p}$ is stopped within several cm from the entrance foil through multiple collisions with target atoms (molecules), and is eventually captured by an atom forming an antiprotonic atom.

As is seen in Fig. 23 for $\bar{p}p$ formation, a well-defined threshold is expected for efficient $\bar{p}A^+$ formation. When $E(z)$ is arranged so that it gradually decreases along the trajectory, the drift energy of $\bar{p}$, $\epsilon_d(z)$, also decreases in proportion to $E(z)^2$ (see Eq. 23). At the position z where $\epsilon_d(z)$ is higher than the threshold, the $\bar{p}$ survives annihilation and keeps moving. When the $\bar{p}$ reaches a region where $\epsilon_d(z)$ gets comparable to or lower than the threshold energy, the $\bar{p}A^+$ formation probability is enhanced drastically, which increases the annihilation rates of $\bar{p}$. The annihilation signals are monitored by a pair of track detectors. Combining the position information obtained by them and the time difference between the $\bar{p}$ injection and the annihilation signal, an effective drift velocity responsible for the $\bar{p}A^+$ formation is evaluated. This technique is expected to provide a universal way to determine the threshold behavior of $\bar{p}$ in any gaseous targets. In the case of Ar target for example, Eq. 24 tells that the threshold electric field is expected to appear at around 1kV/cm.

3.3 List of experimental equipment

The equipment required for the experiments using the RFQ described in this chapter are listed in Table 8. Much of the equipment required for the $\bar{p}He^+$ laser spectroscopy experiment will be carried over from the layout described in section 2.7 which will be used in the first year. The annular antiproton detector for the atomic collision experiments is already constructed, and has been successfully used in previous experiments at LEAR by the PS194 collaboration.

Equipment	Comment	Delivered by
laser system	2 sets	Tokyo/Okazaki
Cerenkov counter		Tokyo
fast gating PMT	Hamamatsu Photonics	Tokyo
beam profile monitor	at target focus	Tokyo
target	for $\bar{p}He^+$ spectroscopy	Tokyo
gas supply and mixing system	incl. turbomolecular pump	Tokyo
electronics	CAMAC for beam profile monitor fast sampling digital oscilloscope	Tokyo Tokyo
electrostatic energy analyser	2 sets	Aarhus
collision chamber and goniometer		Tokyo
annular $\bar{p}$ detector		GSI
drift chamber		Tokyo
track detector system		Tokyo

Table 8: *Equipment needed for the experiments using the RFQ*

3.4 Estimation of measurement time

The unit machine time required to complete each experiment described in this chapter is estimated in Table 9. The $\bar{p}He^+$ laser spectroscopy experiment described in Section 3.1 requires about 100 AD shots to complete one scan over the resonance transition. The stopping power, channeling and swarm experiments require about 50–100 shots to obtain a data point.

As with the situation described in Section 2.8, some of the experiments, especially the $\bar{p}He^+$ atomcule and stopping power measurements, require stable experimental conditions over a large number of AD shots, which can only be obtained if we are the only user of the AD beam during that time. Other experiments like the channeling and swarm measurements can be performed while sharing the AD beam with other experimental areas. Those points will be discussed and agreed upon with the AD Users' Committee.

Section	Experiment	Setup	AD shots per measurement
3.1	$\bar{p}He^+$ atomcules	Fig. 12	100
3.2.1	stopping power	Fig. 14	100
3.2.2	channeling	Fig. 15	100
3.2.3	swarm	Fig. 16	50

Table 9: *Estimated time required for each experiment using the RFQ.*

4 Experiments with antiprotons in and from the trap

3rd Step: An entirely new era of low energy antiproton atomic physics

Sanja festival - when downtowners relax in a traditional costume, YUKATA

4.1 Collision dynamics of an ultra slow $\bar{p}$ beam with atoms and molecules

4.1.1 Total ionization

For impact of positive, low velocity projectiles, (i.e. projectiles with velocities smaller than those typical for the electrons of the target atoms), the calculation of ionization cross sections is complicated by the charge exchange phenomenon, where target electrons are transferred to the projectile. This complication does not exist for antiproton projectiles, and therefore low velocity antiproton impact ionization is a very clean case for tests of low velocity ionization theories, and hence of low velocity atomic collision theory in general.

The simplest possible case is that where an antiproton ionizes *atomic* hydrogen, since there is only one electron in play. Data for this process were published by PS194 in 1995 [66], and have caused considerable theoretical efforts since. The experimental data are compared with theoretical calculations in Fig. 17.

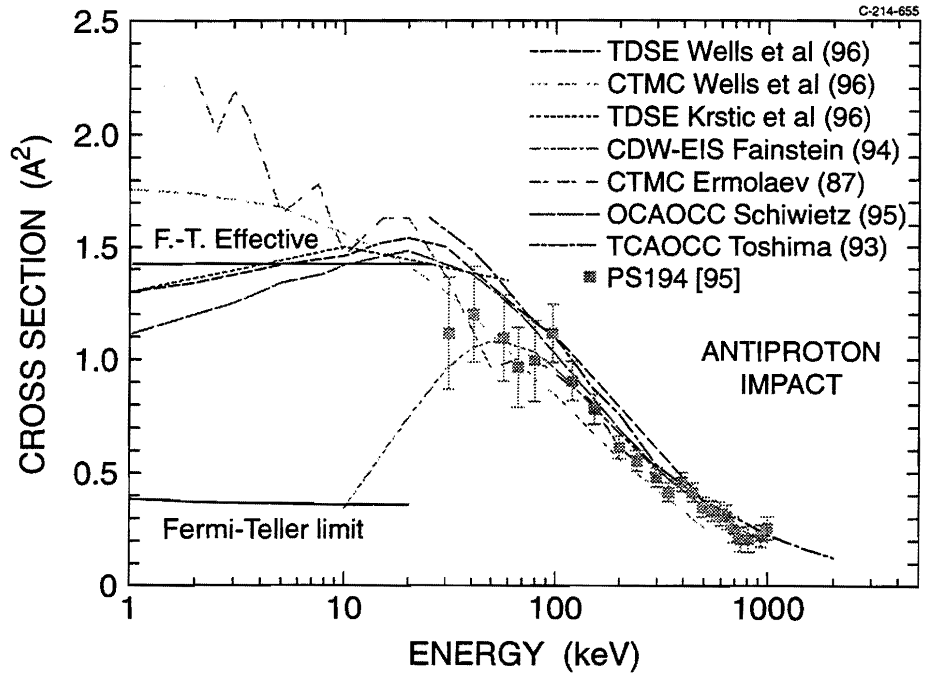

Figure 17: *Ionization of atomic deuterium with antiprotons [55]*

As can be seen, all theories agree with the PS194 experimental data. However, there is a considerable disagreement between the various theories in the region where no experimental data exist.

If the projectile velocity is very low compared with the atomic electron's velocity, a quasi-molecular calculation shows that the electron becomes unbound when the antiproton reaches a point at a distant 0.63 a.u. from the hydrogen nucleus [67]. This so-called Fermi-Teller distance defines a lower bound on the ionization cross section. At higher speeds, the adiabatic picture used to calculate the critical distance of approach breaks down, and the electron is released at larger distances. In the figure,the value marked "F.-T. Effective" shows the resulting ionization cross section. This simple model is supported by recently published very advanced calculations such as the direct integration of the time dependent Schrödinger equation (TDSE) (Krstic et al. [68] and Wells et al. [69]) and the close coupling OCAOCC calculations (Schiewietz [70]). Clearly, however, there is so much divergence between the published theories that it is absolutely necessary to perform a few measurements of this fundamental cross section in the projectile energy range between 1 and 10 keV.

When the He atom is the target, the situation is complicated by the fact that there are two target electrons in play. Fig. 18 shows the experimental results of PS194 compared with (very) recent theoretical calculations.

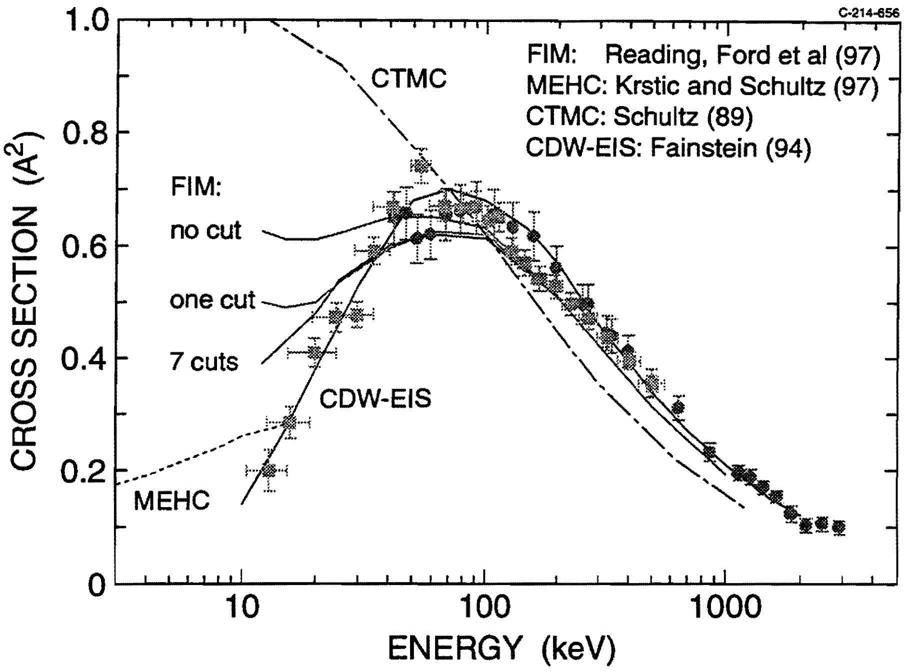

Figure 18: *Ionization of He with antiprotons [55]*

As can be seen, and contrary to what is expected for the atomic hydrogen target, the single ionization cross section of He decreases considerably with decreasing projectile velocity below the cross section maximum. The reason is most likely that although enough energy may be given to one of the electrons to ionize it, the interaction of that electron with the other target electron distributes the available energy, which subsequently is radiated away. The importance of the electron-electron interaction can be seen by inspection of the 3 curves labeled FIM: The curve marked "no cut" is a Forced Impulse Method result without electron-electron dynamic correlation. "one cut" and "7 cuts" marks results with increasing amounts of correlation involved [71]. The curve marked MEHC is a Multi Electron Hidden Crossing calculation by Krstic and Schultz [72] which takes into account the full e–e interaction, but which might not be valid at impact energies as high as 10 keV. (The CDW-EIS theory is valid only at high velocities, and it seems to be a pure coincidence that it fits the experimental data so well). It should be noted that there seems to be a discrepancy between the theoretical predictions and the experimental data, and that experimental measurements below 10 keV are needed.

In the above discussion, we have not mentioned many other possibilities for investigations of atomic collisions involving slow antiprotons, such as measurements of double and multiple ionization cross sections and fragmentation of small molecules.

The experimental apparatus around the target which we suggest to apply for the ionization experiments consists of a differentially pumped transport beamline followed by a vacuum chamber containing a recoil-ion time-of-flight (TOF) spectrometer (⟨1⟩ in Fig. 19) much like the one used by the PS194 collaboration (Ref. [66]). The antiprotons are extracted from the Penning trap as a DC beam of energy between 1 and 10 keV. They pass through the target cell where they cross an atomic beam target of H or He, and are then detected by a thin scintillator downstream. The ions created in the target gas are extracted onto an ion detector by a transverse electric DC field, and the ion time-of-flight is determined from the time difference between the two detector signals. The TOF gives the ion mass-to-charge ratio. The ion yield can be converted to a cross section via an independent determination of the calibration constant using a MeV proton beam from the Aarhus university EN Tandem accelerator.

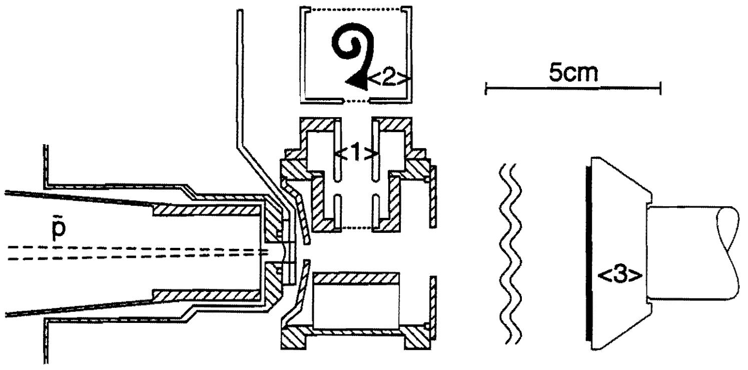

Figure 19: *The target arrangement for measurements of ionization cross section. ⟨1⟩: recoil ion flight tube; ⟨2⟩: ion detector; ⟨3⟩: antiproton detector [66]*

4.1.2 Differential Ionization: kinematically complete experiments

Ionization of atoms and small molecules by antiprotons with energies ranging from 13 keV to a few MeV have been explored in great detail by the PS194 collaboration measuring total single and multiple ionization cross sections at LEAR. Interest has been concentrated on the two most fundamental situations: First, single ionization of atomic hydrogen [66] where only one electron is involved has been studied. Second, single and double ionization of helium where the electron-electron correlation was demonstrated to play an important role for the magnitude of total cross sections [57]. For both situations the energy dependence of total cross sections was found to be considerably different from those for proton impact at energies below about 500 keV. Surprisingly, the ratio of double to single ionization cross sections for helium differed for proton and antiproton collisions up to projectile energies as high as 10 MeV.

These benchmark data for atomic collision physics have stimulated considerable theoretical effort where new insight has been achieved at one hand but substantial questions arose on the other side. In general, the theoretical treatment of ionization by antiprotons is less complicated at medium and low energies, since the charge transfer channel, being dominant for proton impact at energies below about 50 keV simply doesn't exist. In this respect it is surprising that various recent theoretical approaches revealed substantial differences in calculated total cross sections for single ionization of atomic hydrogen and helium at energies below about 100 keV [88]. The reasons for these highly dissatisfying discrepancies are unclear up to now, experimental total cross sections are urgently required at these energies and are proposed in Section 4.1.1. Different mechanisms for double ionization of helium by protons and antiprotons have been illuminated by elaborate calculations with the *Forced Impulse Method* (FIM) which is in good agreement with the experimental ratio of double to single ionization cross sections. The electron-electron correlation in the ground state as well as during the collision was found to be of great importance for double as well as for single ionization.

Up to now only one pioneering run on differential ionization cross sections in collisions with antiprotons has been performed at LEAR by the PS194 collaboration. Due to the limited antiproton flux efficient spectrometers with large detection solid angles are demanded which have only been developed during the last three years. In Fig. 20, the experimental longitudinal momentum distribution (along the beam axis) is shown for 1 MeV antiproton impact. The results have been compared to calculations in the *Classical Trajectory Monte Carlo* method (CTMC) as well as with *Continuum Distorted Wave* (CDW) calculations which both disagree substantially at an impact energy, where total cross sections are well described.

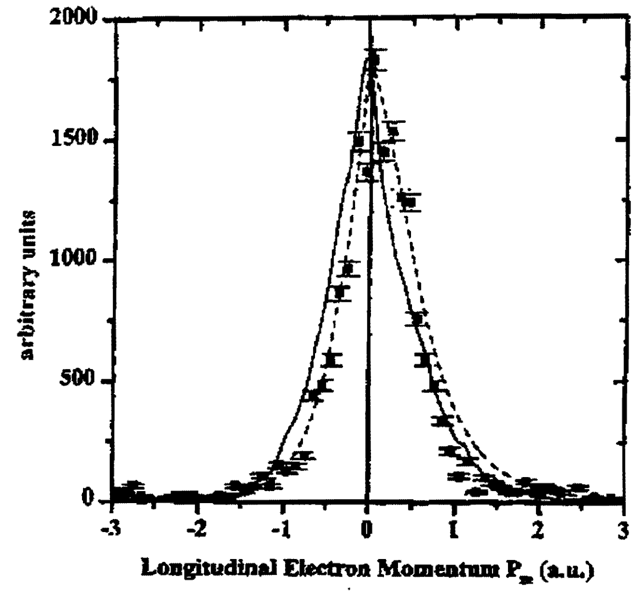

Figure 20: *Experimental longitudinal momentum distributions of electrons for single ionization of helium in collisions with 1 MeV antiprotons. Theoretical results: CTMC (full line), CDW (dashed line).*

To the best of our knowledge, the most elaborate theoretical approaches at low energies as very large scale numerical solutions of the time-dependent Schrödinger equation (TDSE) [88] or the hidden crossing method (HC) [89] both have substantial difficulties to calculate differential electron emission cross sections and no such results have been published up to now.

None of the quantum mechanical theoretical approaches at hand is able to incorporate the full three body dynamics between the ionized electron, the recoiling target ion and the scattered projectile which is only feasible within the CTMC method. Rich structures have been predicted recently in the electron emission for 100 keV antiproton impact [90]. In Fig. 21, the final electron momenta are projected onto a plane defined by the incoming projectile along the +z-axis and the recoiling target He^+ ions along the +x-axis. Crosses denote the location of the target at (px, pz) = (0,0) and the location of the emerging projectile at (px, pz) = (0,2), respectively. Tremendous differences are observed in the three-body dynamics for proton (left column) or antiproton (right column) impact. No such predictions for double ionization have been published until now. It seems to be difficult, if not impossible, to obtain differential information from the FIM calculations where the continuum is described by pseudo-states to represent the continuum energy of the electrons but not their individual momenta.

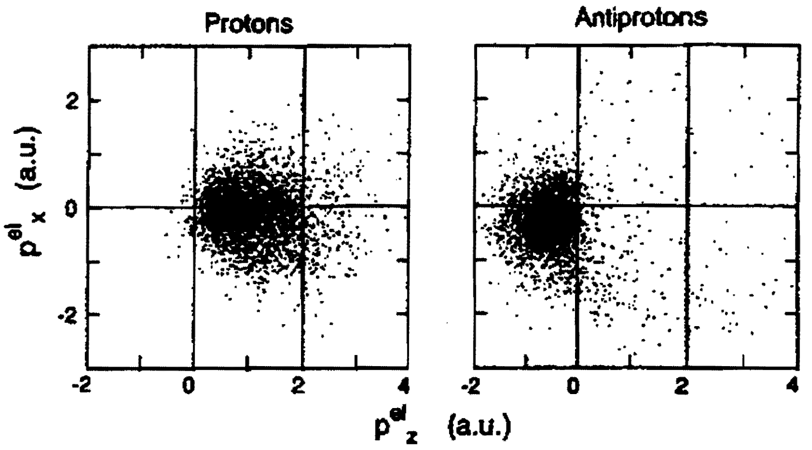

Figure 21: *Ionized electron momenta projected onto the plane determined by the incident projectile (along the +z direction) and the outgoing recoil ion (along the +x axis) in coincidence with the transverse momentum of the recoil ion ($p_{R\perp} \leq 1.0$ a.u.). The proton and antiproton results are in the left- and right-hand part, respectively.*

Here we propose to perform kinematically complete experiments on single ionization of hydrogen and helium by antiprotons, the most fundamental three particle reactions in atomic physics over broad range of incident energies (5 keV to 500 keV) in order to provide benchmark data for theory. Such experiments have become feasible and have been performed for slow proton on helium collisions at energies between 5 keV and 15 keV [91] as well as for heavy-ion impact [92–94]. In addition, differential experiments on double ionization are anticipated. Recently, we have been demonstrated the feasibility of kinematically complete experiments on helium double ionization for heavy-ion on helium collisions [95]. Such studies provide the key to the understanding of differences in the calculated total cross sections for single ionization of hydrogen and helium by antiprotons. They provide an ultimate test for atomic collision theories and are the experimental basis for a detailed understanding of the role of the dynamic electron-electron correlation in single and double ionization of helium. Moreover, these experiments yield the energy loss of the projectile as well as its angular scattering in single ion-atom collisions and thus are the link to the energy loss and angular straggling of antiprotons traversing thin films or gases (Section 3.2.1). Even more, our apparatus is feasible to analyze the momenta of up to 10 electrons emitted from a foil after the passage of an ion and thus gives unprecedented information on the details of the energy transfer from the ion to the electrons of a solid. As illustrated in Fig. 22, the experiment is based on the simultaneous detection of the recoiling target ion (*Recoil-Ion Momentum Spectroscopy*: RIMS) and of one or several electrons emitted in a single or multiple ionization event. Only a brief description is given here, technical details having been described by Moshammer et al. [96]. An overview on experiments has been provided in a recent review by Ullrich et al. [97].

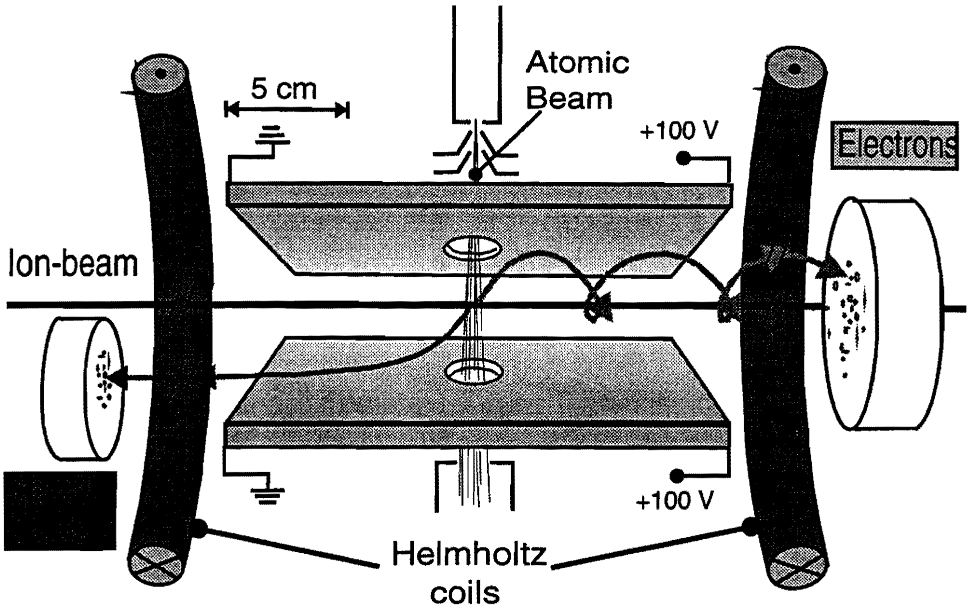

Figure 22: *Schematic of the "GSI-reaction-microscope" (see text)*

A two-stage supersonic jet provides a well defined (2.8 mm diameter), cold (50 mK) and dense (10^{12} atoms/cm^2) atomic or molecular target. Low-energy ions (typical energies $E_R \ll 1$ eV) and electrons (typical energies $E_e < 80$ eV) are accelerated into opposite directions by applying a weak electric field (1–5 V/cm) along the ion-beam. The field is sufficiently strong to project recoiling target ions with a large solid angle ($\Delta\Omega_R/4\pi > 98\%$ for $\mathrm{He}^{1+,2+}$) onto a two-dimensional position sensitive (2DPS) microchannel plate detector (MCP). An additional solenoidal magnetic field is generated by two Helmholtz coils (1.5 m in diameter) with its field vector along the ion beam. It efficiently guides the electrons ($\Delta\Omega_e/4\pi > 50\%$ for the same reactions) onto a 80 mm diameter MCP equipped with a fast delay-line readout that is able to accept "multi-hits" for time intervals between individual hits larger than 10 ns. From the measured absolute positions and flight times the ion and electron trajectories are reconstructed and their initial momenta are calculated. For the investigation of multi-electron emission from foils, the supersonic jet is simply turned off and replaced by solid state targets.

4.1.3 Antiprotonic atom formation

As is described in Appendix C, slow monoenergetic antiproton beams will be prepared by the combination of an RFQ and a catching trap, which enable us, for the first time, to investigate the elementary processes of antiprotonic atom ($\bar{p}A^+$) formation. These exotic atoms are produced in vacuum, and the spectroscopic nature of isolated $\bar{p}A^+$ at the initial stage of their formation is studied. This will be realized employing collisions between ultra slow antiprotons and a thin gas target under single collision conditions, where external electric fields due to neighboring target atoms (molecules) which drastically shorten the lifetimes of exotic atoms via Stark quenching, can be negligibly weak (Appendix B.1). Among various antiprotonic atoms, $\bar{\mathrm{p}}\mathrm{p}$ is particularly interesting because it is the simplest two body system consisting of a particle and an antiparticle with strong interaction. Such a two body system in Yrast states can decay only via slow radiative transitions when an external electric field is negligible, the lifetime of which easily exceeds ~ 1 μs.

Total $\bar{\mathrm{p}}\mathrm{A}^+$ production cross section We propose, at the first stage, (i) to measure the antiproton capture cross sections $\sigma_{\bar{p}A}$ for various gaseous targets such as H, H_2, He, Li, Ne, etc., and (ii) to measure the intrinsic lifetimes of these antiprotonic atoms in vacuum for ultra slow (1–100 eV) antiprotons under single collision conditions. The capture cross sections and the lifetimes of exotic atoms will be measured combining a pulsed antiproton beam and delayed annihilation signals. As is discussed in Appendix B.1, the $n_{\bar{p}A}$ distribution is controllable by varying the incident energy of $\bar{\mathrm{p}}$. The experimental setup is similar to that used for the ionization measurements (Fig. 19) but with a flight tube of ~ 1 m. The momentum of $\bar{\mathrm{p}}\mathrm{A}^+$ is roughly the same as that of the incident antiproton, i.e., the arrival time of the produced $\bar{\mathrm{p}}\mathrm{A}^+$ at the end of the flight tube is delayed as compared with that of *raw* antiprotons. As shown in Fig. 23, a CTMC calculation predicts that $\sigma_{\bar{p}A}$ is $\sim 10^{-16}$ cm^2, i.e., a target gas cell of ~ 10 cm long filled with $\sim 10^{-4}$ Torr atomic hydrogen (H), the yield is evaluated to be ~ 10 $\bar{\mathrm{p}}\mathrm{p}$/sec for incoming 10^4 $\bar{\mathrm{p}}$/sec.

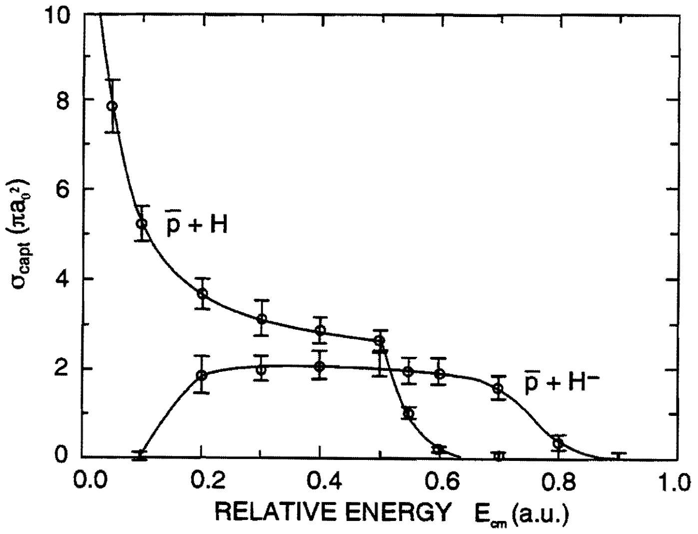

Figure 23: *$\bar{\mathrm{p}}\mathrm{p}$ formation cross section predicted by a CTMC method in $\bar{p}$ + H and $\bar{p}$ + H^- collisions. [84]*

Differential $\bar{\mathrm{p}}\mathrm{A}^+$ production cross section To further investigate the collision dynamics, the principal quantum number distribution will be determined through measurements of ejected electrons. Equation (21) tells that $n_{\bar{p}A}$ of $\bar{\mathrm{p}}\mathrm{A}^+$ is uniquely determined through measurements of the kinetic energy of the released electron, ϵ_{ef}, because ϵ_{ei} and $\epsilon_{\bar{p}}^{\mathrm{cm}}$ are both known.

The experimental setup is similar to that used for the differential ionization studies (Fig. 22) except that plastic scintillators are surrounding the whole setup to detect the annihilation of antiprotons. In the case of $\bar{\mathrm{p}}\mathrm{p}$ for example, the energy difference between adjacent states, $\epsilon_{\bar{p}p}(n_{\bar{p}p} -$

1) $-\ \epsilon_{\overline{p}p}(n_{\overline{p}p})$ [$\sim 2(\mu_{\overline{p}p}/m_e)n_{\overline{p}p}^{-3}\epsilon_R$] is $\sim$ 0.2 eV at $n_{\overline{p}p} \sim 40$, where $\Delta\epsilon_{\overline{p}p} \sim 4$ eV. As a typical time resolution of the system is $\sim$ 1 ns, the adjacent states around $n_{\overline{p}p} \sim 40$ are well resolved by TOF methods. It should be noted that under the presence of the electric field, the $\overline{\mathrm{p}}\mathrm{p}$ annihilates immediately, which gives the start pulse to measure the flight time of the e^- to the MCP.

Multi-electron atoms are also used as targets. The corresponding $\overline{\mathrm{p}}\mathrm{A}^+$ atom formed in a highly excited state decays not only via radiative transitions as in the case of $\overline{\mathrm{p}}\mathrm{p}$ but also via Auger transitions. Considering that Auger transition probabilities are smaller when the overlap between active particles is smaller and the transition energies are larger, antiprotonic alkali atoms are expected to be fairly stable in vacuum. For example, when $\overline{\mathrm{p}}\mathrm{Li}^+$ is produced through $\overline{\mathrm{p}}$ + Li collisions, the antiproton replaces the $2s$ electron, which is far outside of the residual two $1s$ electrons of Li, and accordingly the Auger transition energies are larger and the spatial overlap between the antiproton and the two $1s$ electrons is smaller. It should be noted that the antiproton states with the same principal quantum number but with different orbital angular quantum numbers are not degenerate with each other any more, i.e., $\overline{\mathrm{p}}\mathrm{Li}^+$ is expected to be much stronger than $\overline{\mathrm{p}}\mathrm{p}$ against quenching induced by an external electric field.

As a result of Auger transitions, antiprotonic ions, $\overline{\mathrm{p}}\mathrm{A}^{q+}(q \geq 2)$, are formed. Further, antiprotonic ions could resonantly be formed via *Resonant Transfer and Excitation* [74], which is followed by an Auger electron emission, i.e.,

$$\overline{\mathrm{p}} + \mathrm{A} \rightarrow \overline{\mathrm{p}}\mathrm{A}^{++*} + \mathrm{e}^- \rightarrow \overline{\mathrm{p}}\mathrm{A}^{++} + 2\mathrm{e}^-, \tag{18}$$

where A^{++*} is an electronic excited state of A^+. In this case, resonant features are expected to be seen above the single electron exchange threshold. These multi-electron processes constitute important subjects in the study of slow antiproton-atom collisions as has already been discussed for double ionization of He in Section 4.1.1. Another interesting subject to be pursued is the branching ratio into different charge states.

Collisions with molecular targets In the case of atomic targets, as has been discussed in Section B.1, antiprotonic atoms are formed via an exchange collision between the antiproton and a target electron transferring almost all the initial $\overline{\mathrm{p}}$ momentum to the $\overline{\mathrm{p}}\mathrm{A}^+$. In other words, the excess energy is to be carried away by the released electron. As the electron is leaving a neutral complex (antiprotonic atom), the final momentum of the electron does not exceed its initial momentum very much. The formation cross section then drops drastically when the energy release exceeds that of the binding energy of the target electrons as seen in Fig. 23. In the case of molecular targets on the other hand, the exchange collision temporarily forms an antiprotonic molecule, which then dissociate into $\overline{\mathrm{p}}\mathrm{A}^+$ and a residual atom (molecule) [75]. The residual atom (molecule) takes care not only of the excess energy but also of the excess momentum, which may keep the $\overline{\mathrm{p}}\mathrm{A}^+$ formation cross section at a considerable level even beyond the "threshold". As shown in Fig. 24, the FMD calculation [75] predicts a dramatic increase of $\sigma_{\overline{p}p}$ for molecular hydrogen as compared to that for atomic hydrogen far beyond the threshold. The FMD further predicts that the initial n- and l-distributions of $\overline{\mathrm{p}}\mathrm{p}$ for H_2 targets are shifted significantly to smaller values than those for H. These interesting features expected for molecular targets will for the first time be studied through measurements of the final angular and energy distributions of $\overline{\mathrm{p}}\mathrm{A}^+$. Although the temporal antiprotonic molecule formed in $\overline{\mathrm{p}}$ + H_2 collision is predicted to dissociate primarily into $\overline{\mathrm{p}}\mathrm{p}$ + H, metastable exotic molecules will also be searched for.

An important feature to be studied with molecular targets is a "dynamic" Stark effect. As is discussed, the temporal antiprotonic molecule will dissociate into a $\overline{\mathrm{p}}\mathrm{A}^+$ and a spectator atom (molecule), i.e., the $\overline{\mathrm{p}}\mathrm{A}^+$ evolves in the electric field of the spectator atom (molecule) for a finite time, which may considerably increase the branching ratio leading to immediate annihilation of $\bar{p}A^+$ particularly for slow antiprotons.

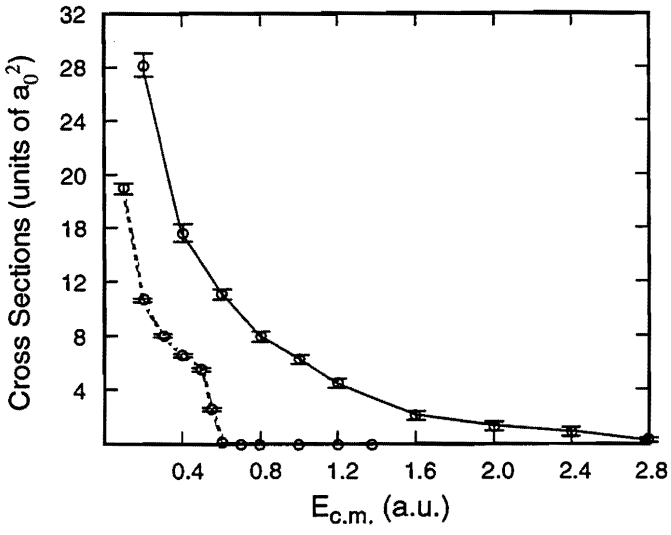

Figure 24: *$\bar{p}p$ formation cross section in $\bar{p}$ + H (the dotted line) and in $\bar{p}$ + H_2 (the solid line) collisions [75]*

4.1.4 Particle Injection into Antiproton Cloud in the Trap

Instead of directing the extracted $\bar{p}$ beam on gaseous target, an alternative way to produce isolated $\bar{p}A^+$ in vacuum is to inject various neutral and charged particles onto antiprotons in the trap.

H^- and He^+ As is seen in Fig. 23, the $\bar{p}p$ formation cross section for $\bar{p}$ + H^- collisions is predicted to be finite ($\sim 10^{-16}$ cm^2) only for an energy window between 0.2 a.u. and 0.8 a.u. in the center-of-mass system. The steep decrease at lower energies is due to the Coulomb repulsion between $\bar{p}$ and H^-, the behavior of which is quite different from that of $\bar{p}$ + H collisions.

An H^- beam of several tens of eV is injected into the trap along its axis. The strong magnetic field helps to focus the beam on the antiproton target. We propose to measure the $\bar{p}p$ formation cross section as a function of the H^- energy. The trap potential is to be tuned so that no effective electric field exists around the trap, which prevents produced $\bar{p}p$ from quenching on their way out from the trap. The formed $\bar{p}p$ will be ejected from the other side of the trap keeping the momentum of the incident H^-. As the quality of the incident H^- beam is quite high in the sense of the angular divergence and energy width, the resultant $\bar{p}p$ is also expected to keep this excellent feature, i.e., one can prepare a high quality $\bar{p}p$ beam in vacuum, which could be used for further investigations. It is noted that the produced $\bar{p}p$s will travel several tens cm during their lifetimes under the present condition.

The yield of $\bar{p}p$ is evaluated to be ~10/sec for the incident H^- beam of 1 nA into a plasma of $\sim 10^6$ antiprotons with a size of $\sim$ 10 mm^3 in the trap. The disturbance on the $\bar{p}$ plasma from the H^- beam should be negligibly small because its density is several orders of magnitude smaller than the antiproton density.

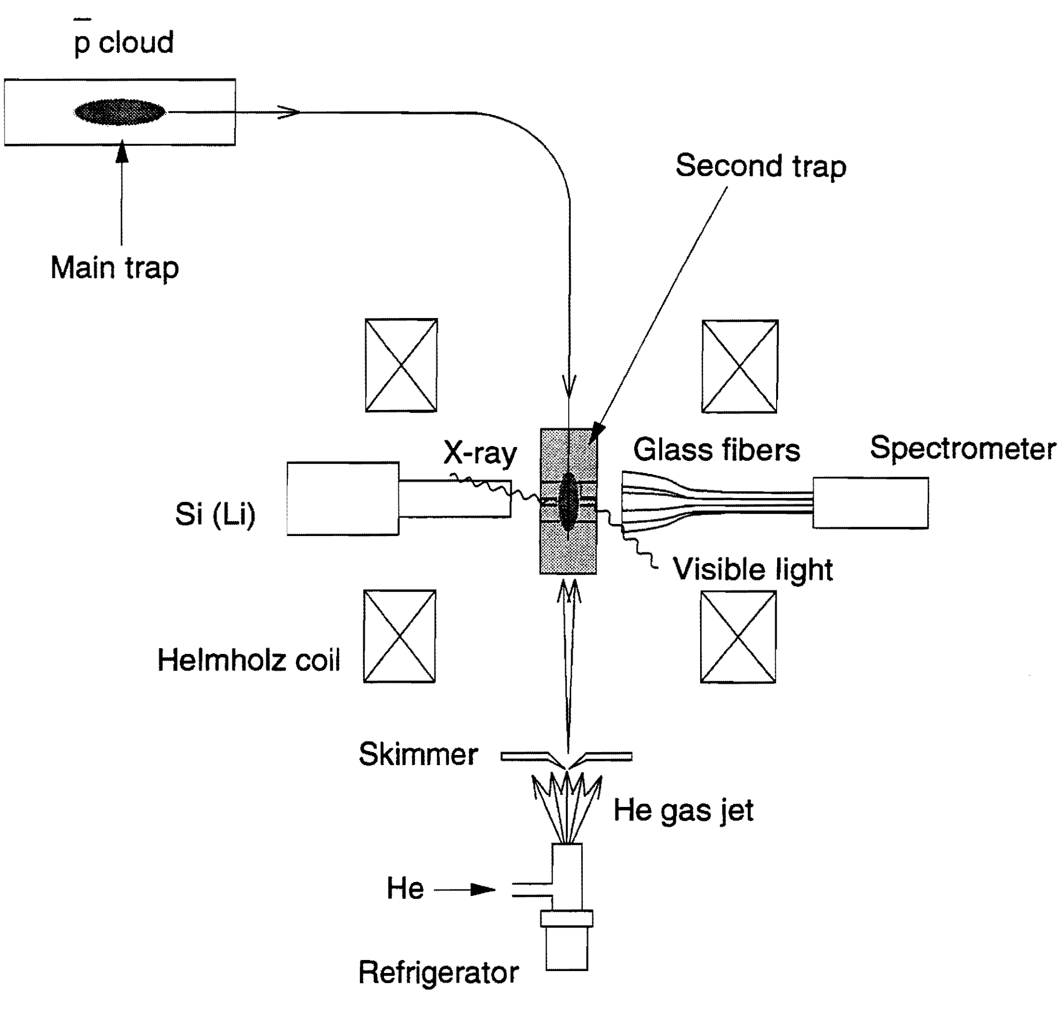

Figure 25: *A schematic experimental setup of He jet injection into the trap*

A similar experiment is planned for a He$^+$ beam, which can again be quite high quality with enough intensity. Although no theoretical predictions on the $\bar{\rm p}{\rm He}^{++}$ formation cross section in $\bar{\rm p}$ + He$^+$ collisions are known, it is expected to be a similar order of magnitude as that of the $\bar{\rm p}{\rm p}$.

Supersonic He and H^0 A collision between a charged particle and a neutral atom (molecule) below a few eV is dominated by the polarization force as is discussed in Appendix B.1. The reaction cross section in this case is expected to be given by $\sigma_{\rm pol} = \pi e\sqrt{2\alpha/\epsilon_{\bar{p}}^{\rm cm}}$ (Eq. (22)).

Here, we propose to measure the $\bar{\rm p}{\rm He}^+$ formation cross section in vacuum by injecting a supersonic well-collimated He beam with an internal temperature of μeV into the trap. This energy range is particularly interesting because the de Broglie wave length of ~ meV antiproton is comparable to or even larger than the size of the target atom. In this case, effectively all $\bar{\rm p}{\rm He}^+$ annihilate in the trap, which allows a high efficient spectroscopy of visible light emitted from $\bar{\rm p}{\rm He}^+$ during their cascading. In order to realize this study, an additional small trap with a Helmholtz type magnet will be prepared, in which cooled $\bar{\mathrm{p}}$s are transferred from the catcher trap. As is schematically drawn in Fig. 25, glass fibers surrounding the small trap will collect visible light emitted from the $\bar{\mathrm{p}}\mathrm{He}^+$, covering a solid angle larger than ~ 1 sr.

The supersonic He beam is prepared with a free jet expansion [77] of high-pressure He gas through a nozzle. During the expansion, the velocity of the gas flow increases and approaches to a so-called terminal velocity $\sqrt{\frac{2kT_0}{m}\frac{\gamma}{\gamma-1}}$ decreasing the internal temperature, where m is the atomic mass of the gas, T_0 is the temperature of the gas before expansion. When the gas is pre-cooled to 30 K, the terminal velocity is $\sim 3 \times 10^2$ m/s ($\sim$ meV) and the internal temperature is below $\sim$ 1K($\sim$ μeV). In this way, a He beam of $10^{10}/\mathrm{cm}^3$ at $\sim$ meV is prepared. The "current" density equivalent of the He beam is as high as $\sim$ 100 $\mu\mathrm{A/cm}^2$. For the supersonic He beam of $10^{13}/\mathrm{cm}^2\mathrm{sec}$ (i.e., $\sim$ 10 $\mu\mathrm{A/cm}^2$) flowing into a cloud of 10^6 $\bar{\mathrm{p}}$, detectable photon intensities are estimated to be $\sim$ 10^2/s assuming the cross section to be $10^{-15}\mathrm{cm}^2$ and the detection efficiency to be 10^{-2}. Plastic scintillators are installed around the trap to monitor the annihilation of $\bar{\mathrm{p}}\mathrm{He}^+$ in the trap, the lifetime of which is evaluated by the time difference between the photon emission and the annihilation.

4.2 Laser spectroscopy of protonium ($\bar{\mathrm{p}}\mathrm{p}$) atoms

4.2.1 Physics motivation

According to Hughes and Deutch [78], recent high-precision comparison of the proton and antiproton cyclotron frequencies [79],

$$\frac{\omega_{\bar{p}}}{\omega_p} = \frac{m_p}{m_{\bar{p}}}\frac{e_{\bar{p}}}{e_p} = 1 + (1.5 \pm 1.1) \times 10^{-9},$$

does not imply equal masses or charges of proton and antiproton at the same precision. This is because the 'antiprotonic Rydberg', $\frac{m_{\bar{p}}}{m_e}\frac{e_{\bar{p}}^2}{e^2}$ times the electron one, obtained by the spectroscopy of antiprotonic atoms has a much lower precision [80]. This relaxes the constraint on the masses and charges to 20 ppm. Hughes and Deutch argued that spectroscopy measurements on antihydrogen could yield an improved test.

The SPSC has approved two AD proposals to produce and study antihydrogen (ATHENA and ATRAP). In these proposals it is argued that the two-photon spectroscopy of the antihydrogen $2s - 1s$ transition could yield a high-precision CPT test. However, this method tests CPT in the lepton sector as the transition energies of antihydrogen depend mostly on the positron mass. For a CPT test in the baryon sector one needs an antiprotonic system whose reduced mass is closer to that of the proton. The simplest such system is protonium (i.e. antiprotonic hydrogen, $\bar{\mathrm{p}}\mathrm{p}$) which is, in addition, much easier to produce than antihydrogen. The information obtained this way should be complementary to that gained from the comparison of hydrogen and antihydrogen.

However, hadronic atoms generally are too much affected by the strong interaction unless (high$-n$, high$-l$) levels can be studied, as in the case of the $\bar{\mathrm{p}}\mathrm{He}^+$ system. Here we propose to measure the antiprotonic Rydberg with high precision by using these metastable protonium states.

4.2.2 Principle

The proposed method to perform the laser spectroscopy of protonium is as follows:

1. Protonium ($\bar{\mathrm{p}}\mathrm{p}$) will be produced in a Stark-free environment. This will be accomplished in one of two ways:

- An ultra-slow antiproton beam ($T \sim 10$ eV) extracted from a catching trap (combined with the RFQ decelerator) will be injected into a very low density hydrogen gas target or jet, where it will produce a slow protonium beam.
- A 10 eV beam of neutral hydrogen molecules or atoms will be brought into the catching trap.

2. Two lasers will induce resonant two-photon absorption between levels with n_i ($\sim 35 - 45$) and n_f ($\sim 50 - 65$). Two-photon absorption makes it possible to achieve high resolution unaffected by the Doppler width caused by the motion of the protonium. A third laser will then be used to ionize $\bar{\mathrm{p}}\mathrm{p}$ from the n_f level.

3. The freed antiproton will be accelerated towards an electrode, its annihilation on which will be detected.

The success of the method described above will rely on the formation of protonium in field-free "vacuum" conditions as it is well known that the dominant deexcitation mechanism of protonium is the Stark mixing induced by the collision of $\bar{\mathrm{p}}\mathrm{p}$ with neighboring H_2 molecules [81].

Formation of protonium in a Stark-free environment

For a $\bar{\mathrm{p}}\mathrm{p}$ kinetic energy of ~10 eV, the Stark mixing rate for principal quantum numbers $20 < n < 100$ is about $4 \times 10^{-10} n^{1/2} N \mathrm{sec}^{-1}$, where N is the hydrogen atomic density per cm^3 [82, 84]. For comparison, the radiative lifetimes for $30 \leq n \leq 50$ are shown in Fig. 26, calculated by adding all $\Delta l = \pm 1$ dipole transition rates [83].

For the Stark mixing rate to be *less* than the radiative rate, a target density of $N \leq 10^{14}$ cm^{-3} ($\sim 10^{-3}$ Torr at room temperature) will be required. If this condition is satisfied, the protonium in large-(n, l) levels are metastable; the lifetimes can be made even longer than the $\bar{\mathrm{p}}\mathrm{He}^+$ case, if suitable (n, l) states can be populated.

Initial (n, l) distribution

In Fig. 27, the initial (n, l) distributions calculated by Cohen et al. [84] by using the classical-trajectory Monte Carlo (CTMC) method are shown for the case of $\bar{\mathrm{p}}$ + H, at various $\bar{\mathrm{p}}$ laboratory energies. For example, with $T_{\bar{p}} \sim 10$ eV, the initial capture would occur preferentially around $n \sim 35 \pm 5$ and $l \sim 30$. These figures show that we need to achieve a relative $\bar{\mathrm{p}}\mathrm{p}$ energy of about 10-20 eV. Figure 27 refers to atomic hydrogen. Recent calculations by Cohen [75] for the case of hydrogen molecules predict a formation cross section and a slight shift of the initial (n, l) distributions to lower n values.

4.2.3 Laser spectroscopy

We propose here to selectively ionize the $\bar{\mathrm{p}}\mathrm{p}$ system in two steps:

1. Let us assume that the initial antiproton kinetic energy is about 15 eV, and the initial n distribution is centered around $n = 43$. By tuning two of the lasers to $\lambda \sim 600$ nm, we can induce a resonant two-photon absorption between the $n = 43$ and $n = 66$ levels. Various choices of initial and final n values are possible, but we will use these numbers here for the purpose of discussion. The fine and hyperfine splittings are small compared to typical laser bandwidths, so that *all* angular momentum states will contribute to the resonance. If the initial n distribution is as sharp as shown in Fig. 27, the $n = 66$ level should be initially empty,

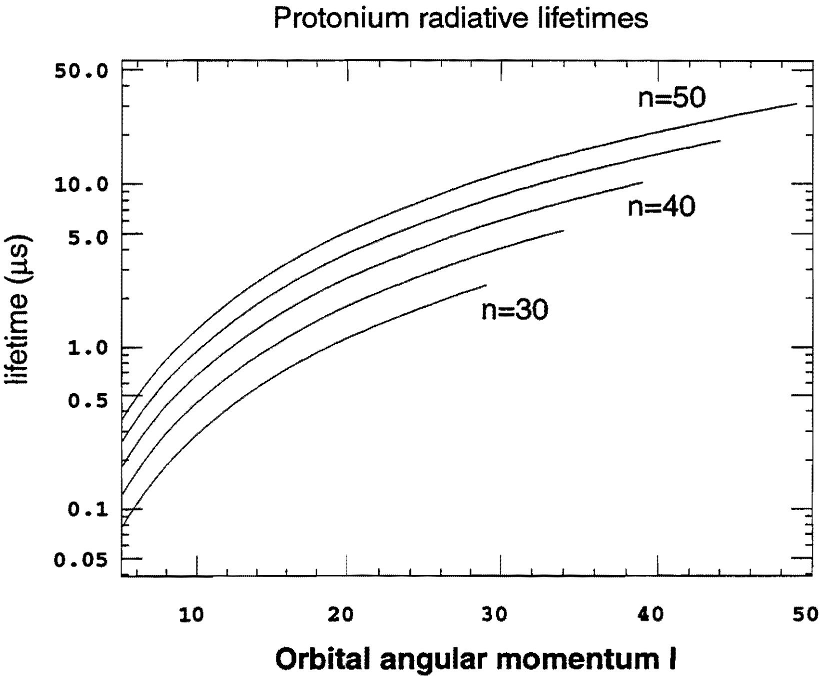

Figure 26: *Radiative lifetimes of* $\overline{p}p$ *for* $30 \leq n \leq 50$.

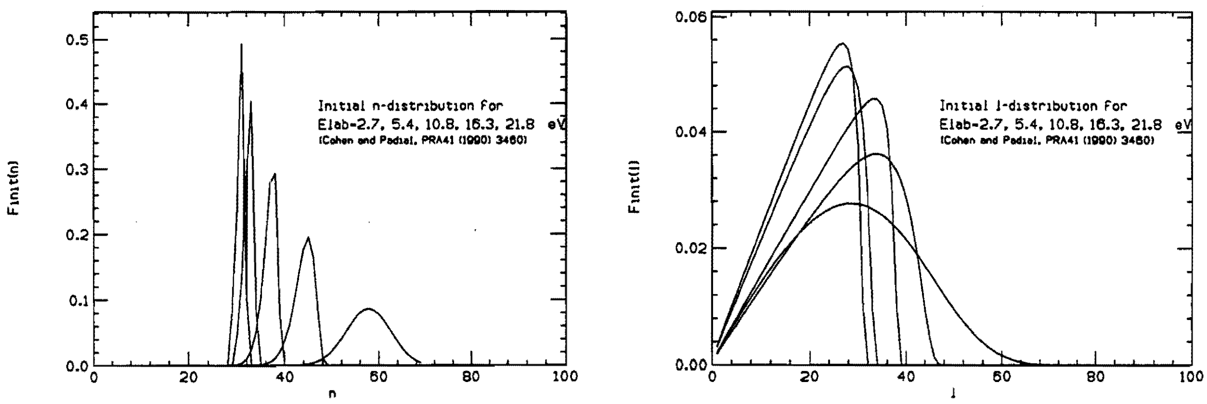

Figure 27: *Initial n-distribution calculated by Cohen for the case of* $\overline{p}$ + *H (left) and l-distribution (right).*

and the populations of the $n = 43$ and $n = 66$ levels will be equalized when the resonance condition is satisfied.

2. With the third laser tuned to a wavelength of $\lambda \leq 400$nm, the $\bar{\text{p}}\text{p}$ can be ionized from the $n = 66$ level.
3. Once the protonium is ionized, the antiproton annihilation can easily be detected by a conventional scintillation or Čerenkov counter.

4.2.4 Resonant two-photon spectroscopy with suppressed Doppler width

The two-photon transition probability is usually very small, but by tuning the laser frequencies so that the intermediate virtual state $|v\rangle$ comes very close to a real one $|k\rangle$, the transition is greatly enhanced (see Fig. 28). The transition matrix element is [85]

$$|\mathcal{M}| \propto \sum_k \frac{\mu_{fk}\,\mu_{ki}}{|E_v - E_k|\,/\,\hbar} \sim \frac{\mu_{fm}\,\mu_{mi}}{\Delta E/\hbar}.$$

If the energy difference ΔE is sufficiently small, the matrix element and therefore the transition probability can be considerably enhanced.

The situation described above is somewhat different from conventional two-photon Doppler-free spectroscopy. If two beams with slightly different (angular) frequencies ω_1, ω_2 are used instead of two photons of the same frequency, the first Doppler width of the resonance is not cancelled but is suppressed by a factor $|\,\omega_1 - \omega_2\,|\,/\,(\omega_1 + \omega_2)$ compared with the Doppler width Δ_D for the case of one-photon transitions. In this case the laser frequencies can be selected and tuned so as to cause quasi-resonance between the intermediate virtual state and one of the real states, and a high enough transition rate can be achieved for otherwise weak two-photon transitions.

The Rabi (angular) frequency for the transition is:

$$\Omega = 8\pi\alpha \frac{\mu_{fm}}{ea_0}\frac{\mu_{mi}}{ea_0}{a_0}^2\frac{I}{\Delta E},$$

where a_0 is the Bohr radius of the hydrogen atom. With typical dipole moments of 0.03 debye $\sim 0.012\,ea_0$ and a pulsed laser of $I = 2$ MW/cm^2 power density and 5 ns pulse length (10 mJ/cm^2 energy),

$$\Omega\Delta t = \frac{4 \times 10^{-5}}{\Delta E\,/\,[\text{eV}]} \times 2\pi.$$

This value has to be close to $\pi/2$, to convert a significant part of the initial state population to the final state. This means $\Delta E \lesssim 1.6 \times 10^{-4}$ eV. This displacement ΔE, on the other hand, should not be too small to avoid sequential single-photon transitions $|i\rangle \to |m\rangle \to |f\rangle$, which are subject to Doppler broadening.

By selecting a favorable combination of initial and final states for which the quasi-resonance is achieved with a small difference in the two laser frequencies, two-photon transition can be induced within the short period of the pulse lengths of the laser beams while keeping the suppressed Doppler width much smaller than the laser bandwidth of ca. 1 GHz. The central frequencies of the resonances can be measured with a precision of better than 10% of the laser bandwidth, i.e. several tens of MHz. Thus we can determine the antiprotonic Rydberg constant to a 10^{-7} precision.

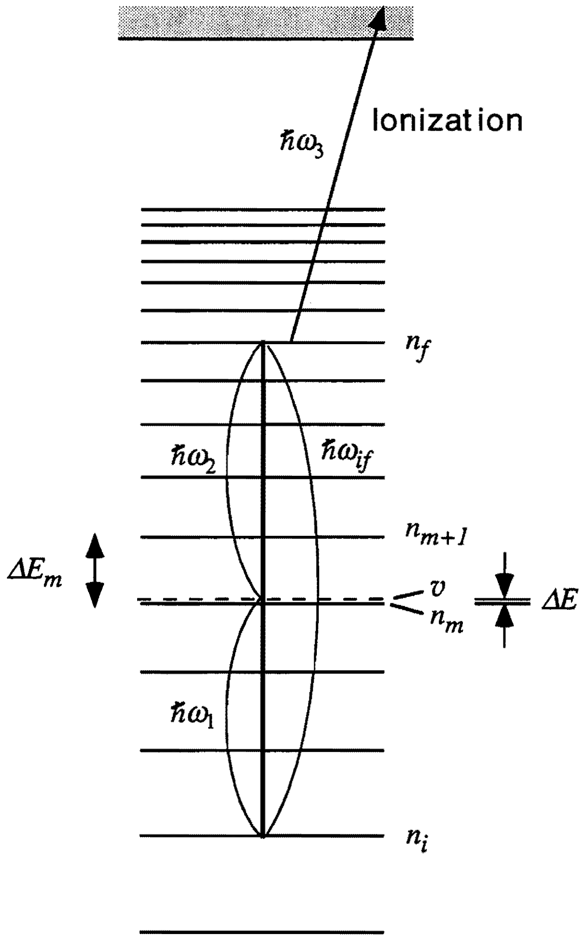

Figure 28: *A schematic of the resonant two-photon spectroscopy of protonium.*

4.2.5 Choice of states and laser systems

For the resonant two-photon transition between the discrete states $|i\rangle$ and $|f\rangle$, two tunable pulsed-laser systems with normal output power in the visible-light range can be used, as discussed in the previous section. The ionization of protonium atoms from the $|f\rangle$ states, on the other hand, requires a UV laser with an energy density of the order of $\sim$ 100 mJ/cm^2. For this purpose an excimer laser or a pulsed YAG laser would be appropriate. A variety of excimer laser wavelengths are available in the UV region by changing gases, ranging from 175 nm (ArCl) to 351 nm (XeF). In the case of a YAG laser, the third- or fourth- order harmonic wavelengths of 355 nm / 266 nm can be used. Some examples of possible and favorable combinations of the initial and final bound states together with the laser wavelengths both for the resonant two-photon transition and the ionization are listed in Table 10.

Quantum numbers			Laser wavelengths [nm]		
n_i	n_m	n_f	$\lambda_{1\,(mi)}$	$\lambda_{2\,(fm)}$	$\lambda_{3\,(\text{ioniz.})}$
45	53	68	719	710	$201 < \lambda_3 < 459$
43	51	66	634	640	$183 < \lambda_3 < 432$
39	50	55	606	607	$151 < \lambda_3 < 300$
39	48	69	444	443	$151 < \lambda_3 < 472$
33	37	43	528	523	$108 < \lambda_3 < 183$

Table 10: *Examples of the possible choice of states and wavelengths of the lasers*

APPENDIX

A Additional results of $\bar{p}\mathrm{He}^+$ atomcule spectroscopy at LEAR

A.1 Laser spectroscopy with fast and slow extraction of $\bar{p}$

In PS205, we accomplished the resonance observation in two ways. Initially, we used the LEAR slow-extracted beam to observe the spike in an event-by-event mode, as shown in the top panel of Fig. 29 for the 470 nm resonance ($(n, l) = (37, 34) \rightarrow (36, 33)$). We later developed a new method of observing the resonance spike in analog DATS using the LEAR fast-extraction mode, as shown in the bottom panel of Fig. 29. Only this latter method is relevant to the present proposal at the AD, where continuous extraction is not possible. Table 11 summarizes the recent results on $\bar{p}\mathrm{He}^+$ spectroscopy at LEAR.

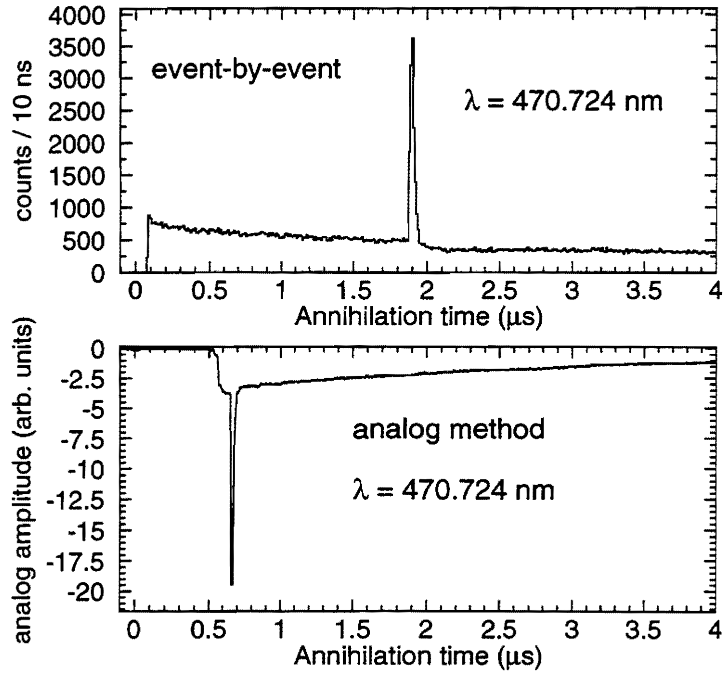

Figure 29: *The laser-induced transitions at 470 nm observed by the event-by-event method (top) and the pulsed-beam analog method (bottom).*

A.2 Precise measurement of the resonant transition frequency and its density shift

High-resolution spectroscopy was performed with the improved laser bandwidth of 1 GHz using an intra-cavity etalon for the 597 and 470 nm transitions. As well as given better comparison with the theoretical calculations (see Figure 30), this revealed the density shift of the resonance frequencies.

We have found that the central resonance frequencies shift with density of the helium medium, and studied this effect systematically [27]. The measurements were made at a large variety of target conditions, ranging from 170 mbar at 6.2 K (density of 1.4 g/ℓ) to 8.0 bar at 5.8 K (127 g/ℓ). The

Table 11: *Summary of the recent results on* $\bar{p}He^+$ *spectroscopy at LEAR. See Fig. 2 for the assignments of the transitions.*

'Favoured' $\bar{p}^4He^+$ transitions	(39,35) → (38,34)	[14]
(metastable → short-lived, v = constant)	(37,34) → (36,33)	[16]
Double resonance	(38,35) → (37,34) → (36,33)	[18]
'Unfavored' transitions	(37,35) → (38,34)	[21]
($\Delta v = 2$)	(37,34) → (38,33)	[21]
Hyperfine splitting	(37,35) → (38,34)	[24]
Lifetimes and populations	(39,35), (38,34), (38,35), (37,34), (36,33)	[15,16,25]
Quenching by H_2	(39,35), (37,34)	[21]
Hydrogen-assisted inverse resonance	(38,35) → (39,36)	[22]
	(38,36) → (39,37)	[22]
	(38,37) → (39,38)	[22]
	(37,34) → (38,35)	[22]
	(37,35) → (38,36)	[22]
	(37,36) → (38,37)	[22]
$\bar{p}^3He^+$ transitions	(38,34) → (37,33)	[17]
	(36,33) → (35,32)	[28]
	(37,34) → (36,33)	[17]

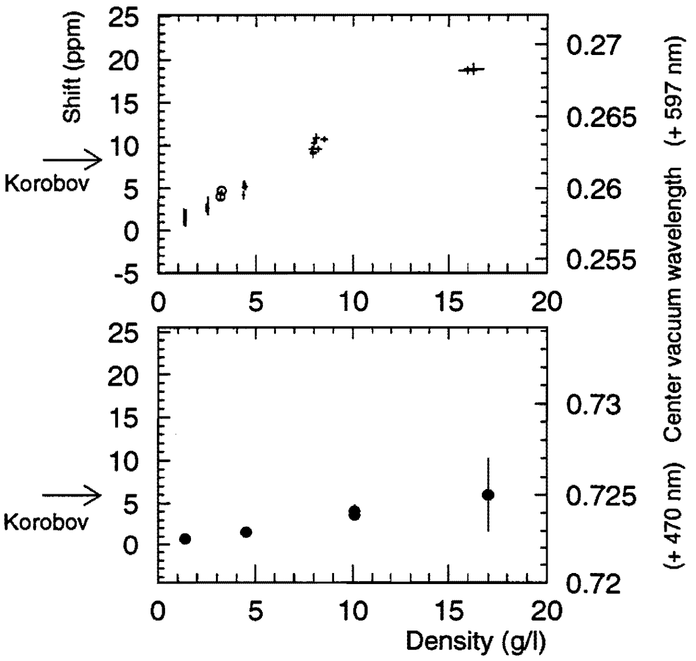

Figure 30: *The central vacuum wavelength plotted against the density of the target helium at rather low-density medium. Theoretical values of Korobov including the relativistic correction [45] are shown for comparison.*

597 and 470 nm lines showed 0.61 ± 0.01 GHz and 0.22 ± 0.05 GHz red-shifts per 1 g/ℓ respectively, and the observed shifts were linear even at the highest density of the super-critical phase. This fact implies that the shift reflects elastic two-body collisions between the $\bar{p}He^+$ atomcule and a helium atom, but why such a large state dependence exists is not understood yet. Our experiment gives complementary data on the collisional interaction together with the density-dependent quenching effect stated in Section A.3. Tempted by these observations, some theoreticians have started to work on this subject. We are looking forward to having a theoretical explanation.

The study of the resonance shift is also important when we compare the transition energies with the theoretical calculations, because the calculation of three-body Coulomb system assumes no collisional effect and thus the theoretical energies must be compared with experimental values extrapolated to the zero-density limit. Thus, the current discrepancy is 8 and 6 ppm for the two lines, after relativistic corrections are taken into account [45]. Further theoretical work to solve these small but significant discrepancies is under way.

A.3 Dependence of the level lifetimes on the helium density

Currently, three methods exist to determine the lifetimes of individual states. In the first of these, the lifetimes of particularly short-lived states (those with $\sim$ 1 ps lifetime) are obtained by measuring the linewidth of the laser resonances [23].

In the second method [15, 16], each $\bar{p}He^+$ atom is irradiated with two successive laser pulses tuned to the same resonance at independently varying times after formation of the $\bar{p}He^+$ atom. The first pulse (at time t_1) induces annihilation from the last metastable state of a constant-v cascade sequence, the number of such annihilations thus constituting a measure of the population of that state at t_1. Natural feeding from higher levels in the cascade then refills the parent state. The number of annihilations induced by a second laser pulse (at time t_2) then measures the recovery of the parent state population between t_1 and t_2, and the population evolution of the parent state is obtained. To extract the lifetimes of individual states from these measurements, cascade models with two and three level sequences of $\Delta n = \Delta l = -1$ transitions are used.

The third is referred to as the "depletion-recovery" method [25]. The on-resonance laser pulse creates a sharp spike on the $\bar{p}He^+$ delayed annihilation time spectrum, which decays with the lifetime of the resonance daughter state. The spectrum then recovers with the lifetime of the parent state, so that the lifetimes of the two states can be directly derived from the shape of the time spectrum.

The time-response characteristics of the laser systems and Cherenkov counters used in the experiment will be optimized so that the lifetimes of both Auger-dominated short-lived states (with nanosecond lifetimes) and metastable states (with microsecond lifetimes) can be measured to high accuracy.

The density dependence of the transitions $(37, 34) \to (36, 33)$ at 470.72 nm, $(38, 35) \to (37, 34)$ at 529.62 nm, and $(39, 35) \to (38, 34)$ at 597.26 nm were studied in pure helium gas at pressures between 0.1 and 9.0 bar, and temperatures between 5.5 and 7.0 K. The lifetimes of the three metastable states $(n, l) = (37, 34)$, $(38, 35)$, and $(39, 35)$ together with two states with large Auger widths $(n, l) = (36, 33)$ and $(38, 34)$ were obtained using a new method for direct measurement of individual state lifetimes. The time spectra of these resonances show depletion-recovery profiles, characterized by a decay with the lifetimes of the resonance daughter states, and a recovery with the lifetimes of the parent states. Using these characteristics, the lifetimes of the parent and daughter states were determined in a model independent way (Fig. 31). The state $(39, 35)$ had a zero-density decay rate of 0.7 μs^{-1}, with no significant change between densities of $2 \cdot 10^{20}$ and $1.9 \cdot 10^{22}$ cm^{-3}. In sharp contrast, the decay rate of the state $(37, 34)$ increased non-linearly with target density, from

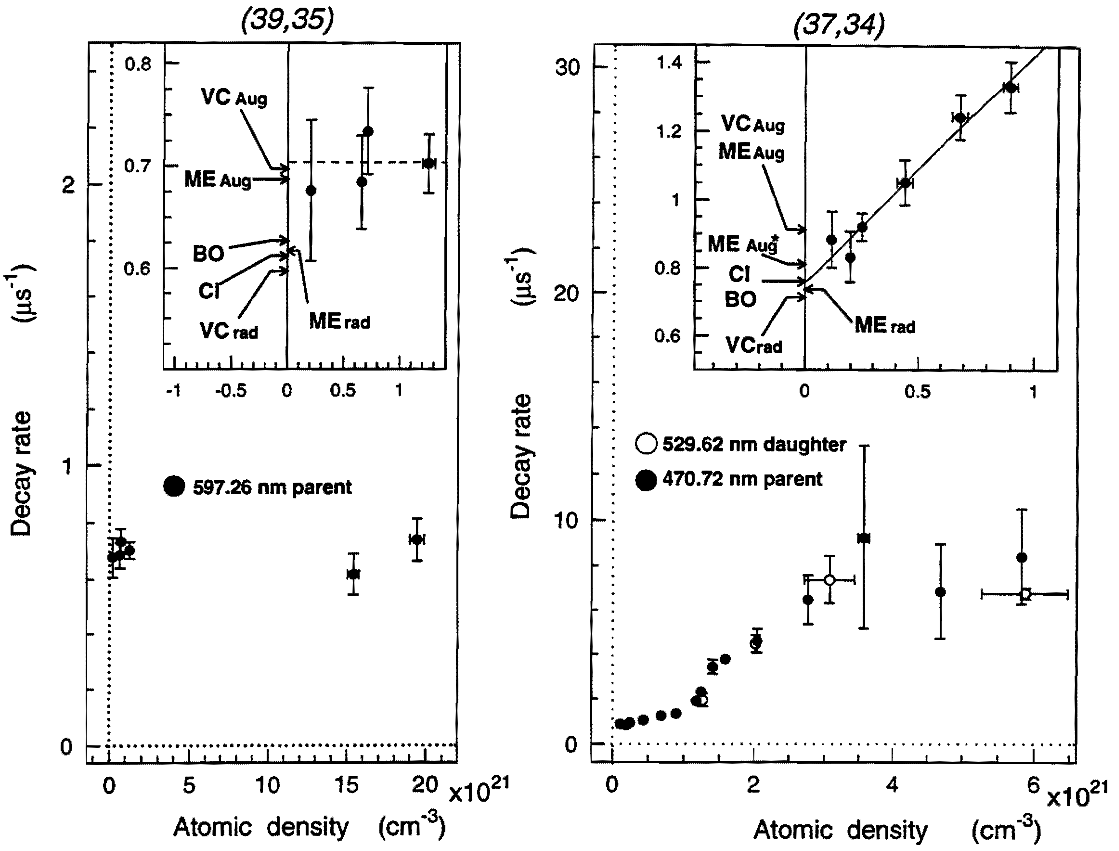

Figure 31: *Decay rates of the states* $(n, l) = (39, 35)$ *and* $(37, 34)$ *measured at various densities using the 470.72 nm, 529.62 nm, and 597.26 nm resonances. Radiative rates from Born-Oppenheimer (BO [6, 7]) and variational calculations (*VC_{rad} *[37] and* ME_{rad} *[45]), sum of Auger and radiative rates from atomic configuration-interaction (CI [31]) and variational calculations (*VC_{Aug} *[36, 37],* ME_{Aug} *[45],* $ME_{Aug}{}^{*}$ *[47]) are shown.*

0.9 μs^{-1} at $1.2 \cdot 10^{20}$ cm^{-3} to 10 μs^{-1} at $5.8 \cdot 10^{21}$ cm^{-3}. This state is responsible for the short-lived component that appears in the overall delayed annihilation time spectra at densities above 10^{21} cm^{-3}. Using the shortened lifetime of the state at high density, the resonance $(38, 35) \to (37, 34)$ at 529.62 nm was reconfirmed. The decay rate of the state $(38, 35)$ was also found to increase with density, from 1.6 μs^{-1} at $\rho = 1.3 \cdot 10^{21}$ cm^{-3}, to 6.4 μs^{-1} at $\rho = 6 \cdot 10^{21}$ cm^{-3}. The measured lifetimes of the metastable states $(37, 34)$ and $(39, 35)$ at the zero density limit agreed with radiative rates calculated with configuration-interaction, Born-Oppenheimer, and molecular variational methods. The Auger-dominated states $(38, 34)$ and $(36, 33)$ had decay rates of 90 ± 10 μs^{-1} and 200 ± 40 μs^{-1}, respectively, which agree with Auger rates calculated using configuration-interaction and molecular variational wave-functions.

An overview of the state-dependent lifetime shortening as the helium density is increased is depicted in Fig. 32.

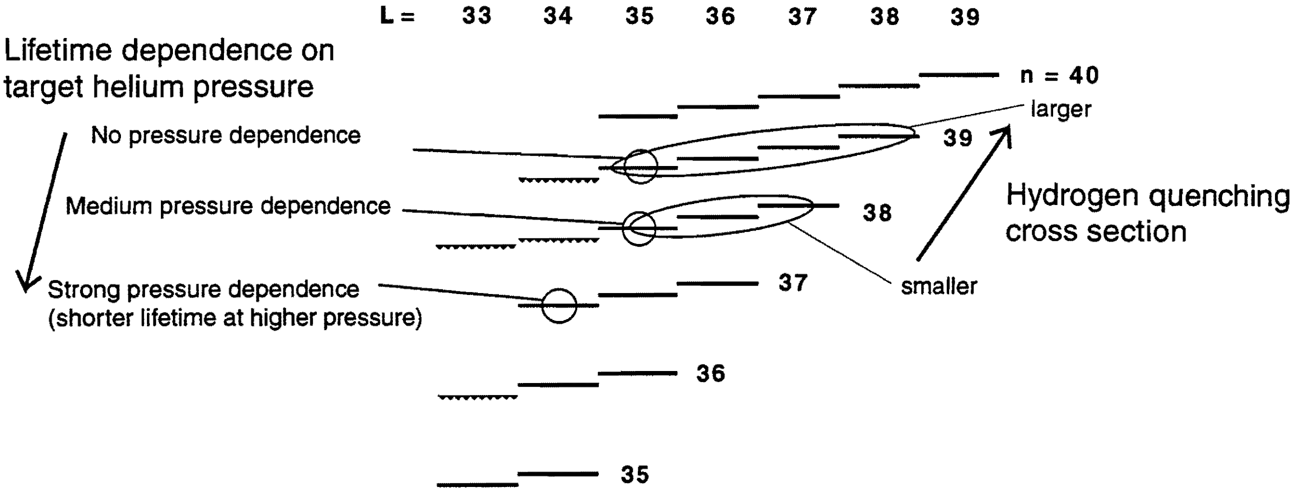

Figure 32: *The collision of* $\bar{p}He^{+}$ *with surrounding helium atoms and hydrogen impurities affect the level lifetimes differently.*

A.4 Laser-tagging studies of the lifetime shortening by H_2

Various quenching phenomena of DATS caused by impurity atoms/molecules have been studied microscopically by using the laser spectroscopic method. The lifetimes of the (n, l) = (39,35) and (37,34) states were determined from studies of the 597 and 470 nm resonances in which the H_2 concentration was changed. The quenching cross section of the (39,35) state was found to be by a factor of 23 larger than that of the lower (37,34) state [21]. The reason for this enormous difference is not yet known.

This selective quenching behavior was used to control the individual lifetimes artificially so that the lifetimes of the upper states (n, l) which are normally metastable are shortened relative to the lower states $(n-1, l-1)$. Thus, inverse laser resonances $(n-1, l-1) \rightarrow (n, l)$ can be detected, if a suitable concentration of H_2 is chosen. This "hydrogen-assisted inverse resonance" (HAIR) method was successfully applied to find 6 inverse resonances $(38, l-1) \rightarrow (39, l)$ with $l = 36, 37, 38$ and $(37, l-1) \rightarrow (38, l)$ with $l = 35, 36, 37$ [22] (see Fig. 2). The success was made possible by measuring analog DATS in the early time range ($\lesssim 0.5$ μs) combined with a pulsed $\bar{p}$ beam from LEAR, since the parent-state lifetimes were shortened to a few 100 ns range.

Although the first HAIR experiments were not complete at all, the lifetimes of the parent and daughter states were determined for selected H_2 concentrations and thus the quenching cross sections $\sigma_q(n, l)$ were deduced for the wide domain of (n, l), as shown in Fig. 6 [26]. To the right-hand side of this figure the $\sigma_q(n, l)$ is converted to the quenching rate for various H_2 concentrations in the "standard" medium condition (30K, 1 bar). The general tendency found is i) rapid increase of $\sigma_q(n, l)$ with n and ii) slow decrease of $\sigma_q(n, l)$ with l for the same n. This is a valuable information on the behavior of this "pseudo-hydrogen" $\bar{p}He^{+}$ atomcule, and extensive studies of HAIR are planned for the era of AD.

The quenching by O_2 was also studied by the laser resonance technique. It did not show such a large state selectivity as in the case of H_2 [29].

B Atomic collisions in very low energy region

B.1 $\overline{\mathrm{p}}\mathrm{A}^+$ formation

A collision between a antiproton and an atom to be discussed here satisfies a so-called adiabatic condition, i.e., $v_{\overline{p}} \ll v_e$, where $v_{\overline{p}}$ and v_e are the velocities of the antiproton and the electron, respectively. When the impact parameter is less than a critical distance (e.g., about $2a_B$ for He target [87], where a_B is the Bohr radius.), the atom is ionized releasing electron(s) and the antiproton leaves the ionized atom alone (ionizing collision). When the kinematic energy of antiproton is small enough so that the released electron can take away the major part of the $\overline{\mathrm{p}}$ kinetic energy, then the antiproton and the ionized atom are bound together in a state with a large principal quantum number $n_{\overline{p}A}$. Energy and momentum conservations before and after the collision require that

$$\frac{1}{2}m_{\overline{p}}v_{\overline{p}}^2 - \epsilon_{ei} = \frac{1}{2}(m_{\overline{p}} + m_A)v_{\overline{p}A}^2 - \epsilon_{\overline{p}A} + \frac{1}{2}m_e v_{ef}^2 \tag{19}$$

$$m_{\overline{p}}v_{\overline{p}} = (m_{\overline{p}} + m_A)v_{\overline{p}A} + m_e v_{ef} \tag{20}$$

where $m_{\overline{p}}$, m_A, and m_e are the antiproton, target atom, and electron masses, respectively. $v_{\overline{p}}$, $v_{\overline{p}A}$ and v_{ef} are the velocities of the incident antiproton, $\overline{\mathrm{p}}\mathrm{A}^+$, and the released electron, respectively. $\epsilon_{ei} > 0$ is the initial binding energy of the electron, $\epsilon_{\overline{p}A} = \frac{\mu_{\overline{p}A}}{m_e}\frac{\epsilon_R}{n_{\overline{p}A}^2} > 0$ is the binding energy of $\overline{\mathrm{p}}\mathrm{A}^+$ after the collision, where $\mu_{\overline{p}A} = \frac{m_{\overline{p}}\, m_A}{m_{\overline{p}} + m_A}$, ϵ_R is the Rydberg constant, and $n_{\overline{p}A}$ is the principal quantum number of the $\overline{\mathrm{p}}\mathrm{A}^+$ system.

Considering that the momentum carried by the released electron is negligibly small, eq.(20) yields $v_{\overline{p}A} = \frac{\mu_{\overline{p}A}}{m_A}v_{\overline{p}}$. Accordingly, one gets

$$\epsilon_{\overline{p}A} \sim \epsilon_{ei} + \epsilon_{ef} - \epsilon_{\overline{p}A}^{\mathrm{cm}} \tag{21}$$

where $\epsilon_{\overline{p}A}^{\mathrm{cm}} = \frac{1}{2}\mu_{\overline{p}A}v_{\overline{p}}^2 = \frac{\mu_{\overline{p}A}}{m_{\overline{p}}}\epsilon_{\overline{p}}$, and $\epsilon_{ef} \;=\; \frac{1}{2}m_e v_{ef}^2$.

As the ionization takes place adiabatically, $m_e v_{ef}$ does not exceed the initial electron momentum very much, i.e., $\epsilon_{ef} \lesssim \epsilon_{ei}$. This relation indicates that

1. the formation cross sections of $\overline{\mathrm{p}}\mathrm{A}^+$ are appreciable only when $\epsilon_{\overline{p}}^{\mathrm{cm}}$ is comparable to or less than ϵ_{ei}, and

2. $\epsilon_{\overline{p}A}$ and accordingly $n_{\overline{p}A}$ are "tunable" by varying the incident kinetic energy of antiprotons.

When $E_{\overline{p}}^{\mathrm{cm}}$ is increased from 0 to ϵ_{ei}, $\epsilon_{\overline{p}A}$ decreases from ϵ_{ei} to 0. In other words, $n_{\overline{p}A}$ increases from $n_{\overline{p}A}^{min} \sim \sqrt{\mu_{\overline{p}}/m_e}$ (e.g. $\sim$ 30 and 40 for H and He targets, respectively) to $n_{\overline{p}A}^{max} \to \infty$. As the antiproton can feel the target potential only when the impact parameter is smaller than the radius of the target atom ($\sim a_B$), the angular momentum quantum number of $\overline{\mathrm{p}}\mathrm{A}^+$, $l_{\overline{p}A}$, could be as high as $\sim \mu_{\overline{p}A}\ v_{\overline{p}}\ a_B \sim \sqrt{\mu_{\overline{p}A}/m_e}\ \hbar$, i.e., a considerable fraction of $\overline{\mathrm{p}}\mathrm{A}^+$ is expected to be stabilized because of their high $l_{\overline{p}A}$. It is noted that very little is known experimentally on these basic quantities.

Theoretical studies are also fairly limited primarily because a tremendous number of reaction channels are involved in the collision as is imagined from the estimated $n_{\overline{p}A}$ and $l_{\overline{p}A}$ values. Available predictions known to us are obtained employing a classical trajectory Monte Carlo simulation (CTMC) [84] and a so-called Fermion Molecular Dynamics (FMD) [76].

The solid lines in Fig. 23 shows the CTMC prediction of $\overline{\mathrm{p}}\mathrm{p}$ formation cross section, $\sigma_{\overline{p}p}$, for $\overline{\mathrm{p}}$ + H and $\overline{\mathrm{p}}$ + H$^-$ collisions. It is seen that $\sigma_{\overline{p}p}$ for H does show a threshold at $\epsilon_{\overline{p}}^{\mathrm{cm}} \sim \epsilon_{ei}$ and increases monotonically as $\epsilon_{\bar{p}}^{\rm cm}$ decreases. On the other hand, $\sigma_{\bar{p}p}$ for H$^-$ shows two thresholds, and is finite only when 0.2 a.u. $\lesssim \epsilon_{\bar{p}}^{\rm cm} \lesssim$ 0.7 a.u. Considering the binding energy of H$^-$ is $\sim$ 0.8 eV, the spacial extension of which is estimated to be $\sim$ 5 a.u. Accordingly, the incoming antiproton should have a kinetic energy larger than $\sim$ 0.2 a.u. to overcome the Coulomb barrier, which is reflected in the two thresholds of $\sigma_{\bar{p}p}$ for H$^-$. The CTMC further predicts that the average values of $n_{\bar{p}p}$ for H and H$^-$ at $\epsilon_{\bar{p}}^{\rm cm} \sim \epsilon_{ei}$ are around 100 and 45, respectively. Smaller $n_{\bar{p}p}$ for H$^-$ as compared with that for H again reflects the fact that an effective kinetic energy of antiproton at the moment of collision with H$^-$ is reduced due to the mutual repulsive force.

An important implication of the CTMC results (Fig. 23) is that $\sigma_{\bar{p}p}$ for H increases drastically as $\epsilon_{\bar{p}}^{\rm cm}$ decreases to zero. This peculiar feature is understood to originate from an effective interaction potential produced by the combination of a polarization potential, $-\alpha e^2/2r^4$, and the centrifugal potential, $l(l+1)\hbar^2/2\mu_{\bar{p}A}r^2$, where α denotes the atomic polarizability of the target atom. The combined effective potential has a barrier of $l^2(l+1)^2\hbar^4/8\mu_{\bar{p}A}^2\alpha e^2$ at $r = (\alpha e^2/\epsilon_{\bar{p}}^{\rm cm})^{1/4}$. When $\epsilon_{\bar{p}}^{\rm cm}$ is larger than the barrier height, the antiproton can reach the interior of the target atom (molecule). The critial impact parameter to overcome the barrier is given by $b_0 = (2\alpha e^2/\epsilon_{\bar{p}}^{\rm cm})^{1/4}$, and the corresponding angular momentum becomes $(8\alpha e^2\mu_{\bar{p}A}^2\epsilon_{\bar{p}}^{\rm cm})^{1/4}$. If some energy dissipating mechanism functions during the antiproton is in the interior, it is captured by the target atom (molecule), the cross section of which is given by

$$\sigma_{\rm pol} = \pi b_0^2 = \pi e\sqrt{2\alpha/\epsilon_{\bar{p}}^{\rm cm}} \;\propto\; v_{\bar{p}}^{-1}, \tag{22}$$

which is a so-called Langevin cross section. The energy dissipation is taken care of by releasing a target electron, i.e., $\bar{\rm p}$ + H $\rightarrow$ $\bar{\rm p}$p + e$^-$.

B.2 Charged particle drift in gaseous media

The swarm has been known to be a powerful technique to study low-energy ion-atom (molecule) collisions, which will in the present case enable to investigate the formation process of $\bar{\rm p}$A$^+$.

The mean free path of a charged particle in a target with density ρ is given by $(\rho\sigma_{\rm eff})^{-1}$, where $\sigma_{\rm eff}$ is an effective scattering cross section responsible for the energy dissipation. When an electric field E is applied, the energy gain of the particle between a successive collision, ϵ_d, amounts to $eE(\rho\sigma_{\rm eff})^{-1}$. Assuming $\sigma_{\rm eff} \sim \sigma_{\rm pol}$ (eq.(22)), one finds that

$$\epsilon_d = \frac{1}{2\pi^2\alpha}\frac{\mu_{\bar{p}A}}{m_{\bar{p}}}\frac{E^2}{\rho^2}, \tag{23}$$

i.e., the drift energy is controllable and is proportional to the square of E.

In the case of antiproton in He (α = 0.2 Å^3) of 1 Torr at 300 K, we get

$$\epsilon_d \;({\rm eV}) \sim 2\times 10^{-3}\; E \;\;({\rm V/cm})^2 \tag{24}$$

As in the case of $\bar{\rm p}$ + H collision(figure 23), the cross section of $\bar{\rm p}$He$^+$ formation is also expected to decrease drastically around the ionization threshold of He. Thus $\epsilon_{\bar{\rm p}{\rm He}}^{\rm cm} \sim$ 30 eV is expected to be critical to form $\bar{\rm p}$He$^+$, which is achievable at E = 120 V/cm.

C An RFQ post $\bar{p}$ decelerator and a catcher trap

Big efforts have been made in the last decade to develop an ultra slow antiproton beam by (i)preparing a antiproton beam of a few tens keV by degrading 5 MeV antiprotons supplied from LEAR, and (ii)injecting them in a Penning trap for electron-cooling (PS200). It has been proved that these antiprotons can be cooled down at least to sub-eV range [86] with a trapping efficiency of $\sim$ 1%. This relatively low efficiency resulted because the angular and energy spreads of the degraded antiprotons are very large.

Following a similar procedure as PS200 but aiming at much higher trapping efficienty and production of high quality antiproton beams in a few eV to 100 keV region, we adopt a combination of a RFQ and a Penning catcher trap.

Antiprotons from AD are expected to have the following properties:

Energy	5.8 MeV $\Delta E/E = 0.2\%$
Emittance	1 π mm mrad
Repetition	1 per min
Intensity	$\sim 1 \times 10^7$ $\bar{p}$/ pulse

The antiproton beam from the AD is pre-bunched and then injected into the RFQ, which further slows it down to 50 keV. A debuncher following the RFQ will provide a antiproton beam with energies between 20 and 190 keV, which will be used for experiments proposed in Section 3. The characteristics of the antiproton beam from "the RFQ + the debuncher" is expected to be:

Energy	190 keV to 20 keV
Transmission	40 % for 50 keV ± 5 keV
Emittance	180 π mm mrad @ 50 keV
Repetition	1 per min.
Time width of one beam pulse	$\sim$ 250 ns
Intensity	$\sim 4 \times 10^6$ $\bar{p}$/pulse for 50 keV ± 5 keV

An expected energy distribution of antiproton from the RFQ is shown in Fig. 33, which indicates a sharp peak centered around 50keV. On the other hand, a non-negligible high energy component is observed, which is to be taken into account in designing experimental setups which use the direct beam from the RFQ.

To further decelerate the antiproton beam, a new catcher trap has been designed. The antiproton beam of 50keV from the RFQ is injected in the trap via an aluminum foil of $\sim$ 4000 Å thick located just in front of the trap, which degrades 50 keV antiprotons to less than $\sim$ 10 keV. The overall trapping efficiency including that of the RFQ is estimated to be better than 30%, i.e., $\sim 3 \times 10^6$ $\bar{p}$/min. The spot size of the antiproton cloud in the trap is simulated to be less than a few mm. The space charge of the antiproton cloud amounts to $\sim$10 eV although the temperature of cooled antiprotons is less than meV.

The cooled antiproton beam will be extracted at 1.5 keV from the trap to prevent serious divergence during extraction. The collision energy will be tuned by varying the bias of the whole trap and the beamline. In most experiments with ultra slow antiprotons, we use a gaseous target which is directly connected to the trap without any window, i.e., efficient differencial pumping stages separated by small apertures are necessary. Beam transport features have been simulated and reasonable transport parameters are found.

Trapping and cooling features will fully be tested experimentally before the year 2000 employing H^- beams of a similar quality. As the binding energy of H^- is $\sim$ 0.8 eV, the electron cooling of

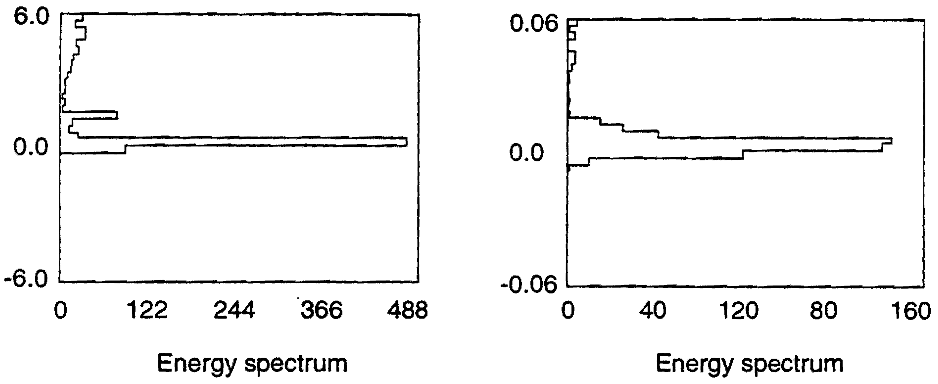

Figure 33: *Energy distribution of antiproton beam from the RFQ. The ordinates of both figures are given in MeV.*

$\lesssim 1$ keV H^- can be done without serious problem. A superconducting 5 T solenoid for the trap is newly designed (Fig. 34), which has a flat top magnetic field distribution with effective length of ~ 1 m .

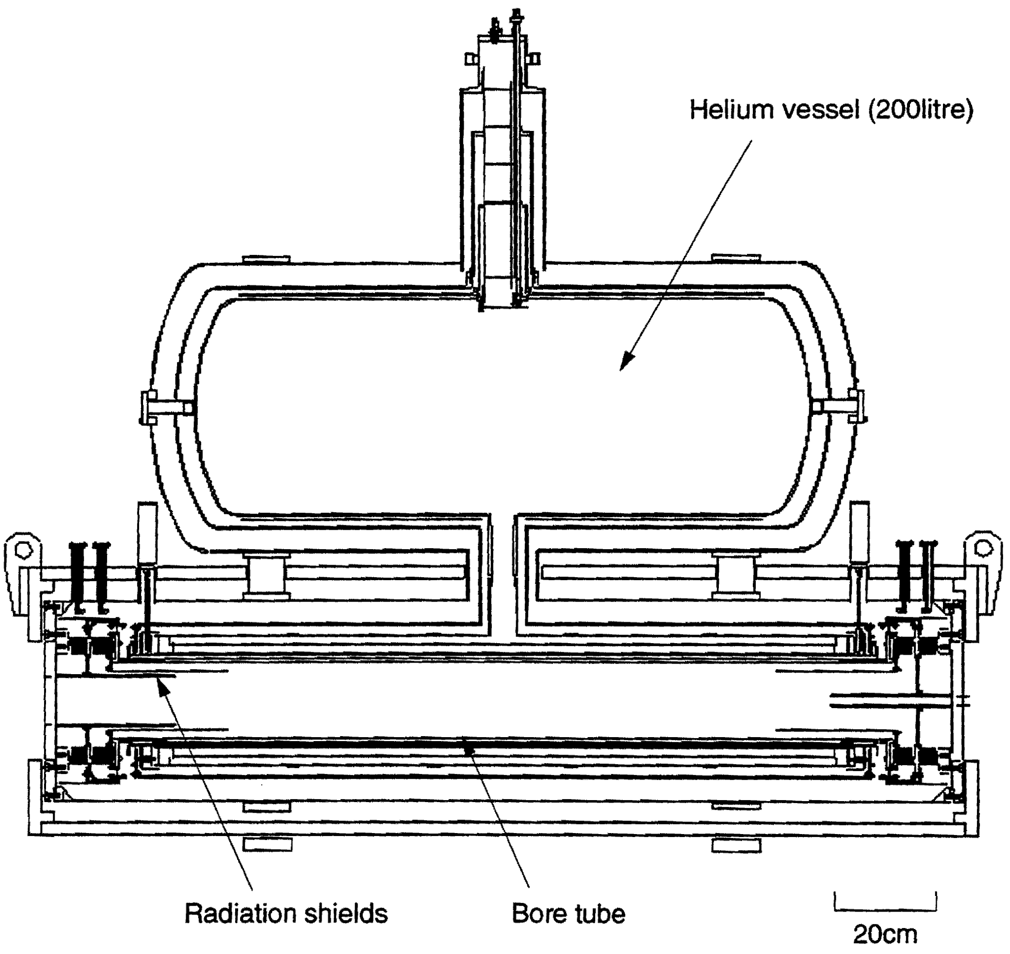

Figure 34: *An outlook of the superconducting magnet of the catcher trap*

D Infrastructure requirements

In order to perform the experiments proposed in the previous sections, we will need the following infrastructure at the AD experimental hall:

Basic infrastructure (Year 1999)		
experiment area	size	8 × 20 m for installation of RFQ and trap
buildings	1 laser hut	size ~ 5 × 10 m adjacent to the beam area metallic walls for dust-free environment air conditioned (stable temperature!)
	1 electronics barrack (~ 2.5 × 5 m)	next or above laser hut
	1 data analysis barrack (~ 2.5 × 5 m)	next or above laser hut
	1 preparation space	close to exp. area, ~ 5 × 5 m
cooling water	lasers	2 × 23 ℓ/min, < 30 °C 2 × 1 ℓ/min, < 22 °C
power supplies	laser hut	air condition, power to be decided
	lasers	2 × 380 VAC, 3-phase, 15 A/phase 2 × 230 VAC, 1-phase, 2 A
	pumps (roughing, turbomolecular)	230 VAC 1 phase 6 kW
	electronics, computers	230 VAC 1 phase 10 kW
cryoliquids	liquid N_2	15 ℓ/day
	liquid He	< 100 ℓ/day helium recuperation system needed
gas supplies	N_2	small quantities
	He-4	small quantities
computing	Ethernet	about 10 ports of 10/100 base T external network connection needed
	off-line	small scale access to CERN PLUS (public interactive services) access to public batch services for theoretical calculations

Table 12: *Necessary infrastructure at the AD — part 1*

RFQ (Year 2000)		
space	RFQ length incl. buncher cavity	$\sim$ 9 m
	RFQ power chain	amplifier, driver: twice 1.1 × 1.1 m HV modulator: 2.4 × 1.1 m 8 standard racks (0.55 × 0.8 m)
	distance to resonator: 10–15 m	
electric power RFQ	amplifier	230/400 VAC 3-phase 63 A
	driver	230/400 VAC 3-phase 63 A
	HV modulator	230/400 VAC 3-phase 125 A
	predriver chain	230/400 VAC 3-phase 25 A
electric power buncher & debuncher	amplifier	230/400 VAC 3-phase 15 A
	driver	230/400 VAC 3-phase 15 A
	predriver chain	230/400 VAC 3-phase 25 A
water	demineralized	20 ℓ/min, 6 bar
Trap (Year 2000)		
space	length after RFQ incl. extraction	$\sim$ 6 m
electric power		200 VAC, 3 phases, 20 kVA
		100 VAC, 1 phase, 20 kVA

Table 13: *Necessary infrastructure at the AD — part 2*

The detailed design of the laser hut meeting the requirements of a dust-free room with stable temperature will have to be worked out with the responsible people at CERN and local manufacturers. Our collaboration is ready to cover the expenses for the laser hut. The position of the barracks for data aquisition and analysis have to be decided based on the available space in the AD hall. The power supplies for the electronics, computer, and lasers should be isolated from the electric power for the RFQ, to prevent radiofrequency noise from interfering with our high-sensitivity measurements.

E Cost estimate

In the following the estimated cost or availability of the major equipment needed is listed, together with the responsible institute.

item	cost	contributing institution
infrastructure		
laser hut	500 kCHF	Shinpro
laser system & components	800 kCHF	Shinpro
RFQ	1000 kCHF	Shinpro
magnet for Trap	1000 kCHF	Shinpro
Trap components, electronics	200 kCHF	Shinpro
computers (off-line)	50 kCHF	Shinpro
first year		
electronics, detectors	50 kCHF	Shinpro
cryostats & gas system	100 kCHF	Shinpro
microwave components	200 kCHF	Shinpro
experiments using the RFQ beam		
cryostat	30 kCHF	Shinpro
Cerenkov counter	5 kCHF	Shinpro
electrostatic energy analyser	70 kCHF	Aarhus
scattering chamber for energy loss	exists	Aarhus
scattering chamber for channeling and goniometer	150 kCHF	Shinpro
annular $\bar{p}$ detector for channeling	exists	GSI
drift chamber	50 kCHF	Shinpro
track detector system for swarm	100 kCHF	Shinpro
experiments using the trap		
collision chamber and pumps for ionization	60 kCHF	Aarhus
detectors for ionization	30 kCHF	Aarhus
reaction microscope	exists	GSI
collision chamber for $\bar{p}$ capture	exists	Shinpro
atomic hydrogen source	exists	St. Patrick's College / KVI
H^-, He^- ion source	200 kCHF	Shinpro
superconducting Helmholtz coil	350 kCHF	Shinpro
supersonic He beam source	100 kCHF	Shinpro
visible light spectrometry system	100 kCHF	Shinpro

Table 14: *Estimated cost of experimental installation*

References

[1] M. Iwasaki, S. N. Nakamura, K. Shigaki, Y. Shimizu, H. Tamura, T. Ishikawa, R. S. Hayano, E. Takada, E. Widmann, H. Outa, M. Aoki, P. Kitching, and T. Yamazaki, Phys. Rev. Lett. **67**, 1246 (1991).

[2] G. T. Condo, Phys. Lett. **9**, 65 (1964).

[3] J. E. Russell, Phys. Rev. Lett. **23**, 63 (1969); Phys. Rev. **188**, 187 (1969); Phys. Rev. **A1**, 721 (1970); Phys. Rev. **A1**, 735 (1970); Phys. Rev. **A1**, 742 (1970).

[4] R. Ahlrichs, O. Dumbrajs, H. Pilkuhn, H. G. Schlaile, Z. Phys. A **306**, 297 (1982).

[5] T. Yamazaki and K. Ohtsuki, Phys. Rev. A **45**, 7782 (1992).

[6] I. Shimamura, Phys. Rev. A **46**, 3776 (1992), and private communication.

[7] P. T. Greenland and R. Thürwächter, Hyperfine Interact. **76**, 355 (1993), and private communication.

[8] T. Yamazaki, E. Widmann, R.S. Hayano, M. Iwasaki, S. N. Nakamura, K. Shigaki, F. J. Hartmann, H. Daniel, T. von Egidy, P. Hofmann, Y. -S. Kim, and J. Eades, Nature **361**, 238 (1993).

[9] S. N. Nakamura, R. S. Hayano, M. Iwasaki, K. Shigaki, E. Widmann, T. Yamazaki, H. Daniel, T. von Egidy, F. J. Hartmann, P. Hofmann, Y. -S. Kim, and J. Eades, Phys. Rev. A **49**, 4457 (1994).

[10] E. Widmann, I. Sugai, T. Yamazaki, R. S. Hayano, M. Iwasaki, S. N. Nakamura, H. Tamura, T. M. Ito, N. Morita, F. J. Hartmann, H. Daniel, T. von Egidy, W. Schmid, J. Hoffmann, and J. Eades, Phys. Rev. A **51**, 2870 (1995).

[11] B. Ketzer, F. J. Hartmann, H. Daniel, T. von Egidy, A. Niestroj, S. Schmid, W. Schmid, T. Yamazaki, I. Sugai, K. Nakayoshi, R. S. Hayano, F. E. Maas, H. A. Torii, T. Ishikawa, H. Tamura, N. Morita, D. Horváth, J. Eades and E. Widmann, Phys. Rev. A **53**, 2108 (1996).

[12] E. Widmann, I. Sugai, T. Yamazaki, R. S. Hayano, M. Iwasaki, S. N. Nakamura, H. Tamura, T. M. Ito, A. Kawachi, N. Nishida, W. Higemoto, Y. Ito, N. Morita, F. J. Hartmann, H. Daniel, T. von Egidy, W. Schmid, J. Hoffmann, and J. Eades, Phys. Rev. A **53**, 3129 (1996).

[13] N. Morita, K. Ohtsuki, T. Yamazaki, Nucl. Instr. Meth. A **330**, 439 (1993).

[14] N. Morita, M. Kumakura, T. Yamazaki, E. Widmann, H. Masuda, I. Sugai, R. S. Hayano, F. E. Maas, H. A. Torii, F. J. Hartmann, H. Daniel, T. von Egidy, B. Ketzer, W. Müller, W. Schmid, D. Horváth, and J. Eades, Phys. Rev. Lett. **72**, 1180 (1994).

[15] R. S. Hayano, F. E. Maas, H. A. Torii, N. Morita, M. Kumakura, T. Yamazaki, H. Masuda, I. Sugai, F. J. Hartmann, H. Daniel, T. von Egidy, B. Ketzer, W. Müller, W. Schmid, D. Horváth, J. Eades, and E. Widmann, Phys. Rev. Lett. **73**, 1485 (1994); **73**, 3181(E) (1994).

[16] F. E. Maas, R. S. Hayano, T. Ishikawa, H. Tamura, H. A. Torii, N. Morita, T. Yamazaki, I. Sugai, K. Nakayoshi, F. J. Hartmann, H. Daniel, T. von Egidy, B. Ketzer, A. Niestroj, S. Schmid, W. Schmid, D. Horváth, J. Eades, and E. Widmann, Phys. Rev. A **52**, 4266 (1995).

[17] H. A. Torii, M. Hori, T. Ishikawa, F. E. Maas, R. S. Hayano, N. Morita, M. Kumakura, I. Sugai, B. Ketzer, H. Daniel, F. J. Hartmann, R. Pohl, R. Schmidt, T. von Egidy, D. Horváth, J. Eades, E. Widmann, and T. Yamazaki, Phys. Rev. A **53**, R1931 (1996).

[18] R. S. Hayano, T. Ishikawa, H. Tamura, H. A. Torii, M. Hori, F. E. Maas, N. Morita, M. Kumakura, I. Sugai, F. J. Hartmann, H. Daniel, T. von Egidy, B. Ketzer, R. Pohl, D. Horváth, J. Eades, E. Widmann, and T. Yamazaki, Phys. Rev. A**55**, R1 (1997).

[19] H. A. Torii, R. S. Hayano, F. E. Maas, M. Hori, N. Morita, M. Kumakura, T. Yamazaki, H. Masuda, I. Sugai, B. Ketzer, F. J. Hartmann, H. Daniel, T. von Egidy, W. Müller, W. Schmid, A. Niestroj, D. Horváth, J. Eades and E. Widmann, Nucl. Instrum. Methods A **396**, (1996) 257.

[20] A. Niestroj, F.J. Hartmann, H. Daniel, B. Ketzer, T. von Egidy, F.E. Maas, R.S. Hayano, T. Ishikawa, H. Tamura, H.A. Torii, N. Morita, T. Yamazaki, I. Sugai, K. Nakayoshi, D. Horváth, J. Eades, E. Widmann, Nucl. Instrum. Methods A **373**, (1996) 411.

[21] T. Yamazaki, B. Ketzer, E. Widmann, J. Eades, H. Daniel, F. J. Hartmann, M. Hasinoff, R. Pohl, R. Schmidt, T. von Egidy, D. Horváth, M. Kumakura, N. Morita, I. Sugai, Y. Fujita, H. A. Torii, M. Hori, T. Ishikawa, F. E. Maas, H. Tamura, and R. S. Hayano, Chem. Phys. Lett. **265**, 137 (1997).

[22] B. Ketzer, F. J. Hartmann, T. von Egidy, C. Maierl, R. Pohl, J. Eades, E. Widmann, T. Yamazaki, M. Kumakura, N. Morita, R. S. Hayano, M. Hori, T. Ishikawa, H. A. Torii, I. Sugai, and D. Horváth, Phys. Rev. Lett. **78**, 1671 (1997).

[23] T. Yamazaki, E. Widmann, J. Eades, M. Kumakura, N. Morita, H. A. Torii, M. Hori, T. Ishikawa, F. E. Maas, H. Tamura, R. S. Hayano, I. Sugai, Y. Fujita, H. Daniel, B. Ketzer, H. Daniel, F. J. Hartmann, R. Pohl, R. Schmidt, T. von Egidy, and D. Horváth, Phys. Rev. A **55**, R3295 (1997).

[24] E. Widmann, J. Eades, T. Yamazaki, H. A. Torii, R. S. Hayano, M. Hori, T. Ishikawa, M. Kumakura, N. Morita, I. Sugai, F J. Hartmann, T. von Egidy, B. Ketzer, C. Maierl, R. Pohl, and D. Horváth Phys. Lett. **B404**, 15 (1997).

[25] M. Hori, A. Torii, R.S. Hayano, T. Ishikawa, F.E. Maas, H. Tamura, B. Ketzer, F.J. Hartmann, R. Pohl, C. Maierl, T. von Egidy, M. Kumakura, N. Morita, I. Sugai, D. Horv'ath, E. Widmann, J. Eades and T. Yamazaki, submitted to Phys. Rev. A.

[26] B. Ketzer, F. J. Hartmann, T. von Egidy, C. Maierl, R. Pohl, J. Eades, E. Widmann, T. Yamazaki, M. Kumakura, N. Morita, R. S. Hayano, M. Hori, T. Ishikawa, H. A. Torii, I. Sugai, and D. Horváth, submitted to J. Chem. Phys.

[27] H.A. Torii, R.S. Hayano, M. Hori, T. Ishikawa, N. Morita, M. Kumakura, T. Yamazaki, I. Sugai, B. Ketzer, F. J. Hartmann, T. von Egidy, R. Pohl, C. Maierl, D. Horváth, J. Eades and E. Widmann, to be submitted to Phys. Rev. A.

[28] C. Maierl, Master thesis, Technische Universität München (1997), unpublished.

[29] R. Pohl et al., to be submitted.

[30] W. A. Beck, L. Wilets and M.A. Alberg, Phys. Rev. A **48**, 2779 (1993).

[31] K. Ohtsuki, private communication.

[32] T. Yamazaki and K. Ohtsuki, Phys. Rev. A **50**, 5350 (1994).

[33] O. I. Tolstykhin, S. Watanabe and M. Matsusawa, Phys. Rev. Lett. **74**, 3573 (1995).

[34] O. I. Tolstykhin, S. Watanabe and M. Matsusawa, Phys. Rev. A **54**, R3705 (1996).

[35] F. Benvenuto, G. Casati and D. L. Shepelyanski, Phys. Rev. A **53**, 737 (1996).

[36] S. I. Fedotov, O. I. Kartavtsev, and D. E. Monakhov, At. Nucl. **59**, 1662 (1996).

[37] O. I. Kartavtsev, At. Nucl. **59**, 1483 (1996).

[38] O. I. Kartavtsev, Hyperfine Interactions, **103**, 369 (1996).

[39] D. Bakalov, I. V. Puzynin, T. P. Puzynina, S. I. Vinitsky, Phys. Lett. **A211**, 223 (1996).

[40] D. Bakalov, I. V. Puzynin, T. P. Puzynina, S. I. Vinitsky, Hyperfine Interactions, **101/102** 487 (1996).

[41] L. A. Melnikov, V. L. Derbov, I. M. Umansky and S. I. Vinitsky, Hyperfine Interactions, **101/102** 471 (1996).

[42] I. V. Puzynin, T. P. Puzynina, S. I. Vinitsky and V. I. Puzynin, Hyperfine Interactions, **101/102** 493 (1996).

[43] G. Ya. Korenman, Hyperfine Interactions, **103**, 341 (1996).

[44] V. I. Korobov, Phys. Rev. A **54**, R1749 (1996).

[45] V. I. Korobov, Phys. Rev. Lett., *in print.*

[46] D. Bakalov and V. I. Korobov, Phys. Rev. A, *in print.*

[47] J. Révai and A. T. Kruppa, Phys. Rev. A, accepted.

[48] E. Yarevsky and N. Elander, Europhys. Letters **37** 453 (1997).

[49] N. Elander and E. Yarevsky, Phys. Rev. A, **55**, (Sept. 1997).

[50] S. Andersson, N. Elander and E. Yarevsky, Phys. Rev. A, submitted.

[51] Y. Kino, M. Kamimura and H. Kudo, Proc. XV. Int. Conf. *Few-Body Problems in Physics*, Groningen, 1997.

[52] H. J. Reyher et al., Phys. Lett. A, **115**, 238 (1986)

[53] S. I. Kanorsky et al., Phys. Rev. B, **50**, 6296 (1994).

[54] R. E. Collin, *Foundations for Microwave Engineering*, Ch. 7, McGraw-Hill, Intern. Ed., Singapore, 1992.

[55] see e.g., H. Knudsen and J. F. Reading, Phys. Rept. **212**, 107 (1992)

[56] L. H. Andersen et al., Phys.Rev. **A41,** 6536 (1990)

[57] P. Hvelplund et al., J.Phys. B **27**, 925 (1994) – and references therein.

[58] L. Ford and J. F. Reading, J. Phys. B **27**, 4215; and J. F. Reading et al., Phys. Rev. Lett. (1997)

[59] S. P. Moeller, E. Uggerhoej, H. Bluhme, H. Knudsen, U. Mikkelsen, K. Paludan, and E. Morenzoni, Accepted for publication, Phys. Rev. A (1997)

[60] see e.g., R. Bacher et al., in *Fundamental Symmetries*, ed., P. Bloch et al. (Plenum Press, New York, 1987).

[61] A. Kreissl et al., Z. Phys. **C37** (1988) 557.

[62] A. H. Soerensen, Nucl Instr. Meth., **B48**, 10 (1990)

[63] A. Adamo et al., Phys. Rev. A **47**, 4517 (1993) and M. Agnello et al., Phys. Rev. Letters **74**, 371 (1995).

[64] E. A. Mason and E. W. Mcdaniel, *Transport properties of ions in gases*, John Wiley & Sons (1988), and E. W. McDaniel et al., *Ion Molecule Reactions*, John Wiley & Sons (1970).

[65] G. Both et al., Rev. Sci. Instrum. **58** 424 (1987).

[66] H. Knudsen et al., Phys. Rev. Letters **74**, 4627 (1995).

[67] E. Fermi and E. Teller, Phys. Rev. **72**, 399 (1947).

[68] D. R. Schultz, P.S. Krstic, C. O. Reinhold and J. C. Wells, Phys. Rev. Letters **76**, 2882 (1996).

[69] J. C. Wells, D. R. Schultz, P. Gavras and M. S. Pindzola, Phys Rev A **54**, 593 (1996).

[70] G. Schiwietz, private communication and J. Phys B **29**, 307 (1996).

[71] J. F. Reading, T. Bronk, A. L. Ford, L. A. Wehrman and K. A. Hall, J. Phys. B **30**, L189 (1997).

[72] P. S. Krstic and D. R. Schultz: Submitted to Phys. Rev. A (1997).

[73] J. Ullrich et al., J. Phys. B **30** 2917 (1997).

[74] C. L. Cocke, Phys. Rep. **205** 153 (1991).

[75] J. S. Cohen, Phys. Rev.A (to be published, Nov. 1997).

[76] D. R. Schultz, P. S. Krstic, C. O. Reinhold, and J. C. Wells, Phys. Rev. A (to be published).

[77] D. R. Miller, *Free Jet Sources*, Atomic and Molecular Beam Methods, Vol. 1 (Oxford University Press, 1988)

[78] R. J. Hughes and B.I. Deutch, Phys. Rev. Lett. **69** (1992) 578.

[79] G. Gabrielse et al., Phys. Rev. Lett. **74** (1995) 3544.

[80] P. Roberson et al., Phys. Rev. **C16** (1977) 1945; E. Hu et al., Nucl. Phys. **A254**, 403 (1975), and B. L. Roberts et al., Phys. Rev. **D12**, 1232 (1975).

[81] G. Reifenröther and E. Klempt, Nucl.Phys. **A503**, 885 (1989).

[82] T. P. Terada and R. S. Hayano, Phys. Rev. **C55**, 73 (1997).

[83] H. A. Bethe and E. E. Salpeter, *Quantum Mechanics of One and Two ELectron Atoms*, Plenum Press, New York 1977.

[84] J. S. Cohen and N. T. Padial, Phys. Rev. **A41** (1990) 3460.

[85] see e.g., Demtröder, *Laser Spectroscopy (2nd ed.)*, Sect. 7.5, 466–479, Springer-Verlag, Berlin, 1996.

[86] M. H. Holzscheiter, Physica Scripta **T59** (1995) 326.

[87] M. Kimura and M. Inokuti, Phys.Rev. **A38** (1988) 3801.

[88] D. R. Schultz, P. S. Kristic, and C. O. Reinhold, J. C. Well, Phys. Rev. Lett. **76**, 2882 (1996).

[89] E. A. Solov'ev, Sov. Phys. JETP **54**, 893 (1981); T. P. Grozdanov and E. A. Solov'ev, Phys. Rev. A 42, 2703 (1990).

[90] C. J. Wood and R. E. Olson, J. Phys. B **29**, L257 (1996).

[91] R. Dörner, H. Kehmliche, M. H. Prior, C. L. Cocke, J. A. Gary, R. E. Olson, V. Mergel, J. Ullrich, and H. Schmidt-Böcking, Phys. Rev. Lett. **77**, 4520 (1996).

[92] R. Moshammer, J. Ullrich, M. Unverzagt, W. Schmidt, P. Jardin, R.E. Olson, R. Mann, R. Dörner, V. Mergel, U. Buck, H. Schmidt-Böcking, Phys. Rev. Lett. **73**, 3371 (1994).

[93] R. Moshammer, J. Ullrich, H. Kollmus, W. Schmitt, M. Unverzagt, H. Schmidt-Böcking, CJ. Wood, R.E. Olson, Phys. Rev. A **56**, 1351 (1997).

[94] R. Moshammer, W. Schmitt, J. Ullrich, H. Kollmus, A. Cassimi, R. Dörner, O. Jagutzki, R. Mann, R. E. Olson, H. T. Prinz, H. Schmidt-Böcking, L. Spielberger, Phys. Rev. Lett. (accepted).

[95] R. Moshammer, J. Ullrich, H. Kollmus, W. Schmitt, M. Unverzagt, O. Jagutzki, V. Mergel, H. Schmidt-Böcking, R. Mann, C. Wood, and R. E. Olson, Phys. Rev. Lett. **77**, 1242 (1996).

[96] R. Moshammer, M. Unverzagt, W. Schmitt, J. Ullrich and H. Schmidt-Böcking, Nucl. Instr. Meth. **B108**, 425 (1996).

[97] J. Ullrich, R. Moshammer, R. Dörner, O. Jagutzki, V. Mergel, H. Schmidt-Böcking, L. Spielberger, Topical Review, J. Phys. B **30**, 2917 (1997).